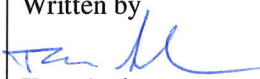# Analysis of discontinuities in metallic materials with the extended finite element method (Master's Thesis)

Authors: Tom Andersson

Confidentiality: Public

Report's title	
Analysis of discontinuities in metallic materials with the extended finite element method (Master's Thesis)	
Customer, contact person, address	Order reference
VYR, VTT	
Project name	Project number/Short name
Reaktoripiirin murtumisriskin arviointi v. 2010	41782-1.2.3 / FRAS 10
Author(s)	Pages
Tom Andersson	80 p.
Keywords	Report identification code
FEM, XFEM, fracture mechanics, crack propagation	VTT-R-02635-10

Summary

The goal of this work was to develop a finite element method code able to handle strong and weak discontinuities in two dimensional cases. The code is able to model crack (strong discontinuity) propagation and take into account the presence of precipitates. Precipitates (weak discontinuity) are modeled as small material domains with Young's modulus differing from the rest of the specimen.

The code is written in Matlab utilizing the Getfem general purpose finite element (FE) library. Getfem-library is an open source library developed with C++. As case studies three edge crack configurations in a two dimensional tensile type fracture mechanics square specimen are considered. In these cases the specimen is loaded from its upper boundary and the lower boundary is fixed. In first case a stationary crack, with length of 3/10 of the whole specimen, is analyzed with the aim of verifying the code. In the cases to follow the crack propagation capabilities of the implementation are investigated. The initial crack length in these cases is 1/10 of the whole specimen. The maximum circumferential tensile stress criterion is used to calculate the crack propagation angle. In second case three different crack propagation variants are considered: one with loading perpendicular to the crack, one with loading parallel to the crack, and one with a 45° angle. The third case is similar to the first variant of case two only difference is that precipitates are included into the material. Constitutive properties of the precipitates differ in these analyses.

The code was verified by crosschecking computed stress intensity factor values with analytical ones. The computed result were in good agreement with theory. The crack propagation was analyzed by comparing the computed crack growth angles and the ones given by the used crack growth criterion. The crack propagation and its behavior near regions with discontinuously varying material properties were in good accordance with theoretical crack propagation. The Getfem-library is found to be effective and user friendly, regardless of the lack of documentation, in building XFEM codes. The code developed during this work will be used as a base for more sophisticated and effective XFEM codes.

Confidentiality	Public

Espoo, 29 March 2010		
Written by	Reviewed by	Approved by
Tom Andersson Research Scientist	Pekka Nevasmaa Senior Research Scientist	Pentti Kauppinen Technology Manager

VTT's contact address

VTT Technical Research Centre of Finland, P.O. Box 1000, FI-02044 VTT, Finland
Tel. +358 20 722 4725, Fax +358 20 722 7002, e-mail: tom.andersson@vtt.fi

Distribution (customer and VTT)
SAFIR/FRAS-project
VTT Arcives

Preface

This work was performed at VTT under the project SAFIR2010. SAFIR2010 is a research programme on nuclear power plant safety. The programme is the latest link in the chain of public research programmes on nuclear safety that maintain and develop know-how in Finland.

I wish to thank M.Sc. Anssi Laukkanen for providing me an interesting topic for my master's thesis work and for the advice and support given in the course of this work. I also wish to thank M.Sc. Lauri Elers and M.Sc. Matias Ahonen for their help during this work.

The advices of Professor Jukka Tuhkuri are acknowledged.

In Espoo February 3, 2010

Tom Andersson

Contents

List of symbols

A	stiffness matrix
A^+, a^-	influence domains of a node on opposite sides of a crack
a	crack length
a_{eff}	effective plastic zone corrected crack length
b	load vector
C	A positive constant
E	Young's modulus
$F, F(x)$	function or functional
$\hat{F}$	isoparametric mapping function
f	body force vector
$f_{ij}^i(x)$	function of x in ij- direction for crack opening mode i (i= I, II or III)
g	a force or a flow on Γ
h	a mesh parameter (e.g. in triangular mesh: the longest side of the K)
$H, H(\xi)$	The Heaviside function
J	J integral; EPFM crack growth parameter
K_k	stress in tensity factor for crack opening mode i (k= I, II or III)
K_c	critical stress intensity factor; a material parameter
K_j	(mesh) element number
$L(\mathbf{x})$	level set function
N_i	node number
P_K	Finite element space
p	basis function which includes shape functions ϕ
p^{bas}	traditional basis function
p^{enr}	enrichment part of the basis function
$\mathbb{R}^n$	n dimensional real space
r_y, r_p	plastic zone size
T_h	set of elements (mesh)
T_h	traction vector
$u, u(x)$	displacement vector
$u^h, u^h(x)$	FEM approximation of displacement vector
V, V_h	finite dimensional space, ϕ_i form basis
v	function
W	Specimen width
w	strain energy density
$\mathbf{x}$	position vector

Greek symbols

δ_{ij}	Kronecker's delta, 1 if i = j otherwise 0
Γ, Γ^e, Γ^c	boundary of Ω
ε_{ij}	strain components in direction $_{ij}$
η_j, η_j^e	unknowns or degrees of freedom associated to FEM solution
θ	angular polar coordinate
κ	bulk modulus
λ	Lamé coefficient
μ	shear modulus
ν	Poisson 's ratio
$\Xi(\mathbf{N})$	enrichment function of nodes $\mathbf{N}$ for weak discontinuities
ξ	signed distance function
ρ	strip yield model plastic zone size
σ_0	tensile loading
σ_{ys}	yield strength
σ_{ij}	stress components in the direction ij (i,j= x, y and z)
Φ	Airy's stress function
ϕ	shape function
ϕ^e	extrinsic base shape function
$\Psi(\mathbf{N})$	enrichment function of nodes $\mathbf{N}$
Ω	bounded open domain

1

Introduction

Traditional finite element methods have limitations in treating weak and strong discontinuities due to the selections made in defining test and shape function bases. As a result mesh design needs to be modified to accommodate the existence of such discontinuities (material interfaces, cracks etc.) which poses severe restrictions to the modeling and evolution of discontinuities within an analysis.

A classic example is crack propagation, where standard displacement formulated Galerkin finite element method (FEM) requires significant reworking and typically introduction of adaptivity to be able to tackle the problem efficiently. Even with such modifications, the resulting methodologies lack in accuracy and do not yield a methodology suitable for complex constitutive models nor behavior in general three-dimensions. Various solutions have been proposed: i) Variating mesh densities (h-adaptivity) or shape function degree (p-adaptivity) (i.e. [1]), ii) augmented Lagrangian-Eulerian meshes (i.e. [2]), iii) boundary element methods (i.e. [3]), iv) element-free methods (i.e. [4]) to name a few. Out of these examples, only the element-free Galerkin (EFG) method is enough efficient to truly provide a generic partial-differential equation (PDE) solving methodology which can successfully tackle with discontinuities. EFG however, has a number of problems of its own, and as such, its wide-scale application has so far been fairly limited.

To combat its deficiencies, a simpler methodology having a partition of unity like background has been presented, the extended finite element method (XFEM). XFEM utilizes a typical FEM scheme for computing the conservation integrals, thus avoiding much of the problems of EFG, but rather that trying to get away from the crude discretization process itself, it enhances (extends) the test and shape function space to better suit modeling of weak and strong discontinuities.

The purpose of this work is to develop a XFEM code that is capable of handling strong and weak discontinuities. The code produced during this work will work as a foundation for more sophisticated and versatile code. The code is developed in a Matlab environment using Getfem-library. The Getfem-library is under constant development and new features are introduced in it from time to time. The library a generic open source finite element library. It actually is a C++-language library, but Matlab and Python interfaces are included in order to make it more easy to use. One purpose of this work is also test the quality and usability of the Getfem-library.

The XFEM code is validated by calculating a simple edge crack test case. The

geometry and boundary conditions of the specimen are intentionally kept simple to hinder the error produced by them. A linear-elastic material model is used in all cases. Although the code is tested only in two dimensional cases, in principle application for three dimensional problems is not limited.

In case one two different mesh discretizations are tested to study the mesh dependency of the methodology. Also the accuracy of the stress calculations are verified.

Codes capability for simulating crack propagation is tested with two different test cases: the first one with three different set ups and the latter with two different set ups. Specimen in these cases is similar as used in case one. In case two the variants are: A force perpendicular to the upper boundary, a force parallel to the upper boundary and a force tilted to 45° angle relative to upper boundary. The second and third variants are mixed mode cases while the first variant is almost pure crack opening mode I.

The case three is similar to the first variant of the case two. Only difference is that two precipitates are placed along the predicted crack propagation path. Material model used in the precipitates is the same used in the rest of the material only the Young's modulus is greater. Two different sub-cases are modeled in this case: one with precipitates three times stiffer and second with precipitates seven times stiffer than the main material.

The main focus of this work is to develop a working code, which could be used to analyze crack propagation. The actual analysis cases are simply model problems and hence, the mesh is left fairly coarse in order to limit computer time and memory capacity needed in this work. Though it is demonstrated to be dense enough for convergent results.

The code is capable of producing valid results in analyzing the crack problems. The error between computed stress intensity factor and the one calculated with Irwin's classical solutions is only about 12 % and it diminishes to - 4 % when the element density is increased. Also in propagating crack analysis the code produces valid crack paths (when comparing to ones found in literature). Altogether the code is working and it can be used as a base for a more advanced analysis tool.

Theory of the fracture mechanics is treated in the next chapter to give background of the phenomena. Chapter three and four treat the theory of FEM and the modifications made to it in XFEM. XFEM is treated in the extent to give tools to simple crack propagation analysis. For a more extensive review reader could for example turn to RWTH Aachen university's Internet site [5]. After the theoretical aspects needed to understand this work are dealt with, a short review of Getfem is followed by a chapter about the code developed in this work. The following three chapters consist of the results, discussion, and description of planned future work related to this master's thesis.

2

Fracture Mechanics

The fundamental difference in fracture mechanics compared to conventional theory of strength of materials can be explained with a simple example: An infinite plate under tensile loading with and without a tiny flaw (a circular hole) (figure 2.1). In the flawless plate the stress field is uniform and remains equal to the applied tensile stress, σ_0, while the elastic solution for an infinite plate with circular hole predicts a biaxial stress field with an stress concentration of 3 ($\sigma_y = 3 \ \sigma_0$ at $\theta = 0, \pi$ and $\sigma_x =$ -σ_0 at $\theta = \pi/2, 3\pi/2$ in figure 2.2) at the boundary of the hole.
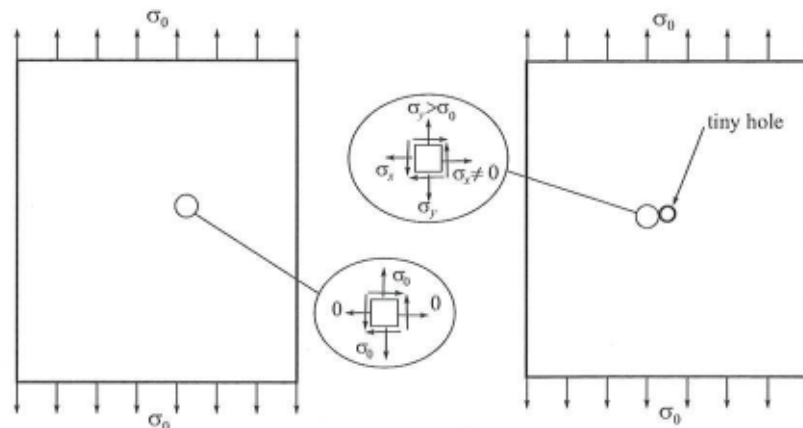
Figure 2.1: An infinite plate with and without a flaw. [6]

Fracture mechanics was developed in order to prevent accidents. The usage of metals, mainly steel and iron, for structural purposes increased enormously during the 19th century industrial revolution. The revolution in structural materials also, unfortunately, caused many accidents, some with loss of life. Large number of those accidents involved steam boiler explosions and railway equipment. Gradually it was found out the many of those accidents were due the material deficiencies in the form of pre-existing flaws. Although better production methods were developed to reduce the number of these type of failures, accidents still occurred. Even to structures in nominally very low stress conditions. It was soon found out that these newly developed steel types were brittle at low temperatures (figure 2.3). These accidents with the need

a) circular hole in an infinite plate   b) stress distribution around the hole
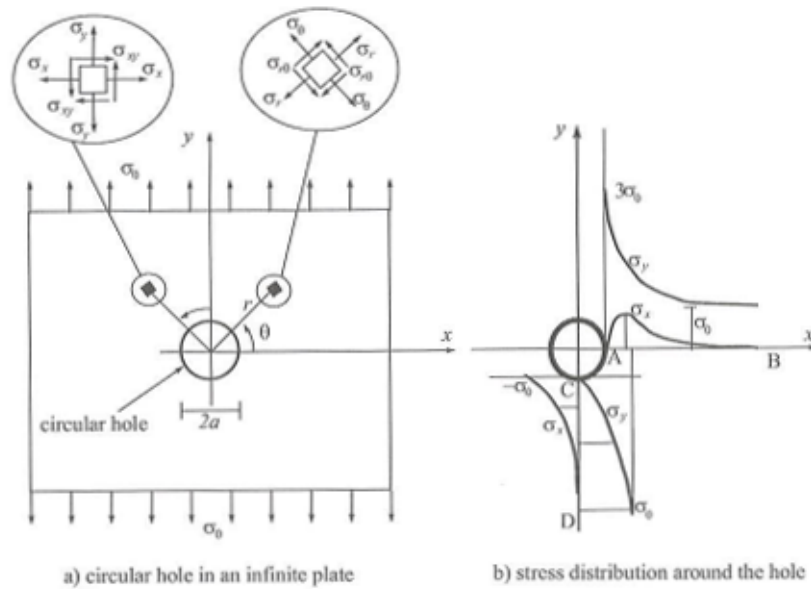
Figure 2.2: Detailed figure of the infinite plate with hole. Geometry on the left and stress distribution on the right. [6]

for lighter, high strength materials led to development of modern fracture mechanics.
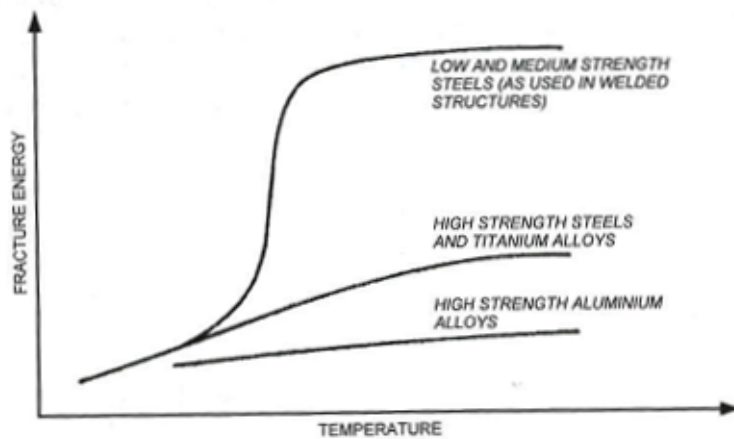
Figure 2.3: Schematic of general effect of temperature on the fracture energy of structural metals. [7]

Cracks propagation often has an element of time. There are several mechanisms for this subcritical crack propagation: Fatigue and creep to name a few.

Fatigue is caused by a repeated cyclic or otherwise varying loading and the amplitude of the loading is always below the level that is sufficient to cause failure in a single application of load. Creep is the tendency of a solid material to slowly move or deform permanently under long exposure to stress levels below the yield strength of the material. Although, neither of the fracture mechanisms are yet fully understood.

4

Environmental conditions (temperature, atmosphere, etc.) and material composition and behavior affects crack propagation.

On a microscopic level ductile structural materials often fail by microvoid coalescence. Microvoid formation and crack initiation is presented figure 2.4. Microvoids (white area) form if the local stress field causes an intermetallic particle or a precipitate (black spots) to split. Alternatively, metallic matrix can break the particle or grain boundaries can be separated, these lead to the same result: formation of a microvoid.

Figure 2.4: Crack propagation by transgranular microvoid coalescence. [7]

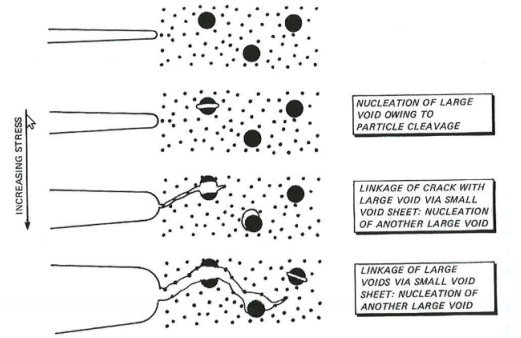Microvoids grow and coalescence during progressive loading, hence the name of the phenomena, and eventually forms a continuous cracked surface, as the local stress field increases.

Material orientation in different grains and phases affects the crack's path (figure 2.5). Material orientation inside a grain affects the crack growth direction as described next.

a) Cyclic slip begins in a surface grain and occurs mainly on one or few sets of crystal planes.

b) This usually leads to slip plane cracking (mode II, fracture modes are explained in the next section), which results in a faceted fracture surface, and spreading of cyclic slip to an adjacent grain. Again the slip is mainly on one or a few sets of crystal planes.

c) The second grain also cracks along the slip plane. Cyclic slip in the interior is now activated on several sets of crystal planes. This enables mode I crack extension.

d) Cyclic slip on several sets of crystal planes results in a continuum mechanism of crack propagation, often characterized by fatigue striations.

The object in fracture mechanics is to quatify the conditions of crack propagation, the residual strength of the structure as a function of crack size and the maximum allowable crack size. The rate of crack propagation in several failure mechanisms, is a function of several variables, and it will usually increase progressively as the crack grows (figure 2.6 a). As the crack propagates the residual strength, which is the failure

5
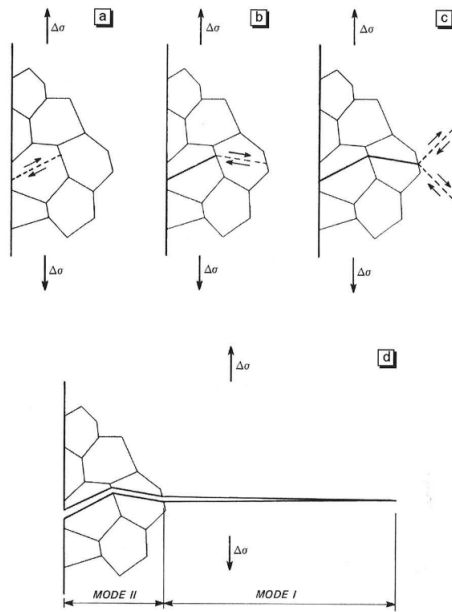
Figure 2.5: Fatigue crack initiation and growth corresponding to a transition from mode II to mode I. [7]

strength as a function of crack size, of the structure decreases (figure 2.6 b). After enough time the residual stress reaches the limit where the structure fails.
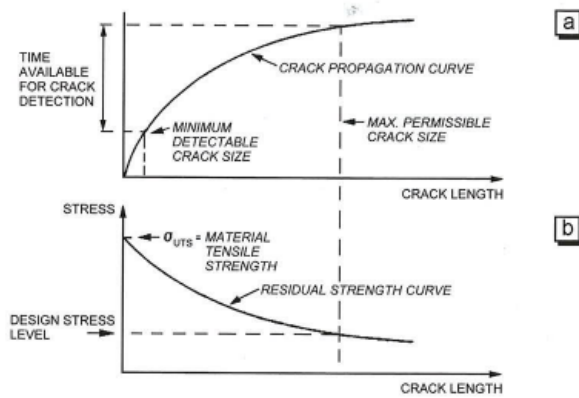

Figure 2.6: The engineering problem of a crack in a structure. [7]

Theoretical concepts presented in this chapter are an adaptation of the one presented in [7] and [8].

6

2.1 LEFM

Linear-elastic fracture mechanics (LEFM) describes the fracturing behavior of a material that obey Hooke's law (i.e. linear material behavior).

Characteristics of stress, strain, and displacement near the crack tip may be divided into three basic types, figure 2.7. Three independent types of loading enable
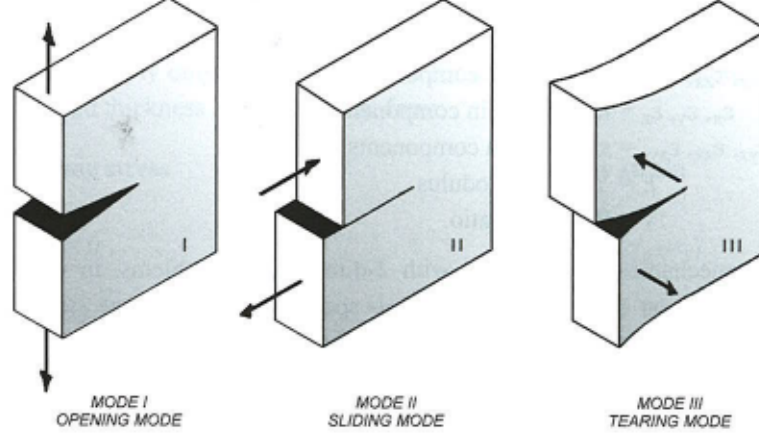
Figure 2.7: The crack loading modes. [7]

crack initiation and propagations in: Mode I Opening mode (a tensile stress normal to the plane of the crack), Mode II Sliding mode (a shear stress acting parallel to the plane of the crack and perpendicular to the crack front), and Mode III Tearing mode (a shear stress acting parallel to the plane of the crack and parallel to the crack front).

The loading modes in LEFM are a decomposition of the stress tensor, hence,

$$\sigma_{ij} = \sigma_{ij}^{I} + \sigma_{ij}^{II} + \sigma_{ij}^{III}. \tag{2.1}$$

Elastic Stress Field Equations

Stress field in a biaxially loaded infinite cracked plate can be obtained from Williams ([9]) and Westergaard ([10]) crack analysis (figure 2.8) This is done by substituting the solution, a complex stress function $\phi(z)$, that Westergaard proposed the biharmonic stress function 2.2 as a solution to Airy's stress function 2.3

$$\Phi = \mathrm{Re}\bar{\bar{\phi}}(z) + \mathrm{Im}\bar{\phi}(z), \tag{2.2}$$

where $\bar{\phi}(z)$ and $\bar{\bar{\phi}}(z)$ are first and second order integrals of $\phi(z)$, respectively and $z = x + i \cdot y$. The stress components then become:

$$\sigma_{xx} = \frac{\partial \Phi}{\partial y}, \sigma_{yy} = \frac{\partial \Phi}{\partial x}, \sigma_{xy} = \frac{\partial \Phi}{\partial x \partial y}. \tag{2.3}$$
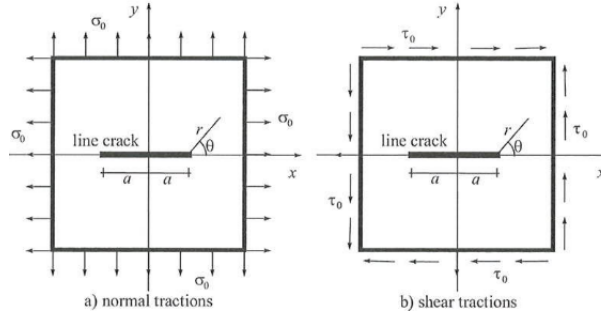
Figure 2.8: An infinite plate subjected to uniform normal (a) and shear (b) traction. [6]

This stress field always fulfills the equilibrium equations of stress 2.5. These equilibrium equations are obtained from figure 2.9. Material element is in equilibrium of forces in x-direction when

$$
\begin{aligned}
(\sigma_{xx} + \frac{\partial \sigma_{xx}}{\partial x} dx)dydz - \sigma_{xx}dydz \quad &+ \\
(\sigma_{xy} + \frac{\partial \sigma_{xy}}{\partial y} dy)dzdx - \sigma_{xy}dzdx \quad &+ \\
(\sigma_{xz} + \frac{\partial \sigma_{xz}}{\partial z} dz)dxdy - \sigma_{xz}dxdy \quad &= \quad 0.
\end{aligned}
\tag{2.4}
$$

Equilibrium of forces in y- and z-directions is obtained in similar manner. This leads

Figure 2.9: The stress components acting in the x direction on an infinitesimal material element [7]

to an equilibrium of stress

$$
\frac{\partial \sigma_{xx}}{\partial x} + \frac{\partial \sigma_{xy}}{\partial y} + \frac{\partial \sigma_{xz}}{\partial z} = 0
\tag{2.5a}
$$

$$
\frac{\partial \sigma_{yy}}{\partial y} + \frac{\partial \sigma_{yz}}{\partial z} + \frac{\partial \sigma_{yx}}{\partial x} = 0
\tag{2.5b}
$$

8

$$\frac{\partial \sigma_{zz}}{\partial z} + \frac{\partial \sigma_{zx}}{\partial x} + \frac{\partial \sigma_{zy}}{\partial y} = 0. \tag{2.5c}$$

In two dimensional case figure 2.8, where $\sigma_{zy} = \sigma_{zx} = 0$ and $\frac{\partial}{\partial z} = 0$ equilibrium equations 2.5 reduced to

$$\frac{\partial \sigma_{xx}}{\partial x} + \frac{\partial \sigma_{xy}}{\partial y} = 0 \tag{2.6a}$$

$$\frac{\partial \sigma_{yy}}{\partial y} + \frac{\partial \sigma_{yx}}{\partial x} = 0. \tag{2.6b}$$

Stress components can be found by substituting 2.2 into 2.3:
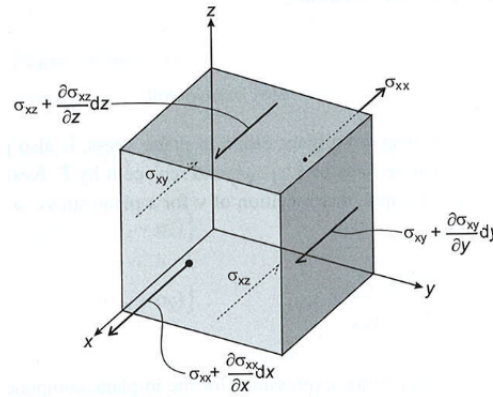
$$\sigma_{xx} = \text{Re}\phi(z) - y \cdot \text{Im}\phi'(z) \tag{2.7a}$$

$$\sigma_{yy} = \text{Re}\phi(z) + y \cdot \text{Im}\phi'(z) \tag{2.7b}$$

$$\sigma_{xy} = -y \cdot \text{Im}\phi'(z). \tag{2.7c}$$

The complex function $\phi(z)$ that satisfies the boundary conditions along the crack and in infinity (figure 2.8a) is

$$\phi(z) = \frac{\sigma_0}{\sqrt{1 - \frac{a^2}{z^2}}} \tag{2.8}$$

Finally, by substituting 2.8 into 2.7, the near crack tip solutions are obtained ($r << a$)

$$\sigma_{xx} = \frac{\sigma_0\sqrt{\pi a}}{\sqrt{2\pi r}}\cos\frac{\theta}{2}(1 - \sin\frac{\theta}{2}\sin\frac{3\theta}{2}) \tag{2.9a}$$

$$\sigma_{yy} = \frac{\sigma_0\sqrt{\pi a}}{\sqrt{2\pi r}}\cos\frac{\theta}{2}(1 + \sin\frac{\theta}{2}\sin\frac{3\theta}{2}) \tag{2.9b}$$

$$\sigma_{xy} = \frac{\sigma_0\sqrt{\pi a}}{\sqrt{2\pi r}}\sin\frac{\theta}{2}\cos\frac{\theta}{2}\cos\frac{3\theta}{2}. \tag{2.9c}$$

Irwin introduced (late 1950s) [11] the stress intensity factor (SIF), K. He illustrated that all elastic stress fields around the crack tip are distributed similarly, and $K_k = \sigma_{ij}\sqrt{\pi r}$ (k is the displacement mode I ,II or III) controls the local stress quantity. Irwin also argued that the stress field in uniaxially (y-direction) loaded plate is identical to biaxially loaded one with the exception of σ_{xx}, which is reduced by the remote stress field. Although, in near tip stress field the correction is usually omitted because near the crack tip σ_{xx} is much larger than σ_0. Equations above also shows that the stress field tends to infinity at the crack tip, $\frac{1}{\sqrt{r}}$ singularity. Substituting SIF into expressions 2.7 the elastic stress state around the crack can be presented by

$$\sigma_{ij} = r^{-\frac{1}{2}}\{K_I f_{ij}^I(\theta) + K_{II} f_{ij}^{II}(\theta) + K_{III} f_{ij}^{III}(\theta)\} + \text{higher order terms} \tag{2.10}$$

where σ_{ij} is the near crack tip stress, $f_{ij}^k(\theta)$ are functions of θ (equations 2.9), and K_I, K_{II} and K_{III} are the SIFs, the parameters that LEFM lies on, associated with crack opening modes

$$K_I = lim_{r\to 0, \theta=0}\sigma_{yy}\sqrt{2\pi r} \tag{2.11a}$$

$$K_{II} = lim_{r\to 0, \theta=0}\sigma_{xy}\sqrt{2\pi r} \tag{2.11b}$$

$$K_{III} = lim_{r \to 0, \theta = 0} \sigma_{yz} \sqrt{2\pi r}. \tag{2.11c}$$

K_k describes the magnitude of the elastic stress field. It can also be used to describe fracture behavior and the crack growth assuming that the stress field near the crack tip remains elastic.

The SIF in mode I 2.11a can be simplified by substituting equation 2.9b into equation 2.11a

$$K_I = \sigma_0 \sqrt{\pi a}. \tag{2.12}$$

The stress field similarly in the pure mode II loading

$$\sigma_{xx} = -\frac{K_{II}}{\sqrt{2\pi r}} \sin\frac{\theta}{2}(2 + \cos\frac{\theta}{2}\cos\frac{3\theta}{2}) \tag{2.13a}$$

$$\sigma_{yy} = \frac{K_{II}}{\sqrt{2\pi r}} \sin\frac{\theta}{2}\cos\frac{\theta}{2}\cos\frac{3\theta}{2} \tag{2.13b}$$

$$\sigma_{xy} = \frac{K_{II}}{\sqrt{2\pi r}} \cos\frac{\theta}{2}(1 - \sin\frac{\theta}{2}\sin\frac{3\theta}{2}), \tag{2.13c}$$

and in pure mode III loading

$$\sigma_{xz} = \frac{K_{III}}{\sqrt{2\pi r}} \sin\frac{\theta}{2} \tag{2.14a}$$

$$\sigma_{yz} = \frac{K_{III}}{\sqrt{2\pi r}} \cos\frac{\theta}{2}. \tag{2.14b}$$

The solutions for the SIF 2.11 are strictly valid only for an infinite plate. In real life engineering problems specimen geometry has to be taking into account. It is done by modifying (e.g. K_I in equation 2.12) the SIF by introducing a geometrical correction, $f(a/W)$, where a is the crack length and W is specimen width, the expression always containing the characteristic geometric parameters of the geometry.

Examples of Stress Intensity Factors

Analytical solutions of mode I stress intensity factors to four classical fracture mechanics problems are presented in this section [7]. The problems are presented in figure 2.10. In the first figure (2.10a) is a tensile plate problem with crack at the center:

$$K_I = [1 + 0.256(\frac{a}{W}) - 1.152(\frac{a}{W})^2 + 12.200(\frac{a}{W})^3]\sigma_0\sqrt{\pi a}. \tag{2.15}$$

Next in figure 2.10b is depicted a tensile plate with an edge crack:

$$K_I = [1.122 - 0.231(\frac{a}{W}) + 10.550(\frac{a}{W})^2 - 21.710(\frac{a}{W})^3 + 30.382(\frac{a}{W})^4]\sigma_0\sqrt{\pi a}. \tag{2.16}$$

Problem in figure 2.10c has an edge crack at both sides:

$$K_I = [\frac{1.122 - 1.22(\frac{a}{W}) - 0.820(\frac{a}{W})^2 + 3.768(\frac{a}{W})^3 - 3.040(\frac{a}{W})^4}{\sqrt{1 - \frac{2a}{W}}}]\sigma_0\sqrt{\pi a}. \tag{2.17}$$

The last problem 2.10d depicts a0 center crack grown into a small elliptical hole

$$K_I = [\frac{[sin^2(\theta) + \frac{b}{a}cos^2(\theta)]^{\frac{1}{4}}}{\frac{3\pi}{8}} + \frac{\pi}{8}\frac{b^2}{a^2}]\sigma_0\sqrt{\pi a}, \tag{2.18}$$

where θ is defined in figure 2.11.
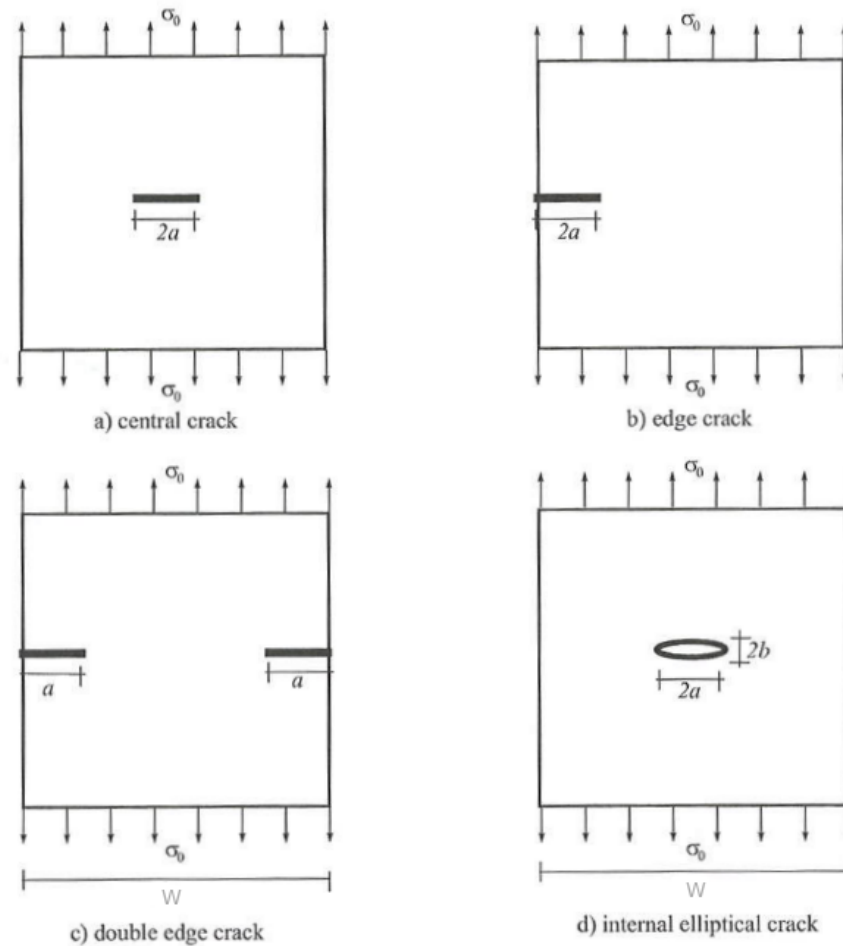
Figure 2.10: Typical plate problems of fracture mechanics. [6]
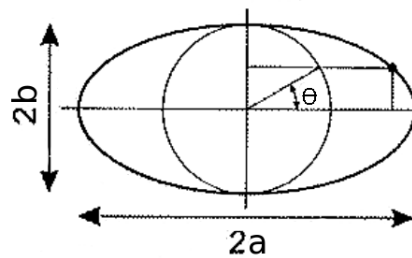
Figure 2.11: Definition of theta for internal elliptical crack. [7]

Crack Tip Plasticity

Previous K_K solutions, with infinite stress at the crack tip (owning to the infinitely sharp crack tip), are not exactly physical viable for real materials. Real material, with atomic structures, can only have the crack tip radius about the interatomic distance. This sets some limits to the stress field. More importantly, inelastic material

deformation (e.g. plasticity in metals and crazing in polymers) further relaxes the stress field at the crack-tip. This inelastic material deformation at stress levels above the yield stress leads to a plastic zone surrounding the crack tip. The accuracy of the elastic stress analysis diminishes as the plastic zone grows. For moderate crack tip yielding, two simple corrections to LEFM have been developed: The Irwin approach and the strip yield model ([12] and [13]). Both of these models predicts that the shape of the plastic zone to be circular, which is not exact. However, the shape of the predictions is not that important since they both are valid only on the x-axis ($\theta = 0$).

The Irwin model states that on the crack plane ($\theta = 0$) near the crack tip plastic zone size is

$$r_y = \frac{1}{2\pi}(\frac{K_I}{\sigma_{ys}})^2, \tag{2.19}$$

the equation for first order estimate for plastic zone size above is derived from the equation for horizontal stress 2.9 by substituting yield strength, σ_{ys}, for σ_{xx}. Shape of the plastic zone is considered to be circular, although this is only an approximation, and strain hardening is neglected. as figure 2.12 illustrates, the stress singularity is truncated by yielding at the crack tip.

The analysis in equation 2.19 is based on an elastic crack tip solution, and thus, is not strictly correct. Stresses are redistributed when yielding occurs in order to satisfy equilibrium. The cross-hatched region in figure 2.12 represents forces that are present in an elastic material but cannot be carried in the elastic-plastic material because the stress cannot exceed the yield strength. Thus, the plastic zone must increase in size in order to accommodate these forces. A simple force balance leads to a second order estimate of the plastic zone size r_p:

$$\sigma_{ys}r_p = \int_0^{r_p} \sigma_{xx}dr \Rightarrow r_p = \frac{1}{\pi}(\frac{K_I}{\sigma_{ys}})^2, \tag{2.20}$$

which is twice as large as first order estimate. Furthermore, the result means that the notational crack length is slightly longer than the actual crack size when considering the effective crack driving force. The effective crack length is defined as the sum of the actual crack size and a plastic zone correction

$$a_{eff} = a + r_y, \tag{2.21}$$

where r_y is for plane stress. In plane strain, yielding is suppressed by the triaxial stress state, and the Irwin plastic zone correction is smaller by a factor of 3

$$r_y = \frac{1}{6\pi}(\frac{K_I}{\sigma_{ys}})^2. \tag{2.22}$$

The effective stress intensity is obtained by inserting a_{eff} into the K expression for the geometry of interest

$$K_{eff} = \sigma\sqrt{\pi a_{eff}}f(\frac{a_{eff}}{W}). \tag{2.23}$$

Since the effective crack size is taken into account in the geometry correction factor $f(\frac{a_{eff}}{W})$, an iterative solution is usually required to solve for K_{eff}.
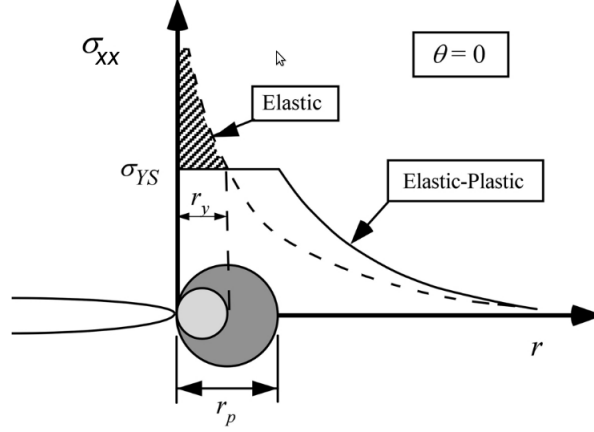
Figure 2.12: First-order and second-order estimates of plastic zone size. [8]
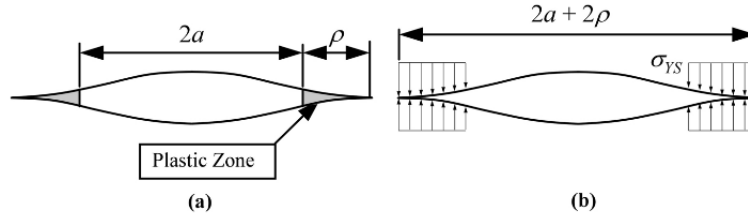
Figure 2.13: The strip-yield model. The plastic zone is modeled by yield magnitude compressive stresses at each crack tip (b). [8]

The strip yield model (figure 2.13) assumes that all the plastic yielding concentrates in a strip in front of the crack. This type of behavior does occur in some materials. In this model the effective crack length is also longer than the physical length(firgure 2.13).

In this model the material is assumed to be elastic-perfectly plastic as well and the material to be plane stress state. Since the stresses are finite in the strip-yield zone, there cannot be a stress singularity at the crack tip. The strip-yield plastic zone is modeled by adding to the crack length $2a$ a plastic zone length 2ρ, with a closure stress equal to σ_{ys} applied at each crack tip (figure 2.13 (b)). The plastic zone length ρ must be chosen such that the stress intensity factors from the remote tension and closure stress cancel one another. The closing stress intensity at each crack tip may be written as follows

$$K_{closure} = -2\sigma_{ys}\sqrt{\frac{a+\rho}{\pi}}\cos^{-1}(\frac{a}{a+\rho}). \tag{2.24}$$

The effective length of the crack can be evaluated by specifying the stress intensity from the remote tensile stress, $K_\sigma = \sigma\pi(a+\rho)$ and $K_{closure}$ equal. Therefore,

$$\frac{a}{a+\rho} = \cos(\frac{\pi\sigma}{2\sigma_{ys}}) \text{ or } 1 + \frac{\rho}{a} = \sec\frac{\pi\sigma}{2\sigma_{ys}}, \tag{2.25}$$

13

the ρ approaches infinity as $\sigma \to \sigma_{ys}$. ρ can be evaluated by using the Taylor series expansion on equation 2.25

$$\frac{a}{a + \rho} = 1 - \frac{1}{2!}(\frac{\pi\sigma}{2\sigma_{ys}})^2 + \frac{1}{4!}(\frac{\pi\sigma}{2\sigma_{ys}})^4 - \frac{1}{6!}(\frac{\pi\sigma}{2\sigma_{ys}})^6 + \dots \tag{2.26}$$

Neglecting all but the first two terms and solving for the plastic zone size gives for $\sigma \ll \sigma_{ys}$

$$\rho = \frac{\pi^2\sigma^2 a}{8\sigma_{ys}^2} = \frac{\pi}{8}(\frac{K_I}{\sigma_{ys}})^2. \tag{2.27}$$

the Irwin 2.27 and strip yield 2.20 approaches predict similar plastic zone sizes; since $1/\pi = 0.318$ and $\pi/8 = 0.392$. One way to estimate the effective stress intensity with the strip yield model is to set a_{eff} equal to $a + \rho$

$$K_{eff} = \sigma\sqrt{\pi a \sec{(\frac{\pi\sigma}{2\sigma_{ys}})}}. \tag{2.28}$$

Equation 2.28 tends to overestimate K_{eff} since the actual a_{eff} is somewhat less than $a + \rho$. This is due that the strip yield zone is loaded to σ_{ys}, which is not exactly true since the elastic stress distribution above σ_{ys} is actually redistributed and retransmitted. A more realistic estimate of K_{eff} for the strip-yield model is proposed by Burdekin and Stone

$$K_{eff} = \sigma_{ys}\sqrt{\pi a}[\frac{8}{\pi}\ln\sec(\frac{\pi\sigma}{2\sigma_{ys}})]. \tag{2.29}$$

The shape of the plastic zone can be predicted by applying a proper yield criterion (e.g. Von Mises or Tresca). A prediction for the plastic zone shape can be derived, for example for a 2 dimensional mode I crack, by first defining principal stresses

$$\sigma_1,\ \sigma_2 = \frac{\sigma_{xx} + \sigma_{yy}}{2} \pm [(\frac{\sigma_{xx} + \sigma_{yy}}{2})^2 + \sigma_{xy}^2]^{\frac{1}{2}} \tag{2.30a}$$

$$\sigma_3 = \begin{cases} 0 & \text{for plain stress} \\ \nu(\sigma_1 + \sigma_2) & \text{for plain strain} \end{cases} \tag{2.30b}$$

from the appropriate equation for stresses (2.9). Substituting the derived principal stresses into the Von Mises yield criterion

$$(\sigma_1 - \sigma_2)^2 + (\sigma_2 - \sigma_3)^2 + (\sigma_3 - \sigma_1)^2 = 2\sigma_{ys} \tag{2.31}$$

yields for the plastic zone radius as afunction of θ

$$r_y(\theta) = \frac{1}{4\pi}(\frac{K_I}{\sigma_{ys}})^2[1 + \cos\theta + \frac{3}{2}\sin^2\theta] \tag{2.32}$$

for plane stress, and

$$r_y(\theta) = \frac{1}{4\pi}(\frac{K_I}{\sigma_{ys}})^2[(1 - 2\nu)^2(1 + \cos\theta) + \frac{3}{2}\sin^2\theta] \tag{2.33}$$

for plane strain. Plastic zones for all three modes are plotted in figure 2.14 The

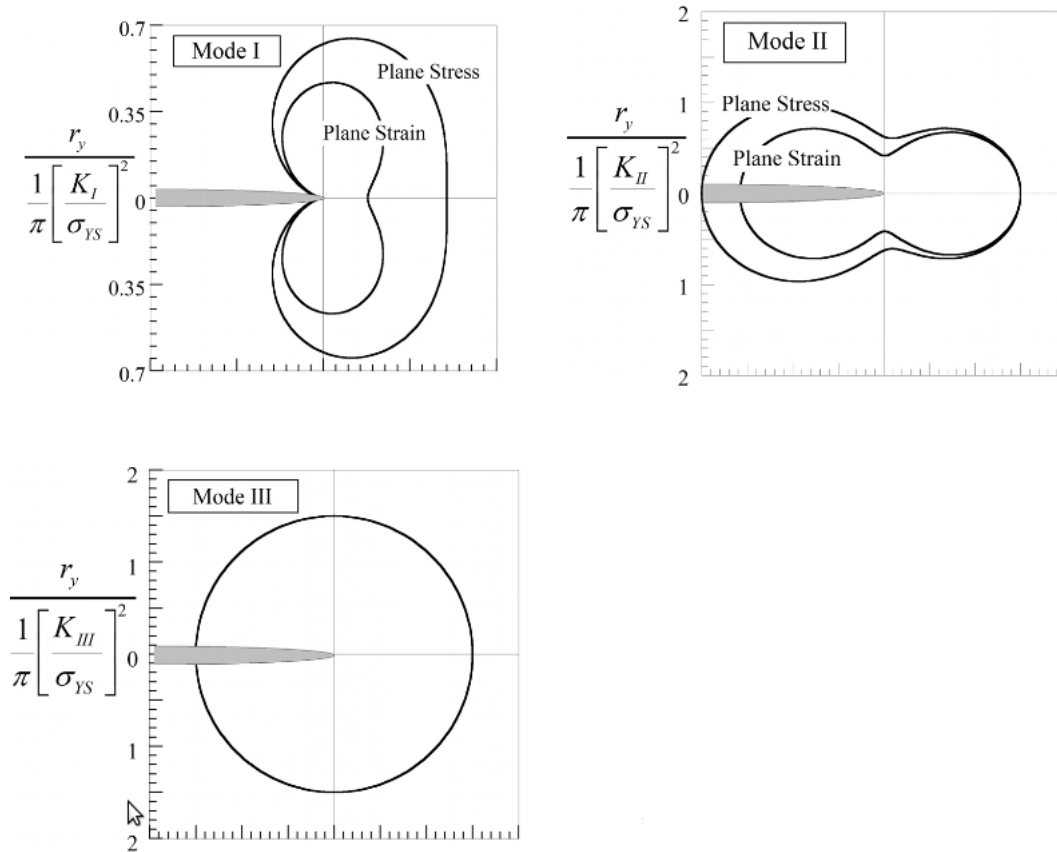Figure 2.14: Crack-tip plastic zone shapes estimated with the Von Mises yield criterion for modes I, II and III. [8]
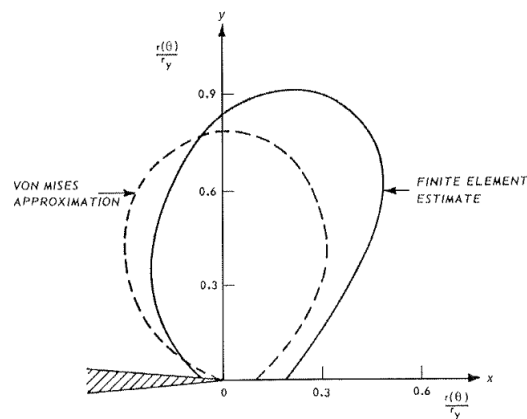

Figure 2.15: Comparison of plane strain plastic zone size and shape estimates for an elastic-perfectly plastic material. [7]

significant difference in the size and shape of the Mode I plastic zones for plane stress and plane strain is due that the latter condition suppressing yielding, resulting in a

smaller plastic zone for a given KI value.

The plastic zones in equations 2.32 and 2.33, and in figure 2.14 are also not exactly correct since the redistribution of stress field above σ_{ys} has not been taking into account. Von mises yield criterion and a FEM estimate, in which the stress field redistribution (due to strain hardening) has been taking into account, for plastic zone size are compared in figure 2.15.

2.1.1 Critical Fracture Toughness

As discussed above, material behavior in cracked linear-elastic materials can be completely defined by one parameter, K_K. Hence, because every material fails locally at a certain combination of stresses and strains, a critical SIF, K_c, determines the value when the crack extends. This material constant, K_c, can be often considered independent of the size and geometry of the cracked body.

Although, K_c is independent of geometry the thickness has an effect to it. A fracture toughness tests on very thin plates usually results in a 45° shear fracture. At larger thicknesses, there is generally some mixture of shear and flat fracture. The thickness effect to the apparent fracture toughness is due to the relative portions of flat and shear fracture. In the limit of a very thick specimen, the flat fracture mechanism dominates, and further increase in thickness have relatively little effect on the measured toughness. This kind a material behavior usually correspond to materials in which the crack propagation is ductile (microvoid coalescence). The crack grows preferentially in the region of high triaxiality. Crack growth on the outer regions of the specimen lags behind, and occurs at a 45° angle to the applied load. The resulting fracture surface exhibits a flat region in the central region and 45° shear lips on the edges (figure 2.16).
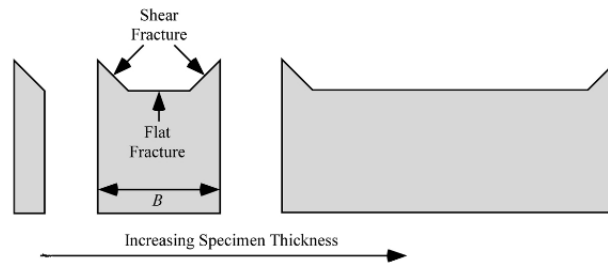
Figure 2.16: Effect of specimen thickness on fracture surface morphology for materials that exhibit ductile crack growth. [8]

The trend in critical fracture toughness level does not indicate a transition from a plane-stress-fracture to a plane-strain-fracture, as was attributed in the past. Although, the behavior is related to the crack-tip stress state, the traditional plane stress plane strain transition model is too simplistic. Rather, it reflects a two distinct fracture mechanisms. In fact, there are no plane-stress-fractures except for example in thin sheet like structures. There is almost always a state of plain strain in front of the crack.

In materials that fail by cleavage fracture usually do not form shear lips, so the phenomena discussed above do not apply to them. Although cleavage fracture toughness does exhibit a slight thickness dependence due to weakest link sampling effects.

2.2 EPFM

As discussed above LEFM describes crack growth and fracture in materials under loading conditions, where only a small region around crack tip is plastically deformed. However, very few materials in practice behave in this way. This leaves out many materials that are too ductile and the crack tip plasticity is too extensive. For predicting fractures in these material, alternatively fracture mechanics methods are needed.

Elastic-plastic fracture mechanics applies to materials that exhibit time-independent, nonlinear behavior (i.e. plastic deformation). Rice [4] provided the basis for extending fracture mechanics analysis beyond the validity limits of LEFM [14]. Rice also introduced a material parameter for EPFM, the contour integral J, which describes crack tip conditions in elastic-plastic materials, hence it can be used as a material parameter. Critical values of J give nearly size-independent measures of fracture toughness, even for relatively large amounts of crack-tip plasticity. There are limits to the applicability of J (e.g. plastic collapse, where the whole body is plastically deformed, which is yielding dominated failure mode), but these limits are much less restrictive than the validity requirements of LEFM. Also other fracture parameters are developed to describe nonlinear material behavior (e.g. CTOD), but the J integral is most widely accepted.

2.2.1 The J Integral

Rice provided the basis for extending fracture mechanics methodology to nonlinear material behavior by idealizing elastic-plastic deformation as nonlinear elastic deformation. In figure 2.17 the uniaxial stress-strain behavior of both elastic-plastic and nonlinear elastic materials is plotted . At seen the material behavior differs only in the unloading part of the curves. As The elastic-plastic material follows a linear unloading path with the slope equal to Young's modulus, the nonlinear elastic material unloads along the loading path.

Deformation theory of plasticity, which relates total strains to stresses in a material, is equivalent to nonlinear elasticity.

Rice also applied deformation plasticity (i.e. nonlinear elasticity) to the analysis of a crack in a nonlinear material. He showed that the nonlinear energy release rate J could be written as a path-independent line integral. Hutchinson [15] and Rice and Rosengren [16] also showed that J uniquely characterizes crack-tip stresses and strains in nonlinear materials. Thus the J integral can be viewed as both an energy parameter and a stress intensity parameter.

Rice showed that the value of the J integral is independent of the path of integration around the crack. Therefore J is called a path-independent integral (figure 2.18).
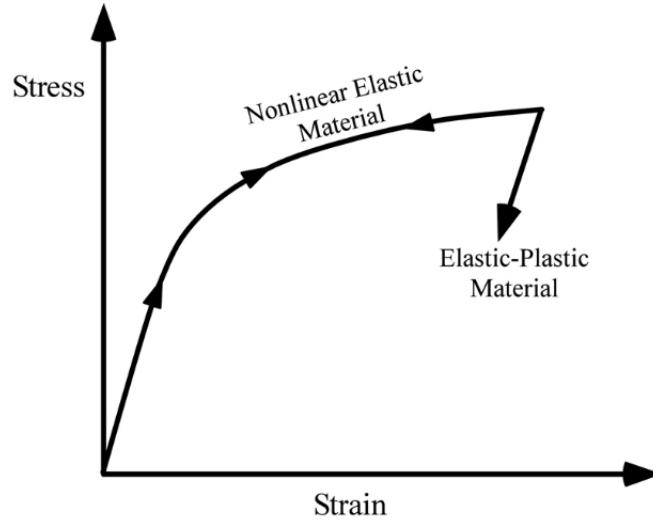
Figure 2.17: Schematic comparison of the stress-strain behavior of elastic-plastic and nonlinear elastic materials. [8]
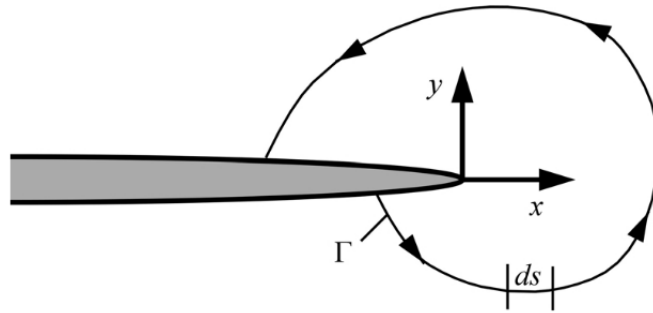
Figure 2.18: A contour around the tip of a crack. [8]

The J integral in figure 2.18 is given by

$$J = \int_{\Gamma} (wdy - T_i \frac{\partial u_i}{\partial x} ds) \tag{2.34}$$

where ds is length increment along the contour Γ, T_i are components of the traction vector, u_i are displacement vector components, and w is strain energy density defined as

$$w = \int_0^{\varepsilon_{kl}} \sigma_{ij} d\varepsilon_{ij} \tag{2.35}$$

where σ_{ij} and ε_{ij} are the stress and strain tensors, respectively, and ε_{kl} is the total strain. The components of the traction vector are given by

$$T_i = \sigma_{ij} n_j \tag{2.36}$$

18

where n_j are the components of the unit vector normal to Γ.

The crack tip stresses and strains can be expressed in terms of J according to the HRR (after Hutchinson and Rice and Rosengren) solution

$$\sigma_{ij} = \sigma_0 \left(\frac{EJ}{\alpha \sigma_0^2 I_n r}\right)^{\frac{1}{n+1}} \overline{\sigma}_{ij}(\theta, n), \tag{2.37a}$$

$$\varepsilon_{ij} = \alpha \frac{\sigma_0}{E} \left(\frac{EJ}{\alpha \sigma_0^2 I_n r}\right)^{\frac{1}{n+1}} \overline{\varepsilon}_{ij}(\theta, n). \tag{2.37b}$$

In which I_n is a dimensionless constant depending the strain hardening constant n and stress and strain relationship is given by a Ramberg-Osgood relation

$$\frac{\varepsilon}{\varepsilon_o} = \frac{\sigma}{\sigma_0} + \alpha \left(\frac{\sigma}{\sigma_0}\right)^n. \tag{2.38}$$

In equations 2.37 and 2.38 α is a dimensionless constant, and $\varepsilon_0 = \sigma_0/E$ with σ_0 usually equal to the yield stress. $\overline{\sigma}_{ij}$ and $\overline{\varepsilon}_{ij}$ are are dimensionless functions of n, angle θ, and the stress state.

The J integral defines the amplitude of the HRR singularity, just as the stress intensity factor characterizes the amplitude of the linear elastic singularity. Thus J completely describes the conditions within the plastic zone. A structure in small-scale yielding has two singularity-dominated zones: one in the elastic region, where stress varies as $1/\sqrt{r}$, and one in the plastic zone where stress varies as $r^{1/(n+1)}$. The latter often persists long after the linear elastic singularity zone has been destroyed by crack-tip plasticity. When $n = 1$ equations 2.37 show $1/\sqrt{r}$ singularity which is consistent with LEFM and can be shown to become identical to equations 2.9.

The HRR singularity contains the same anomaly as the LEFM singularity, both predict infinite stresses as $r \to 0$. However, in reality the singular field does not persist all the way to the crack tip. The large strains at the crack tip cause the crack to blunt, which reduces the stress triaxiality locally. The blunted crack tip is a free surface; thus σ_{xx} must vanish at $r = 0$.

2.3 Crack growth criterion

Many different criteria have been developed to predict mixed mode crack propagation. Most of them are based on LEFM and they are the form

$$f(K_I, K_{Icrit}, K_{II}, K_{IIcrit}) = 0, \tag{2.39}$$

where K_{Icrit}, K_{IIcrit} are experimentally measured fracture toughnesses of the modes I and II, respectively. Usually only mode I fracture toughness is measured, and hence the criterion 2.39 is simplified to

$$f(K_I, K_{Icrit}, K_{II}) = 0. \tag{2.40}$$
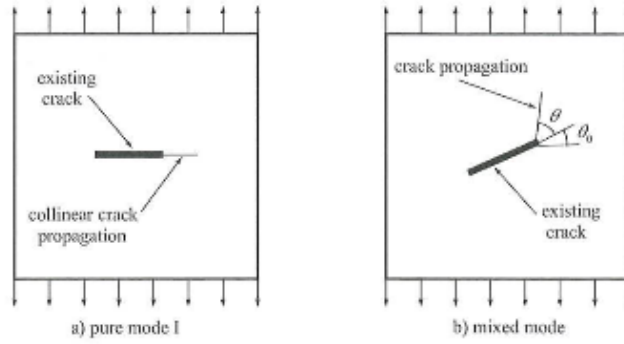
Figure 2.19: Mixed mode crack propagation. [6]

Couple of the most widely used ones are:

- Zero K_{II} criterion [17], where the angle (figure 2.19) of crack growth is calculated by setting K_{II} to zero.

- Maximum circumferential tensile stress criterion [18], where the angle (figure 2.19) of crack growth is calculated by

$$\frac{K_I}{K_{Icrit}}\cos^3\frac{\theta}{2} - \frac{2}{3}\frac{K_{II}}{K_{Icrit}}\cos\frac{\theta}{2}\sin\theta = 1. \tag{2.41}$$

The angle is calculated by modifying the equation 2.41 to

$$\sigma_\theta = \frac{1}{\sqrt{2\pi r}}\cos\frac{\theta}{2}[K_I\cos^2\frac{\theta}{2} - K_{II}\sin\theta] \tag{2.42}$$

θ can be solved by finding the root of the derivative of the equation 2.42 with respect to θ. this yields

$$\cos\frac{\theta}{2}[K_I\sin\theta + K_{II}(3\cos\theta - 1)] \tag{2.43}$$

(a) Positive σ_{xy}. (b) Negative σ_{xy}.
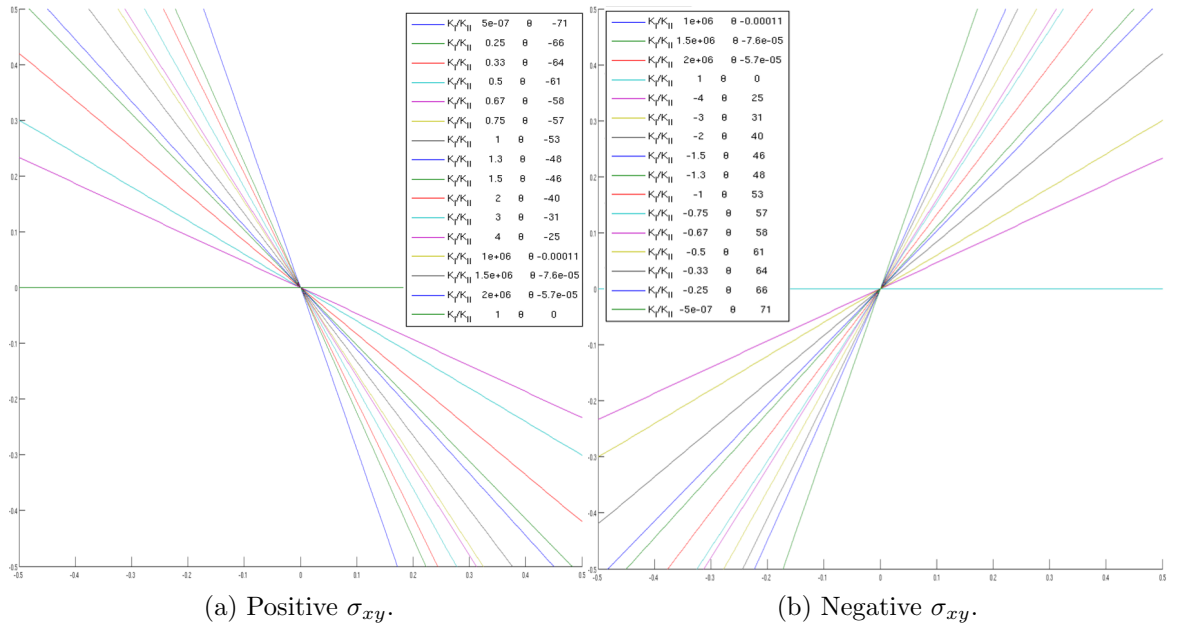
Figure 2.20: Angles predicted by maximum circumferential tensile stress criterion with varying K_I/K_{II} ratio.

Angles predicted by different $\frac{K_I}{K_{II}}$-ratios according to equation 2.43 are plotted in figure 2.20. The angles in figure 2.20 are presented as integers. Crack initiation angle predicted by maximum circumferential tensile stress criterion for pure mode II crack growth is 70.5°, for pure mode I the angle is 0, and for mixed mode (when $K_I = K_{II}$) is 53.1°.

3

FEM

Many phenomena in nature can be depicted with partial differential equations (PDEs). PDEs are equations that consists of a relation involving a function (or functions) of several independent variables and its (or their) partial derivatives with respect to those variables. These PDEs are divided into three main types: elliptic, parabolic and hyperbolic equations. Common examples of the equations are: equation of equilibrium, evolution problems and wave equations respectively.

Finding an exact, analytical, solution to a PDE is often impossible, thus many numerical solution routines have been developed. Nowadays, the most popular and efficient tool to solve PDEs, especially for elliptic problems, is FEM. FEM is based on a weak form of the problem and it has a sound theoretical background.

Since the FEM is such a vast field, it can only be treated to a certain extent in this work. For more comprehensive treatment of FEM can be found in [19],[20] and [21]. Solving problems with FEM includes usually following four steps:

1. Variational formulation for the given problem

2. Discretization using FEM

3. Solution of the discrete problem

4. Implementation of the method on a computer problem

The following presentation follows the one presented in [19].

3.1 Variational Formulation

Strong form of a typical (stationary) boundary value problem (the Poisson equation figure 3.1) in mechanics is

$$-\triangle u = f \quad \text{in } \Omega, \tag{3.1a}$$

$$u = u_0 \quad \text{on } \Gamma, \tag{3.1b}$$

where

$$\triangle u = \frac{\partial^2 u}{\partial x_1^2} + \frac{\partial^2 u}{\partial x_2^2}, \tag{3.2}$$

$u_o = 0$, Ω is bounded open domain in the plane, and Γ is the boundary.
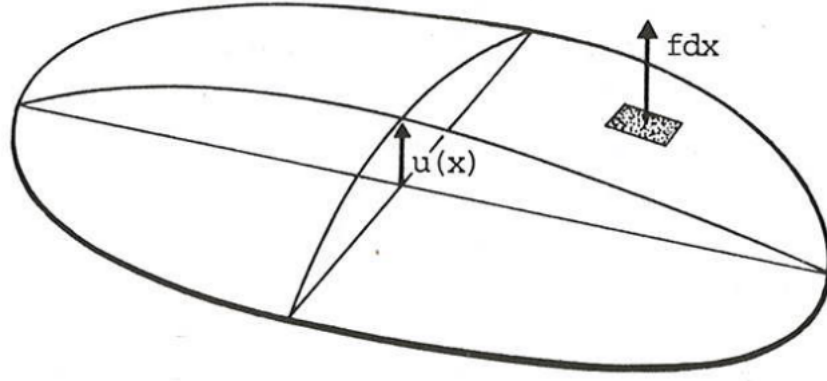
Figure 3.1: Displacement, $u(x)$, of a membrane under a load intensity, f. [19]

Firstly, the given PDE is reformulated into equivalent variational problem in order to form the weak form of the problem. In the case of elliptic problem it is a minimization problem of the form

$$\text{Find } u \; \epsilon \; V \text{ such that} F(u) \leq F(v) \; \forall \, v \; \in \; V, \tag{3.3}$$

in which V is a given set of acceptable functions and $F(v) \in \mathbb{R}$ for all $v \in V$ with $\mathbb{R}$ denoting the set of real numbers. Functions v in V represents continuously varying quantity e.g. a displacement in an elastic body. $F(v)$ is the total potential energy associated with v. The equation 3.3 states that the function u gives the absolute minimum of the total energy when v represents all the functions in space V.

The linear functional $F(v)$ is the total potential energy of the system and its definition is

$$F(v) = \frac{1}{2}a(v,v) - (f,v), \tag{3.4}$$

where

$$a(v,v) = \int_{\Omega} \nabla v \cdot \nabla v \, d\Omega, \tag{3.5}$$

is the internal elastic energy and

$$(f,v) = \int_{\Omega} f \cdot v \, d\Omega, \tag{3.6}$$

is the load potential, f being the load intensity and v the displacement. ∇ operator is

$$\nabla v = (\frac{\partial v}{\partial x_1}, \frac{\partial v}{\partial x_2}) \tag{3.7}$$

It can be shown that if u satisfies 3.1, then u is the solution of the next variational problem

$$\text{Find } u \in V \text{ such that } a(u,v) = (f,v) \, \forall \, v \; \in \; V, \tag{3.8}$$

where

$$V = \{v : v \text{ is continuous on } \Omega, \frac{\partial v}{\partial x_1} \text{ and } \frac{\partial v}{\partial x_2} \tag{3.9}$$
$$\text{are piecewise continuous on } \Omega \text{ and } v = 0 \text{ on } \Gamma\}.$$

23

3.2 Discretization

In order to formulate the function, which gives the solution for the problem in hand, the area needs to be divided into elements, this process is referred as discretization or meshing. Elements shape can be any polygonal form, although, they usually are either triangles or rectangles.

For simplicity the domain Ω in figure 3.1 is assumed to be polygonal and the boundary Γ polygonal curve. Often the boundary of the domain of interest is curved, hence Γ defined in this manner is only an approximation. Accuracy of the solution can be increased by increasing element quantity - diminishing the size of the elements along the boundary or using isoparametric elements. Finite dimensional subspace $V_h \in V$ is done by triangulating the domain Ω, by subdividing it into a set $T_h = K_1, ..., K_m$ of non-overlapping triangles K_i,

$$\Omega = \cup_{K \in T_h} K = K_1 \cup K_2 ... \cup K_m, \tag{3.10}$$

such that no vertex of one triangle lies on the edge of another triangle (figure 3.2). V_h is defined
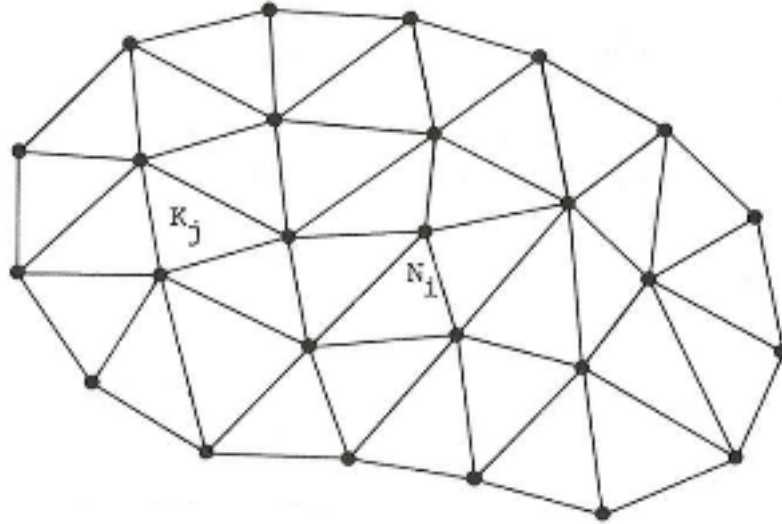
Figure 3.2: Trangulation of the area in the figure 3.1 . [19]

$$V_h = v : v \text{ is continuous on } \Omega, \ v|_k \text{ is linear } \forall \ K \in T_h \ , v = 0 \text{ on } \Gamma, \tag{3.11}$$

where $v|_k$ denotes the restriction of v to K, i.e.,the function defined on K agreeing with v on K. The space V_h consists of all the continuous functions that are linear on each triangle K and vanish on Γ. Values $v(N_i)$ are chosen as parameters to describe function $v \in V_h$ at nodes N_i $(i = 1, \ldots, M)$ of T_h (figure 3.2), the nodes on Γ are excluded since $v = 0$ on Γ. The corresponding shape functions $\phi_j \in V_h$ $(J = 1, ..., M)$ are defined by (figure 3.3)

$$\phi_j(N_i) = \delta_{ij} \equiv \begin{cases} 1 & \text{if } i = j \\ 0 & \text{if } i \neq j \end{cases} \tag{3.12}$$

Points x for which $\phi(x) \neq 0$ consists of the triangles with the common node N_j
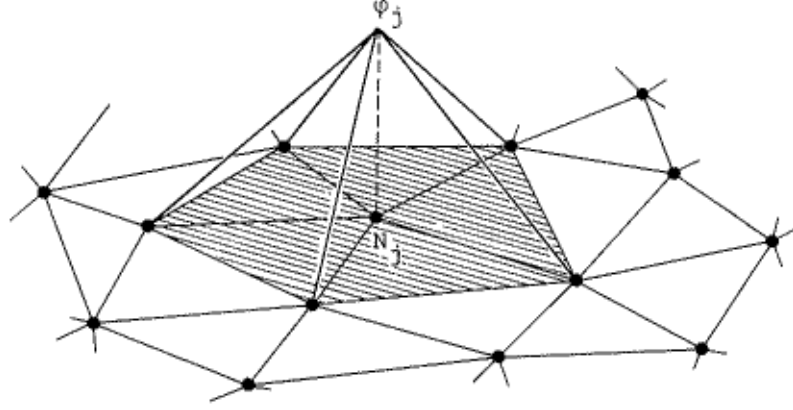
Figure 3.3: The shape functions ϕ_j of the node N_j. [19]

(shaded area in figure 3.3). Shape functions ϕ_i satisfy a condition of partition of unity

$$\sum_{i=1}^{n} \phi_i(N_j) = 1, \tag{3.13}$$

where n is the number of nodes for each element. A function $v \in V_h$ is now

$$v(x) = \sum_{j=1}^{M} \eta_j \phi_j(x), \ \eta_j = v(N_j), \ \text{for } x \in \Omega \cup \Gamma, \tag{3.14}$$

Finite element method can now be formulated for equation 3.1 starting from the variational formulation 3.8:

$$\text{Find } u_h \in V_h \text{ such that } a(u_h, v) = (f, v) \ \forall \, v \, \in \, V_h, \tag{3.15}$$

The equation 3.15 is equivalent to the linear system of equations

$$A\xi = b, \tag{3.16}$$

where $A = (a_{ij})$ is the $(M \times M)$ stiffness matrix with elements $a_{ij} = a(\phi_i, \phi_j)$, and $\xi = \xi_i$ and $b = b_i$ are M-vectors with elements $\xi_i = u_h(N_i), b_i = (f, \phi_i)$. Since A is symmetric and can be shown to be positive defined, a unique solution ξ exists. Furthermore, matrix A is sparse; if N_i and N_j are not nodes of the same triangle, $a_{ij} = 0$.

3.3 Error Estimate

As a result of finite element problem formulation the result will be approximate, and as such, some error $u - u_h$, where $u \in V$, $u_h \in V_h$, and $V_h \subset V$, will be caused. A

quantitative estimate for the error $\|(u - u_h)'\|$ is obtained by estimating $\|(u - \overline{u}_h)'\|$. $\overline{u}_h \in V_h$ interpolates u at the nodes x_j (figure 3.4), i.e.

$$\overline{u}_h(x_j) = u(x_j) j = 0, ..., M + 1, \tag{3.17}$$

where M is the number of nodes. When $\overline{u}_h \in V_h$ is chosen this way, then for $0 \leq y \leq 1$,
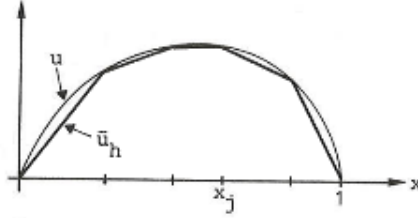
Figure 3.4: The interpolant $\overline{u}_h$. [19]

$$|u'(x) - \overline{u}'_h(x)| \leq h \max_{0 \leq y \leq 1} |u''(y)|, \tag{3.18}$$

and

$$|u(x) - \overline{u}_h(x)| \leq \frac{h^2}{8} \max_{0 \leq y \leq 1} |u''(y)|, \tag{3.19}$$

the error estimate $(u - u_h)$ can be obtained from equation 3.18 by using Cauchy's inequality

$$|(v, w)| \leq \|v\| \|w\| \tag{3.20}$$

and the following theorem

$$\|(u - u_h)'\| \leq |(u - v)|. \tag{3.21}$$

These lead to the error estimate

$$\|(u(x) - u_h(x))\| \leq h \max_{0 \leq y \leq 1} |u''(y)|. \tag{3.22}$$

Since $(u(x) - u_h(x))(0) = 0$ the error estimate for $u(x) - u_h(x)$ is obtained:

$$|u(x) - u_h(x)| \leq h \max_{0 \leq y \leq 1} |u''(y)|, \text{ for } 0 \leq y \leq 1. \tag{3.23}$$

The error estimate is less sharp than the estimate 3.19, where a factor h^2 persists. With a more precise analysis the estimate for the error $u - u_h$ can be shown to have also the factor h^2. The Theorem 3.21 shows that $\|(u - u_h)'\|$ is as small as possible, and equation 3.22 shows that the error tends to zero as the maximum length of subintervals tends to zerpo, if u'' is bounded on [0,1].

Since the triangles $K \in T_h$ are not allowed to be too thin the error estimate for FEM problem 3.15 can be shown to be

$$\|\nabla u(x) - \nabla u_h(x)\| \leq Ch, \tag{3.24}$$

26

where C is a positive constant, that might be different at different occurrences and does not depend on the mesh parameter h. In this case (3.24) the constant C depends on the size of the second partial derivatives of u and the smallest angle of triangles $K \in T_h$. It is also possible to prove that the error $u(x) - u_h(x)$ is as follows

$$\|u(x) - u_h(x)\| \leq Ch^2. \tag{3.25}$$

In particular these estimates shows that if the exact solution u is regular enough, the error and the gradient of the error $u(x) - u_h(x)$ in the norm $\| \cdot \|$ tend to zero as h tends to zero.

3.4   The Hilbert Spaces $\mathbf{L}^2 (\Omega)$, $\mathbf{H}^1 (\Omega)$, $\mathbf{H}_0^1 (\Omega)$

When a boundary value problem is formulated as a variational formulation, it is useful to work with function spaces that contain slightly more functions than the spaces of continuous functions with piecewise continuous derivatives used above (function spaces V and V_h). It is also useful to enrich the spaces V with various scalar products by adding scalar product which is related to the boundary value problem. Which makes V a Hilbert space.

Hilbert spaces $L_2 (\Omega)$, $H^1 (\Omega)$, $H_0^1 (\Omega)$ are defined as follows (Ω is now a bounded domain in $\mathbb{R}^n$, $d = 2$ or 3):

$$L_2(\Omega) = \{v : v \text{ is defined on } \Omega \text{ and } \int_\Omega v^2 \, dx < \infty\}, \tag{3.26a}$$

$$H^1(\Omega) = \{v \in L_2(\Omega) : \frac{\partial v}{\partial x_i} \in L_2(\Omega), i = 1, ..., d\}, \tag{3.26b}$$

$$H_0^1(\Omega) = \{v \in H^1(\Omega) : v = 0 \text{ on } \Gamma\}, \tag{3.26c}$$

the corresponding scalar products and norms are:

$$(v, w) = \int_\Omega v \, w \, dx, \tag{3.27a}$$

$$\|v\|_{L_2(\Omega)} = (\int_\Omega v^2 \, dx)^{1/2}, \tag{3.27b}$$

$$(v, w)_{H(\Omega)} = \int_\Omega [v \, w + \nabla v \cdot \nabla w] dx, \tag{3.27c}$$

$$\|v\|_{H(\Omega)} = (\int_\Omega [v + |\nabla v|^2] \, dx)^{1/2}, \tag{3.27d}$$

where H is either H^1 or H_0^1. The norm associated whit scalar product is defined by

$$\|v\|_a = (a(v, v))^{1/2}, \forall v \in \text{V}. \tag{3.28}$$

The boundary value problem 3.1 can now be given the following variational formulation:

$$\text{Find } u \in H_0^1(\Omega) \text{ such that } a(u, v) = (f, v) \, \forall \, v \in H_0^1(\Omega). \tag{3.29}$$

It is meaningful to use the "right" function space. This makes it easier to prove the existence of solution to the continuous problem and also the error estimate for FEM is an estimate of the norm used in variational formulation.

3.5 Boundary Conditions

Two most common types of boundary conditions are a Neumann condition and the one used above ($u = u_0$ on Γ, where u_0 is the value of u at the boundary Γ), which is called Dirichlet condition. As example of a problem with a Neumann boundary condition consider the following:

$$-\triangle u + u = f \quad \text{in } \Omega, \tag{3.30a}$$

$$\frac{\partial u}{\partial n} = g \quad \text{on } \Gamma, \tag{3.30b}$$

where $\frac{\partial}{\partial n}$ denotes the outward normal derivative to Γ. The Neumann boundary condition corresponds the force or flow g on Γ.

The variational form of equations 3.30 is

$$\text{Find } u \in H^1(\Omega) \text{ such that } (u, v) = (f, v) + \langle g, v \rangle \ \forall v \in H(\Omega), \tag{3.31}$$

where $\langle g, v \rangle = \int_\Gamma gv\, ds$. The Neumann condition is not explicitly in the variational form, because the variational form's solution, u, belongs only to $H(\Omega)$, and thus it is necessary to satisfy equation 3.30b. Instead the boundary condition is implicitly included equation 3.31, and such a boundary condition is called a natural boundary condition. Where as boundary condition in equation 3.1 is an essential boundary condition, which has to be explicitly satisfied in the variational formulation.

For formulating a FEM for the Neumann problem, 3.30, the triangulation, T_h of Γ is defined

$$V_h = v : v \text{ is continuous on } \Omega, \ v|_k \text{ is linear } \forall\, K \in T_h. \tag{3.32}$$

The nodal values that are the parameters describing the functions in V_h now also includes the nodes on the boundary Γ. Hence, the FEM for equation 3.30 is

$$\text{Find } u_h \in V_h \text{ such that } (u_h, v) = (f, v) + \langle g, v \rangle \ \forall v \in V_h. \tag{3.33}$$

The error estimate for equation 3.33 is

$$\|u - u_h\|_{H^1(\Omega)} \le \|u - v\|_{H^1(\Omega)} \tag{3.34}$$

and as above

$$\|u - u_h\|_{H^1(\Omega)} \le Ch, \tag{3.35}$$

if u is enough regular, $\frac{\partial u_h}{\partial n}$ will be an approximation to g on Γ Other types of boundary conditions exist, like a Robin type $\gamma u + \frac{\partial u}{\partial n} = g$ on Γ, where γ is a constant, but they are usually combinations of the first two and rarer.

3.6 The Elasticity Problem

A homogeneous isotropic elastic body (figure 3.5) is occupying a bounded domain $\Omega \subset \mathbb{R}^3$. Boundary Γ of the body is composed of two parts Γ_1 and Γ_2. The body is acted upon by a volumetric load f_i and a boundary load g_i on Γ_1, where indexes $_i$ are the components in the x_i direction ($_i = x, y, z$). The body is fixed along boundary Γ_2
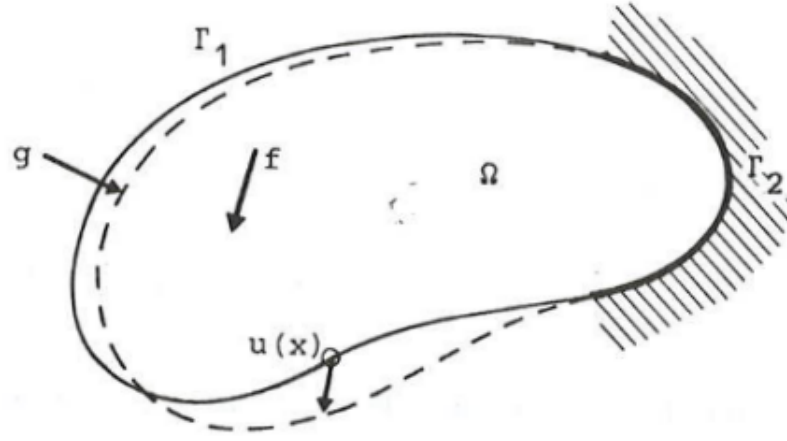
Figure 3.5: An elastic bounded body. [19]

To solve the elastic problem one has to determine the displacement u_i and the stress state σ_{ij} ($i, j = x, y, z$), under the loads f and g. u_i is the displacement in the x, y or z-direction, σ_{ii} is the normal stress, and the σ_{ij}, $i \neq j$, are the shear stresses. Further, $\varepsilon(u) = \varepsilon_{ij}(u)$, where

$$\varepsilon_{ij} = \frac{1}{2}\left(\frac{\partial u_i}{\partial x_j} + \frac{\partial u_j}{\partial x_i}\right), \tag{3.36}$$

is the deformation tensor associated with the displacement u. assuming small deformations/displacements the following constitutive relations (Hooke's law) hold

$$\sigma_{ij} = \lambda \nabla \cdot u \, \delta_{ij} + \mu \, \varepsilon_{ij}(u), \tag{3.37}$$

where λ and μ are Lamé coefficients

$$\mu = \frac{E}{1 + \nu}, \tag{3.38a}$$

$$\lambda = \frac{E\nu}{(1 + \nu)(1 - 2\nu)}, \tag{3.38b}$$

where E is the Young's modulus and ν is Poisson's ratio, and divergence and Dirac delta are as follows

$$\nabla \cdot u = \sum_{i=1}^{3} \frac{\partial u_i}{\partial x_i}, \tag{3.39a}$$

$$\delta_{ij} = \begin{cases} 1 & \text{if } i = j \\ 0 & \text{if } i \neq j \end{cases} \tag{3.39b}$$

The equilibrium equations for problem in hand are

$$-\sum_{j=1}^{3} \frac{\partial \sigma_{ij}}{\sigma x_j} = f_i, \; in \; \Omega, \tag{3.40}$$

29

and the boundary conditions are

$$\sum_{j=1}^{3} \sigma_{ij} n_j = g_i, \tag{3.41a}$$

$$u = 0 \text{ on } \Gamma_2, \tag{3.41b}$$

where n_j is the outward normal to Γ.

The variational formulation for the elastic problem in hand is given by

$$\text{Find } u \in V \text{such that } a(u,v) = L(v) \,\forall\, v \in\, V, \tag{3.42}$$

where

$$a(u,v) = \int_{\Omega} [\lambda \,\nabla \cdot\, u \,\nabla \cdot\, v + \mu\varepsilon_{ij}(u)\varepsilon_{ij}(v)]dx, \tag{3.43a}$$

$$L(v) = \int_{\Omega} f_i v_i \, dx + \int_{\Gamma_1} g_i v_i \, ds, \tag{3.43b}$$

$$V = v \in [H^1(\Omega)]^3 : v = 0 \text{ on } \Gamma_2. \tag{3.43c}$$

The procedure to solve the FEM problem continues with discretization of the domain as in section 3.2.

3.7   Isoparametric Elements

To achieve a higher order of approximation the boundary can be approximated with piecewise polynomials of degree $k \geq 2$. Hence, in the meshed region, Ω, the elements close to the boundary will have one curved side (figure 3.6).
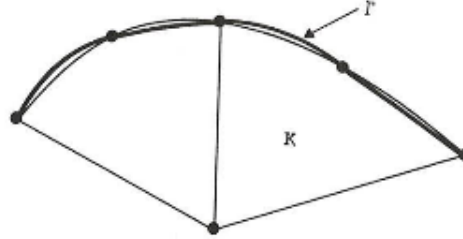
Figure 3.6: Triangular elements on a curved boundary. [19]

A curved element is obtained in principle the following way: $\hat{F}$ is a one-to-one mapping of the reference triangle, $\hat{K}$, in the $(\hat{x}_1,\hat{x}_2)$-plane onto the curved triangle K in the (x_1,x_2)-plane (figure 3.7). For simplicity elements degrees of freedom are of Lagrange type (i.e. a set of shape functions values at certain points $\hat{a}^i \in \hat{K}$, $i = 1,...,m$.

The finite element space, P_K is

$$P_K = p : p(x) = \hat{p}(\hat{F}^{-1}(x)), x \in K, \hat{p} \in P_{\hat{K}}. \tag{3.44}$$
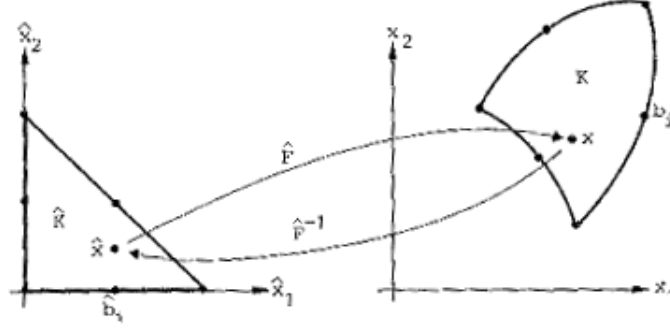
Figure 3.7: Triangular elements on a curved boundary. [19]

The functions $p \in P_K$ are defined through the inverse mapping $\hat{F}^{-1} : K \to \hat{K}$ and the polynomial functions $\hat{p} : \hat{K} \to R$, $\hat{p} \in P_K$. If the mapping $\hat{F} = (\hat{F}_1, \hat{F}_2)$ is of the same type as the functions in P_k the element is isoparametric. The transformation F is

$$\hat{F}(\hat{x}) = \sum_{j=1}^{6} a^j \hat{\phi}_j(\hat{x}), \hat{x} \in \hat{K}, \tag{3.45}$$

where a^j are the node locations in figure 3.7 and the element K is

$$K = \hat{F}(\hat{K}) = x \in R^2 : x = \hat{F}(\hat{x}), \hat{x} \in \hat{K}. \tag{3.46}$$

With equations 3.45 and 3.46 the points $\hat{a}^j$ in the $\hat{x}$-plane are mapped onto the points a^j in the x-plane.

The mapping F is locally one-to-one in small neighborhood of each point $\hat{x} \in \hat{K}$ if

$$\det J(\hat{x}) \neq 0, \hat{x} \in \hat{K}, \tag{3.47}$$

where

$$J = \begin{bmatrix} \frac{\partial F_1}{\partial \hat{x}_1} & \frac{\partial F_1}{\partial \hat{x}_2} \\ \frac{\partial F_2}{\partial \hat{x}_1} & \frac{\partial F_2}{\partial \hat{x}_2} \end{bmatrix} \tag{3.48}$$

is the Jacobian of F and det J is the determinant of J.

The stiffness matrix is computed in the following way: The local shape functions on K are given by

$$\phi_j(x) = \hat{\phi}_j(F^{-1}(x)), j = 1, \ldots, 6, \tag{3.49}$$

where $\hat{\phi}_j$, $j = 1, .., 6$ is a usual shape function for $P_{\hat{K}} \equiv P_2(\hat{K})$. For the Poisson equation 3.1 the following integrals has to be calculated

$$a_{ij}^K = \int_K \nabla \phi_i \cdot \nabla \phi_j dx, i, j = 1, \ldots, 6, \tag{3.50}$$

where

$$\nabla \phi_i = J^{-T} \nabla \hat{\phi}_i, \tag{3.51}$$

where

$$J^{-T} = \begin{bmatrix} \frac{\partial \hat{x}_1}{\partial x_1} & \frac{\partial \hat{x}_2}{\partial x_1} \\ \frac{\partial \hat{x}_1}{\partial x_2} & \frac{\partial \hat{x}_2}{\partial x_2} \end{bmatrix}. \tag{3.52}$$

The transformation of the integral in equation 3.50 to an integral over $\hat{K}$ using the mapping $\hat{F} : \hat{K} \to K$ produces

$$a_{ij}^K = \int_K (J^{-T} \nabla \hat{\phi}_i) \cdot (J^{-T} \nabla \hat{\phi}_j) |\det J| d\hat{x}. \tag{3.53}$$

Further, by simple calculation

$$J^{-T} = (J^{-1})^T = \frac{1}{\det J} J_0, \tag{3.54}$$

where

$$J_0 = \begin{bmatrix} \frac{\partial \hat{F}_2}{\partial \hat{x}_2} & -\frac{\partial \hat{F}_2}{\partial \hat{x}_1} \\ -\frac{\partial \hat{F}_1}{\partial \hat{x}_2} & -\frac{\partial \hat{F}_1}{\partial \hat{x}_1} \end{bmatrix}, \tag{3.55}$$

so that finally

$$a_{ij}^K = \int_{\hat{K}} (J_0 \nabla \hat{\phi}_i) \cdot (J_0 \nabla \hat{\phi}_j) \frac{d\hat{x}}{|\det J|}. \tag{3.56}$$
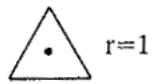
Thus the matrix element a_{ij}^K can be computed by evaluating an integral over the reference element $\hat{K}$.
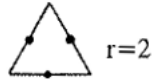
3.8   Quadrature

The integrand in the stiffness matrix elements in equation 3.56 is usually difficult to evaluate exactly. The same difficulty arouses in nonlinear problems and differential equations with variable coefficients. Numerical quadrature formulas are developed to evaluate such integrals. Some quadratures are presented in figure 3.8. In figure 3.8 r indicates the maximal degree of the polynomials for which the formula is exact. Furthermore, a^i (i=1,2,3) are the vertices of the triangle K, b^j(j=1,2,3) denote the midpoint of the side K and a^{123} the center gravity of K. Q denote a rectangle with sides parallel to the coordinate axis of lengths $2h_1$ and $2h_2$ and center at the origin.
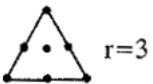
3.9   Hierarchical elements

When refining elements of standard shape functions 3.14 all calculations need to be repeated, since a set of totally new shape functions needs to be generated. A way around this drawback is to consider the shape functions as a series in which the shape function ϕ_i does not depend on the number of nodes N_j in the mesh. This is achieved using hierarchic shape functions. The hierarchic concept is illustrated by the one-dimensional problem in figure 3.9. In standard elements η is the "height" of the approximation while in hierarchical elements $\eta^\star$ is the difference of "heights" of the parent shape function and hierarchical shape function.

$$\int_K f\,dx \sim f(a^{123})\,\text{area}(K)$$

$$\int_K f\,dx \sim \sum_{j=1}^{3} f(b^j)\,\frac{\text{area}(K)}{3}$$

$$\int_K f\,dx \sim \sum_{j=1}^{3} \left[f(a^j)\,\frac{\text{area}(K)}{20} + f(b^j)\frac{2\;\text{area}(K)}{15} \right]$$
$$+ f(a^{123})\frac{9\;\text{area}(K)}{20}$$

$$\int_Q f\,dx \sim \left[f\!\left(\frac{h_1}{\sqrt{3}},\frac{h_2}{\sqrt{3}}\right) + f\!\left(\frac{h_1}{\sqrt{3}},-\frac{h_2}{\sqrt{3}}\right) + f\!\left(-\frac{h_1}{\sqrt{3}},\frac{h_2}{\sqrt{3}}\right) \right.$$
$$\left. + f\!\left(-\frac{h_1}{\sqrt{3}},-\frac{h_2}{\sqrt{3}}\right) \right]\frac{\text{area}(Q)}{4}.$$
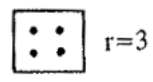
Figure 3.8: Some quadrature formulas. [19]
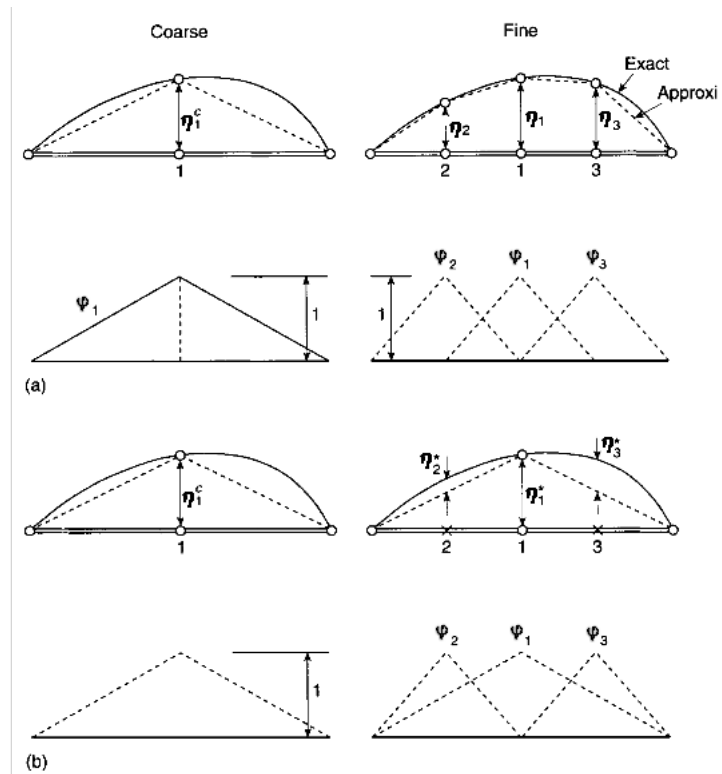
Figure 3.9: A one-dimensional problem of stretching of a uniform elastic bar by prescribed body forces. (a) Standard approximation. (b) Hierarchic approximation. [20]

33

4

XFEM

Fracture mechanics is one of the fields where FEM has been applied. Extensively one of the biggest drawbacks in FEM is that discontinuities have to follow the elemental boundaries. Especially when modeling crack growth ordinary FEM is very limited. For every time step (crack length increment) the model has to be in general terms for example remeshed, in order to handle the altered geometry. Hence, to combat this "flaw" the classical finite element approximation can be enriched, so that the singularities and discontinuous fields around the crack can be treated with greater precision. [6] is used as a general reference in this chapter.

4.1   Enrichment

Enrichment can be done by simply including information from the analytical solution of the problem into the approximation. The choice of enriched functions depends on the a priori solution of the problem. In analysis of cracks, analytical near crack tip solutions can be included into the approximation, in order to increases the accuracy of the solution. The enriching can be done in two ways: intrinsic and extrinsic enrichment. They are done either by enriching the basis functions or by enriching the approximation respectively.

4.1.1   Intrinsic enrichment

In this method new terms (shape functions) are included into the basic basis function

$$p = \{p^{bas}, p^{enr}\}, \tag{4.1}$$

in order to satisfy some condition of reproducing a complex field.

In analysis of cracks new terms are included into the basis function, ϕ. For example, the near crack tip two dimensional displacement field can be written as

$$u_{x_1} = \frac{1}{\mu}\sqrt{\frac{r}{2\pi}}(K_I\cos\frac{\theta}{2}(\kappa - \cos\theta) + K_{II}\sin\frac{\theta}{2}(\kappa + \cos\theta + 2)), \tag{4.2a}$$

$$u_{x_2} = \frac{1}{\mu}\sqrt{\frac{r}{2\pi}}(K_I\sin\frac{\theta}{2}(\kappa - \cos\theta) + K_{II}\cos\frac{\theta}{2}(\kappa + \cos\theta + 2)), \tag{4.2b}$$

34

where μ is shear modulus, κ is a material parameter r and θ are polar coordinates originating at the crack tip (figure 4.1). It is possible to show the displacement field
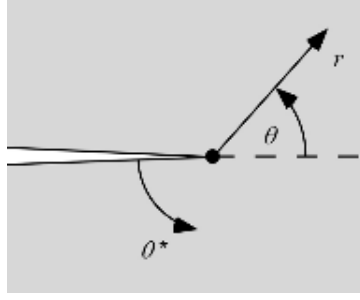
Figure 4.1: Polar coordinates at the crack tip. [8]

(equation 4.2) near crack tip can be expressed by following basis function p

$$p^T(\mathbf{N}) = [\sqrt{r}\sin\frac{\theta}{2}, \sqrt{r}\cos\frac{\theta}{2}, \sqrt{r}\sin\theta\sin\frac{\theta}{2}, \sqrt{r}\sin\theta\cos\frac{\theta}{2}]. \quad (4.3)$$

For the complete solution the basic basis function must be included into the total basis function. For example, if the basic approximation is linear the basis function would be

$$p^T(\mathbf{N}) = [1, x_1, x_2, \sqrt{r}\sin\frac{\theta}{2}, \sqrt{r}\cos\frac{\theta}{2}, \sqrt{r}\sin\theta\sin\frac{\theta}{2}, \sqrt{r}\sin\theta\cos\frac{\theta}{2}], \quad (4.4)$$

where $\mathbf{x}$ is vector of the coordinates. Basis function 4.4 has been used by [22] for fracture analysis with the meshless element-free Galerkin (EFG) method

$$u^h(\mathbf{N}) = p^T(\mathbf{x})\eta(\mathbf{x}), \quad (4.5)$$

where $\eta(\mathbf{x})$ is a vector of coefficients obtained from the one of the least squares techniques for minimizing the overall error of approximation.

4.1.2 Extrinsic enrichment

The other type of enriching uses extrinsic base p^E in order to increase the order of completeness:

$$u^h(\mathbf{N}) = \sum_{j=1}^{M} \phi_j(\mathbf{N})(\eta_j + \sum_{k=1}^{N} p_k^e(\mathbf{N})\eta_k^e), \quad \eta_l = u(N_l), \quad (4.6)$$

where η_k^e are the additional unknowns or degrees of freedom associated to the enriched solution. In general partition of unity enrichment, equation 4.6 is

$$u^h(\mathbf{N}) = \sum_{j=1}^{M} \phi_j(\mathbf{N})(\eta_j + \sum_{k=1}^{N} f_k^{pu}(\mathbf{N})p_k^e(\mathbf{N})\eta_k^e), \quad \eta_l = u(N_l), \quad (4.7)$$

where $f_k^{pu}(\mathbf{x})$ are set of the partition of unity functions defined over the support domain of partition of unity enrichment Ω_{pu}, as illustrated in 4.2
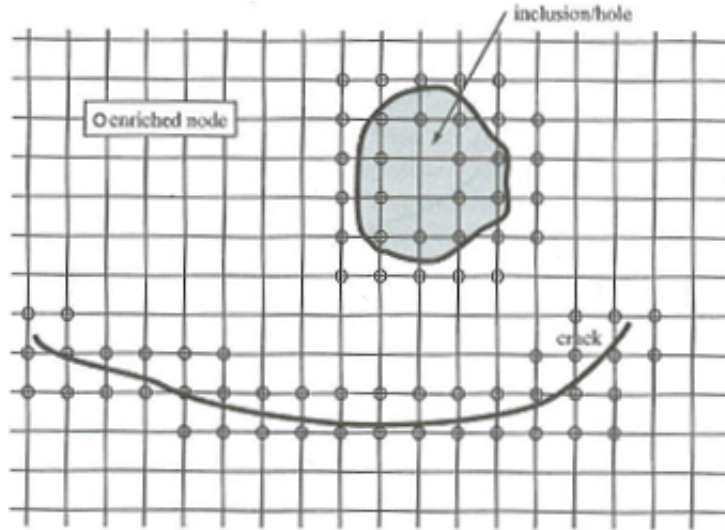
Figure 4.2: Support domain Ω_{pu}. [6]

4.1.3 Partition of unity finite element method

Melenk and Babuska [23] presented mathematical foundation for similar methodology (as extrinsic enrichment), called partition of unity finite element method (PUFEM). They used classical shape functions $\phi_j(\mathbf{X})$ for general point $\mathbf{x}$ within finite element,

$$u^h(\mathbf{N}) = \sum_{j=1}^{n} \phi_j(\mathbf{N})(\eta_j + \sum_{k=1}^{m} p_k^e(\mathbf{N})\eta_{jk}^e). \tag{4.8}$$

The approximation 4.8 is clearly a partition of unity and a compatible solution exists. Examining equation 4.8 for a typical enriched node N_j leads to:

$$u^h(\mathbf{N}_i) = \sum_{j=1}^{n} \phi_j(\mathbf{N}_i)(\eta_j + \sum_{k=1}^{m} p_k^e(\mathbf{N}_i)\eta_{jk}^e), \tag{4.9}$$

where the first part vanishes, expect for $\phi_i(\mathbf{N}_i)\eta_i = \eta_i$. Therefore,

$$u^h(\mathbf{N}_i) = \eta_i + \sum_{k=1}^{m} p_k^e(\mathbf{N}_i)\eta_{jk}^e, \tag{4.10}$$

which is not an acceptable solution. To satisfy interpolation at nodal points equation 4.8 is altered to

$$u^h(\mathbf{N}) = \sum_{j=1}^{n} \phi_j(\mathbf{N})(\eta_j + \sum_{k=1}^{m} (p_k^e(\mathbf{N} - p_k^e(\mathbf{N}_j))\eta_{jk}^e), \tag{4.11}$$

which guarantees $u^h(\mathbf{N}_i) = u_i$.

4.1.4 Generalized finite element method

Generalized finite element method (GFEM) differs from PUFEM in that different shape functions are used in classical and enriched part of the approximation. From equation 4.8

$$u^h(\mathbf{N}) = \sum_{j=1}^{n} \phi_j(\mathbf{N}_j)\eta_j + \sum_{j=1}^{n} \phi_j(\mathbf{N}_j)(\sum_{k=1}^{m} p_k^e(\mathbf{N})\eta_{jk}^e). \tag{4.12}$$

The generalized form is written

$$u^h(\mathbf{N}) = \sum_{j=1}^{n} \phi_j(\mathbf{N}_j)\eta_j + \sum_{j=1}^{n} \phi_j^e(\mathbf{N}_j)(\sum_{k=1}^{m} p_k^e(\mathbf{N})\eta_{jk}^e), \tag{4.13}$$

where ϕ_j^e are new shape functions associated with the enriched part of the approximation.

4.1.5 Extended Finite Method

in Extended Finite Element Method (XFEM) the enrichment is done in a local level, in contrast to PUFEM and GFEM, where the enrichment is usually done in a global level. The assumption of equation 4.13 generates a compatible solution even if partition of unity is used on a local level. This generates considerable computational advantages, since only nodes close to crack are enriched. Enriching only nodes that are close the crack tip can create solution compatibility and interior discontinuities in displacement or strain field approximations. The reason for this is the different order of approximation in adjacent elements while each element follows different basis function. This results in, different values for the common nodes (an internal discontinuity).

4.1.6 Blending Zone

Discontinuities in solution approximation fields can be handled by placing a blending zone around the enriched crack tip elements. In blending zone a ramp function is inserted into the domain that connects elements with and without enrichment (figure 4.3):

$$u^h(\mathbf{N}) = (1 - R)u^{classical}(\mathbf{N}) + Ru^{enriched}(\mathbf{N}), \tag{4.14}$$

where R is a blending ramp

$$R = \begin{cases} 1 & \in \Gamma^e \\ 0 & \in \Gamma^c \end{cases} \tag{4.15}$$

where Γ^e and Γ^c are enriched and classical boundary respectively. Discontinuity can occur in both intrinsic and extrinsic enrichments.

Ramp function can be of any order; a linear R guarantees the continuity of the unknown (e.g. displacement field) and a quadratic R gives smooth approximation of the first derivative of the unknown (e.g. strain field) etc. Hence, finite elements used for the whole domain fall into three categories: classical elements, enriched elements, and partially enriched elements (figure 4.4).
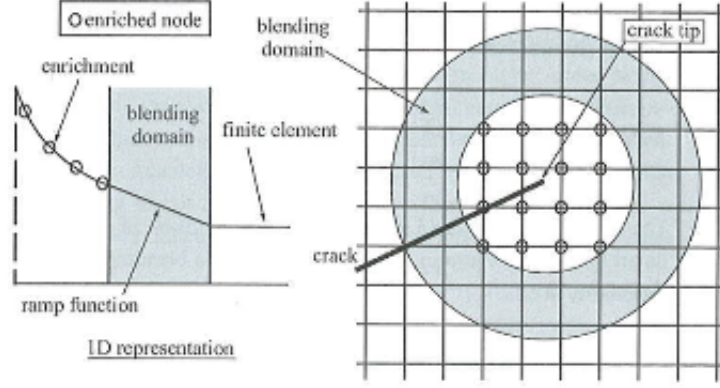
Figure 4.3: Transition between enriched and standard approximations. [6]
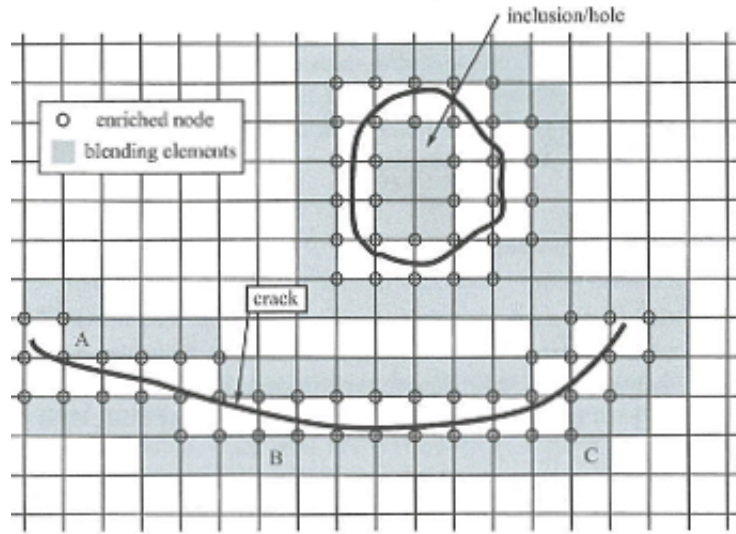
Figure 4.4: Standard, enriched and blending elements. [6]

Figure 4.4 shows the distribution of the three linear element types: classical elements governed by FEM, blank squares; enriched elements governed by XFEM, blank squares with circles in the corners; and blending elements partially governed by XFEM, gray elements. Blending elements are, in addition, dived into three types: type A has three enriched and one classical nodes, type B has two enriched and two classical nodes, and type C that has only one enriched node.

The displacement field for a blending element can be expressed as a sum of classical approximation (for all nodes) and enriched approximation (for two nodes adjacent of a fully enriched element)

$$u^h(\mathbf{N}) = \sum_{j=1}^{4} \phi_j(\mathbf{N})\eta_j + \sum_{k=1}^{2} \phi_k(\mathbf{N})\Psi(\mathbf{N})\eta_k^e, \tag{4.16}$$

38

where $\Psi(\mathbf{N})$ is enrichment function. The fact that the second part of equation 4.16 is not a partition of unity has little effect on the approximation, since blending element does not contain a singularity.

4.2 XFEM for Isotropic Problems

The XFEM approximation is constructed by producing a normal FEM mesh and adding some degrees of freedom to selected nodes close to the discontinuities to achieve better approximation, in order to have better accuracy.

4.2.1 Basic XFEM Approximation

The following XFEM approximation was used to calculate displacement for node N in [24]

$$u^h(\mathbf{N}) = u^{FE}(\mathbf{N}) + u^{enr}(\mathbf{N}) = \sum_{j=1}^{n} \phi_j(\mathbf{N})\eta_j + \sum_{k=1}^{m} \phi_k(\mathbf{N})\Psi(\mathbf{N})\eta_k^e, \qquad (4.17)$$

where η_j is the vector of regular degrees of freedom in FEM, η_k^e is the additional set of degrees of freedom and $\Psi(\mathbf{N})$ is the discontinuous enrichment defined for the nodes that are in the influence domain of the discontinuity. The first term in equation 4.17 is the classical finite element approximation and the second term is the enrichment approximation that describes the discontinuity.

The influence domain of a node, illustrated in figure 4.5, consists of the elements that contain that particular node. The analytical solutions of the type of discontinuity
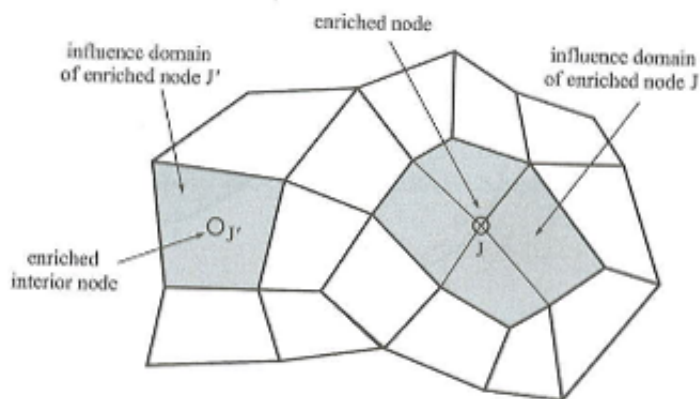
Figure 4.5: Unfluence domains od an edge node J and an internal node J. [6]

can be the basis for the enrichment function $\Psi(\mathbf{N})$ that is chosen. The main function of different enrichment functions in XFEM is to add following features: depict the singular field around the crack tip, continuous displacement in adjacent elements,

independent strain fields in opposite sides of the discontinuity, and maybe some other features according the type of discontinuity problem.

An arbitrary number, np, of discontinuities can be taken into account with XFEM by modifying the approximation 4.17

$$u^h(\mathbf{N}) = u^{FE}(\mathbf{N}) + u^{enr}(\mathbf{N}) = \sum_{j=1}^{n} \phi_j(\mathbf{N})\eta_j + \sum_{l=1}^{np}\sum_{k=1}^{m} \phi_k(\mathbf{N})\Psi_l(\mathbf{N})\eta_{k,l}^e. \qquad (4.18)$$

4.2.2 Signed Distance Function

Signed distance function is one of the tools needed in forming XFEM approximation of a problem as seen later. The distance d from a point x to an interface X is defined as

$$d = \|x - X_x\|, \qquad (4.19)$$

where $X - x$ is the normal projection of x on X. The signed distance function $\xi(x)$ is defined as

$$\xi_k(x) = \min_{x_X \in X} \underbrace{|x - x_X|}\,\text{sign}(n \cdot (x - x_X)), \qquad (4.20)$$

where n is the unit normal vector.

4.2.3 Strong Discontinuity

A strong discontinuity can be modeled several ways. One dimensional example of a XFEM enrichment is shown in figure 4.6 to illustrate different types of enrichment $\Psi(\mathbf{N})$ in equation 4.17. In figure 4.6 only nodes 2 and 3 requires enrichment, since
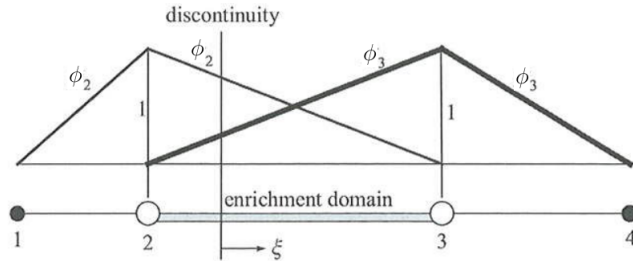
Figure 4.6: one dimensional crack problem: standard linear shape functions. [6]

nodes 1 and 4 are not affected by the discontinuity. The discontinuity is in an arbitrary location within the middle of the element. The simplest way is to approximate discontinuity with a jump function

$$\phi_i^h = \begin{cases} \phi_i - 1 & \phi \in \Omega_i \\ \phi_i & \phi \text{ not included in } \Omega_i \end{cases} \qquad (4.21)$$

where Ω_i is the domain between a discontinuity and the node i. A one dimensional representation of the jump function is illustrated in figure 4.7. A drawback in this

40
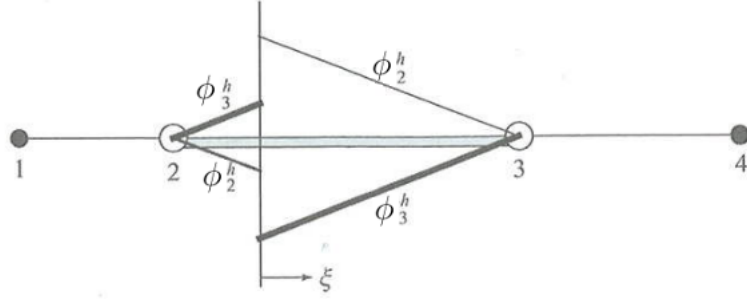
Figure 4.7: one dimensional crack problem: discontinuity described by a jump function. [6]

approach is the the approximation produces similar fields of the first derivative of the unknown for both sides of the discontinuity. This is not enough for crack simulations which requires independent strain fields.

The strong discontinuity can also be approximated by the Heaviside function H. Different definitions of H have been adopted. The first type of H is defined by a step function

$$H(\xi) = \begin{cases} 1 & \forall \, \xi > 0 \\ 0 & \forall \, \xi < 0 \end{cases} \tag{4.22}$$

Applying equation 4.22 to the approximation 4.17 gives

$$u^h(\mathbf{N}) = \sum_{j=1}^n \phi_j(\mathbf{N})\eta_j + \sum_{k=1}^m \phi_k(\mathbf{N})H(\xi)\eta_k^e, \tag{4.23}$$

figure 4.8a shows how this enrichment affects the shape functions. Approximation 4.23 must be altered to ensure it is an interpolation

$$u^h(\mathbf{N}) = \sum_{j=1}^n \phi_j(\mathbf{N})\eta_j + \sum_{k=1}^m \phi_k(\mathbf{N})(H(\xi) - H(\xi)_k)\eta_k^e, \tag{4.24}$$

which is illustrated in 4.8b. This type of an approximation may lead to a discontinuous field when applied on a quadrilateral element. Fields of the unknown and the derivative of the unknown remains independent on both sides of the discontinuity. In order to avoid numerical instabilities, a smoothed Heaviside function can be used. Some Smoothed Heaviside function are presented in [25]

An alternative type of a Heaviside function is the sign function

$$H(\xi) = \text{sign}(\xi) = \begin{cases} 1 & \forall \, \xi > 0 \\ -1 & \forall \, \xi < 0 \end{cases} \tag{4.25}$$

The way the sign function simulates the discontinuity is illustrated in figure 4.9a. Also in this case the approximation 4.17 needs to be modified by a simple shifting procedure to ensure the interpolation

$$u^h(\mathbf{N}) = \sum_{j=1}^n \phi_j(\mathbf{N})\eta_j + \sum_{k=1}^m \phi_k(\mathbf{N}(H(\xi) - H(\xi)_k)\eta_k^e, \tag{4.26}$$

presented in figure 4.9b.

41
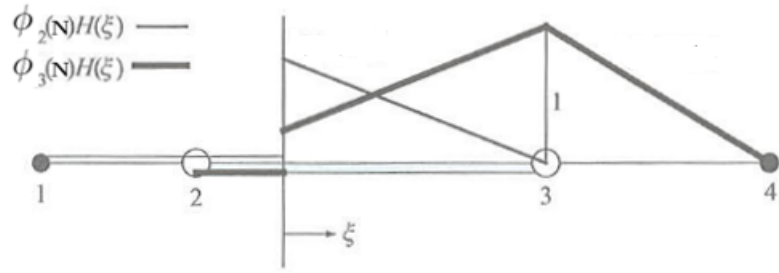
a) effect of the step function on shape functions
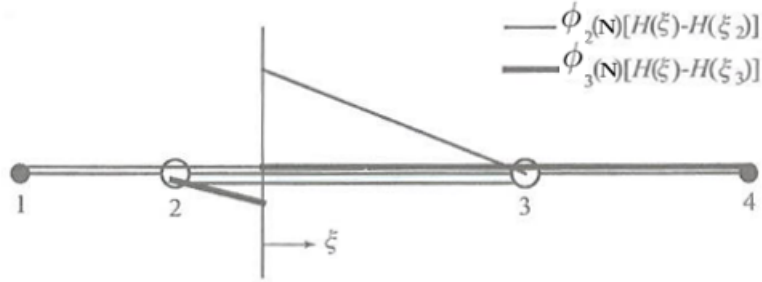
b) effect of shifting on shape functions

Figure 4.8: one dimensional crack problem: enriched shape functions and shifting Heaviside function. [6]

4.2.4 Weak Discontinuity

The same one dimensional problem, figure 4.6, as in section 4.2.3 is considered. The XFEM approximation 4.17 can now be defined by replacing the Heaviside function with an appropriate function $\Xi(\mathbf{N})$ [25]:

$$u^h(\mathbf{N}) = u^{FE}(\mathbf{N}) + u^{enr}(\mathbf{N}) = \sum_{j=1}^{n} \phi_j(\mathbf{N})\eta_j + \sum_{k=1}^{m} \phi_k(\mathbf{N})\Xi(x)\eta_k^e, \qquad (4.27)$$

where weak discontinuity function is defined in terms of the signed distance function ξ

$$\Xi_k(x) = |\xi(x)| - |\xi(x_k)|. \qquad (4.28)$$

Figure 4.10a illustrates these signed distance functions

Figure 4.10b shows the transformation of the original shape functions by the weak discontinuous enrichment functions. A kink in the unknown is introduced. Hence, a jump in its derivative is anticipated.

4.2.5 Plastic Enrichment

The concept of plastic enrichment that includes effects of crack tip plasticity is proposed in [26]. This model is based on a Ramberg-Osgood plasticity model discussed

a) effect of the sign function on shape functions

b) effect of shifting on shape functions
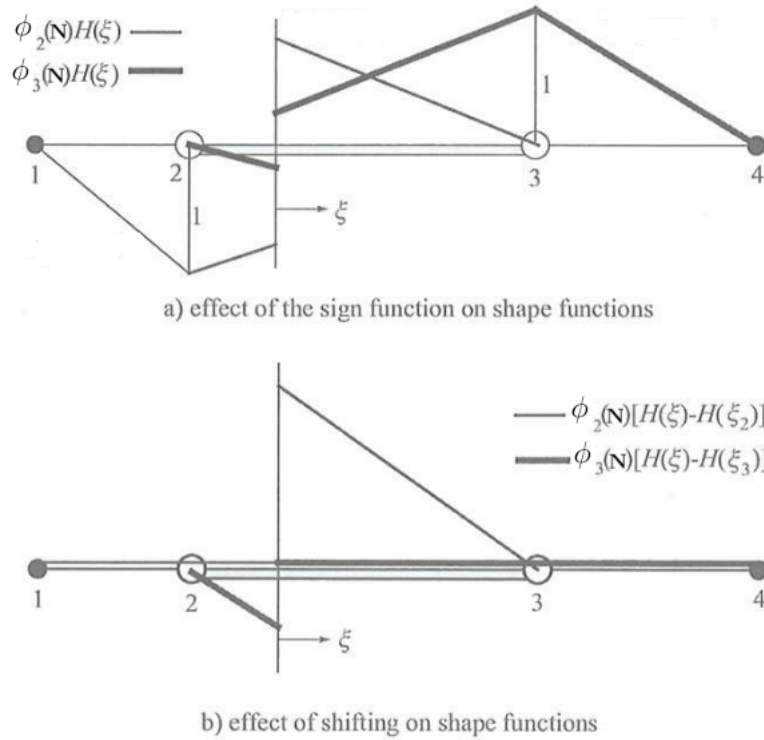
Figure 4.9: one dimensional crack problem: enriched shape functions and shifting Heaviside function. [6]

in section 2.2.1. The model gives for pure opening modes I and II the following basis function

$$r^{\frac{1}{n+1}}\{(\cos\frac{k\theta}{2}, \sin\frac{k\theta}{2}); k \in [1, 3, 5, 7]\}, \qquad (4.29)$$

where r and θ are defined in figure 4.1.

4.2.6 Selection of Nodes for Discontinuity Enrichment

Many different approaches for selecting the nodes that are enriched have been proposed along the years. For example, the Heaviside function enrichment can be separately applied to all the nodes that contain the crack tip by the following ways.

First, only nodes and edges that are crossed by the discontinuity are affected by enrichment while value of the modified shape function remains zero at all other nodes and edges, even if the crack tip is just on the edge, as illustrated in figure 4.11. This procedure satisfies the inter-element continuity requirements, but instabilities may occur when crack passes element edges.

Second, a classical jump function can be used to model the discontinuity. In this method all the nodes in an element containing the discontinuity are affected by the enrichment function as shown in figure 4.12 External forces affects the enrichment degrees of freedom.

43

a) enrichment functions

b) enriched shape functions
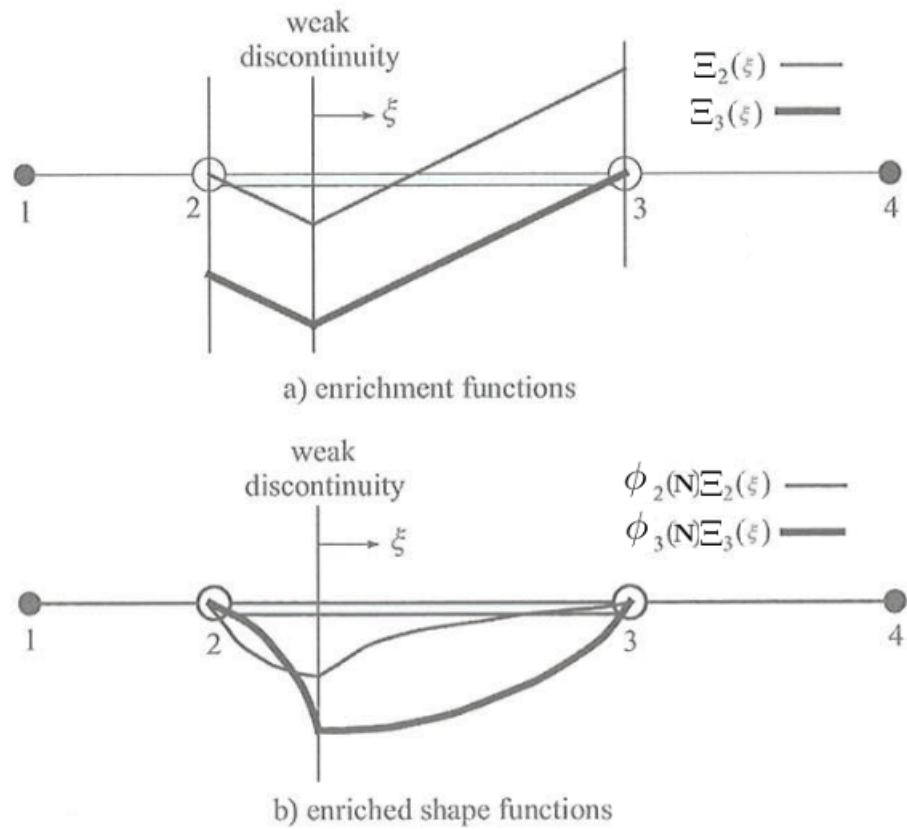
Figure 4.10: Weak discontinuous enrichment functions, and final enriched shape functions. [6]

a) crack tip inside element A

b) crack tip inside element B
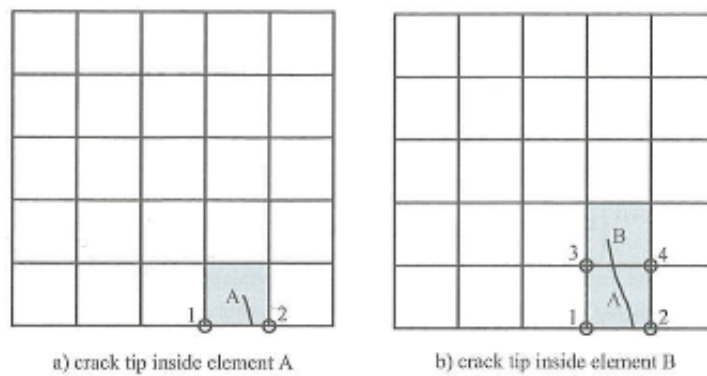
Figure 4.11: Enrichment nodes at different stages of crack propagation. [6]

Third, different enrichment functions can be applied to the elements that contains a crack tip and to the elements that are intersected by the discontinuity but do not contain its tip. This kind of a mesh is depicted in figure 4.13.

These kinds of procedures combined with blending zones ensure smooth field description for the unknowns.
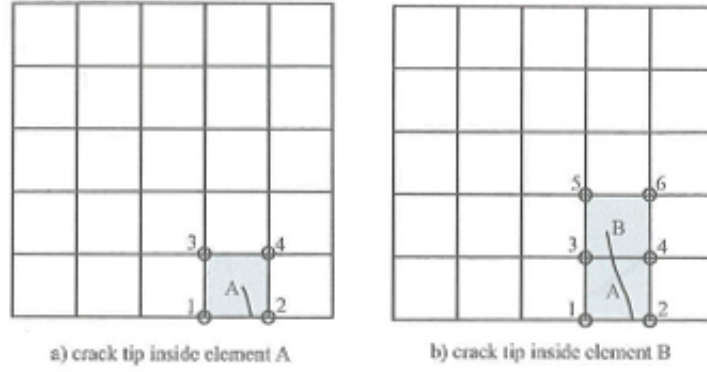
Figure 4.12: Enrichment nodes at different stages of crack propagation. [6]
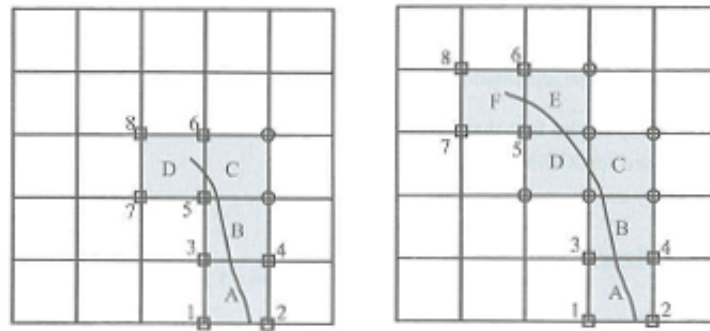
Figure 4.13: Node selection for enrichment at different stages of crack propagation; nodes marked by squares are enriched by crack tip functions and the circled nodes are enriched by the Heaviside function. [6]

4.2.7 Enrichment for Crack modeling

The following modification to approximation 4.17 is proposed in [27].

$$
\begin{aligned}
u^h(\mathbf{N}) &= \sum_{j=1}^{n} \phi_j(\mathbf{N})\eta_j + \sum_{h=1}^{m} \phi_k(\mathbf{N}) H(\xi(x))\eta_h^e \\
&+ \sum_{k=1}^{mt1} \phi_k(\mathbf{N}) \left(\sum_{l=1}^{mf} F_l^1(x)\Psi(\mathbf{N})\eta_k^{l1} \right) \\
&+ \sum_{k=1}^{mt2} \phi_k(\mathbf{N}) \left(\sum_{l=1}^{mf} F_l^2(x)\Psi(\mathbf{N})\eta_k^{l2} \right),
\end{aligned}
\tag{4.30}
$$

where m is the set of nodes in the support domain of the crack, but not the crack tip, while $mt1$ and $mt2$ are associated with crack tips 1 and 2, respectively. η_h^e, η_k^{l1} and η_k^{l2} are additional degrees of freedom for modeling crack faces and two crack tips, respectively, and F_l^1 and F_l^2 represent mf crack tip enrichment functions.

To include corrections related to interpolation term $H(\xi(x))$ is replaced with $H(\xi(x)) - H(\xi(x_h))$ and $F_l^i(x)$ with $F_l^i(x) - F_l^i(x_k)$, where $i = 1, 2$. The equation 4.30 is frequently used in XFEM analysis although it lacks the interpolation property.

4.3 XFEM discretization and quadrature

The procedure to build an extended finite element mesh follows the one presented in chapter 3 enhanced with the methods discussed in this chapter, beginning from the formulation of weak form the problem, followed by the discretization, and choosing appropriate quadrature etc. The enrichment functions complicate the procedure. The widely used Gauss quadrature, which is proven to be exact for polynomial integrands, in nonpolynomial cases may not be accurate.

Adding discontinuities to a mesh turns the displacement and stress fields into highly nonlinear fields and ordinary Gauss rules do not calculate them accurately. Two method to overcome this problem are introduce in [28].

First of the two methods is, where elements on both sides of the crack are subdivided into triangles, is illustrated in figure 4.14. Figure 4.15a shows the influence
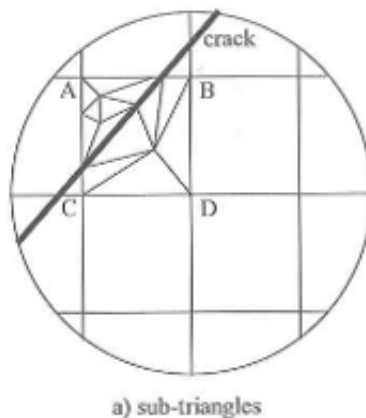
Figure 4.14: Sub-triangles in cracked element. [6]

domains of a node J above A^+ and belove the crack A^- which determines the nodes that are enriched. The node is enriched if values of $A^-/(A^+ + A^-)$ and $A^+/(A^+ + A^-)$ are smaller than an allowable tolerance. A tolerance value of 0.01% is used in [28], although the value must be set according to each problem. In second method the elements are subdivided into sub-quads otherwise the method are similar. In 4.15b the node J must not be enriched because there is no Gaussian point above the crack. In figure 4.15a the node J is enriched because each side of the crack in its influence domain includes at least one Gauss point.

The sub-triangulation process may not be accurate enough if Gauss points in sub-triangles are too close to the stress singularity, which is produced at the crack tip.
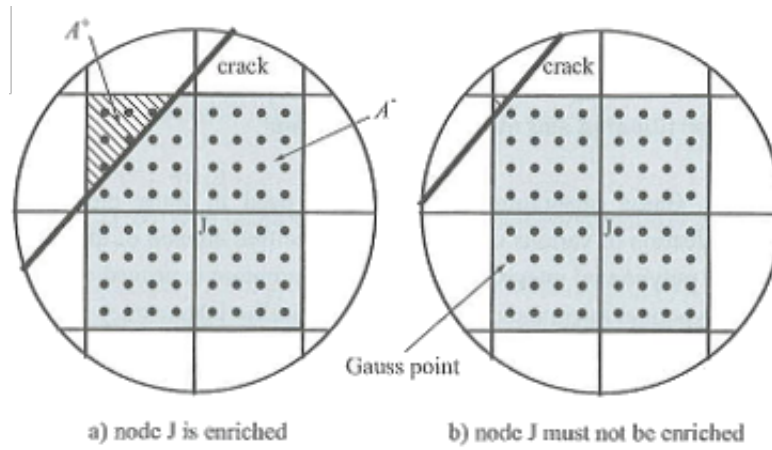
Figure 4.15: Criteria for node enrichment: a) based on definitions of A^+ and A^- in its support domain, b) based on the existence of Gauss points within its support domain. [6]

4.4 Level Set Method

The level set method (LSM), introduced in [29] is a capable tool to track boundaries. The method builds a surface from a curve. In two dimensional cases this cone shaped curve intersects the plane exactly where the curve sits. In other words, LSM generates a height (level) of a point in the plane as presented in figure 4.16.
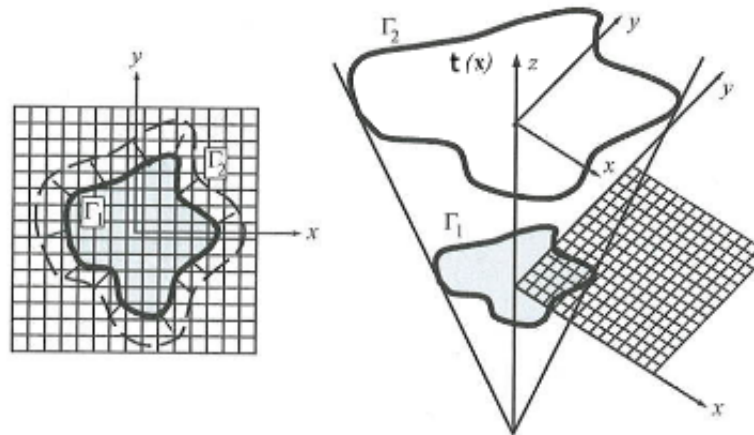
Figure 4.16: A simple description of LSM and FMM presented later, including the original front projected on the xy-plane and the level set function as the intersection of surface and xy-plane. [6]

In LSM the interface of interest is presented as a zero level set of a function $L(\mathbf{x})$, which is one dimension higher than the interface's dimension. This may cause larger needs for computational time and storage space.
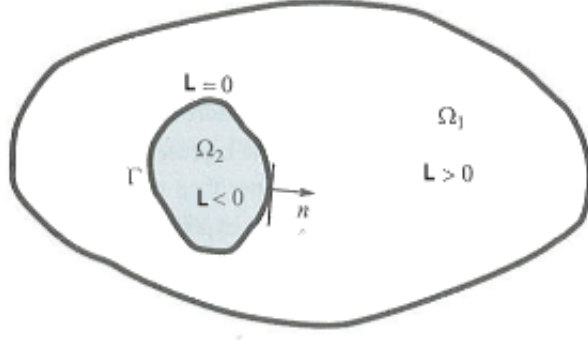
Figure 4.17: Definition of a level set function. [6]

The level set function $L(\mathbf{x})$, depicted in figure 4.17, is defined as

$$L(\mathbf{x}) = \xi(\mathbf{x}) = \begin{cases} > 0 & \mathbf{x} \in \Omega_1 \\ = 0 & \mathbf{x} \in \Gamma \\ < 0 & \mathbf{x} \in \Omega_2 \end{cases} \tag{4.31}$$

where Ω_1 and Ω_2 are non-overlapping subdomains of Ω sharing an interface Γ. In equation 4.31 the interface Γ can be interpreted as zero level contour of the level set $L(x)$. The level set can simply be defined as signed distance function

$$L(\mathbf{x}) = \begin{cases} d & \mathbf{x} \in \Omega_1 \\ -d & \mathbf{x} \in \Omega_2 \end{cases} \tag{4.32}$$

where d is the normal distance function from a point $\mathbf{x}$ to the interface Γ. The domains Ω_1 and Ω_2 can be defined with the Heaviside function of equation 4.22

$$\Omega_1 = \{\mathbf{x} \in \Omega, H(\phi(\mathbf{x})) = 1\}, \tag{4.33a}$$

$$\Omega_2 = \{\mathbf{x} \in \Omega, H(-\phi(\mathbf{x})) = 1\}. \tag{4.33b}$$

The normal vector $\mathbf{x}$ to the interface Γ at a point $\mathbf{x} \in \Gamma$ is defined as

$$\mathbf{n} = \frac{\nabla L(\mathbf{x})}{\|\nabla L(\mathbf{x})\|}. \tag{4.34}$$

Discretization of the levels set allows the evaluation of the level set at the element level, based on the nodal level set values $L_i = L(\phi_i)$ and known element shape functions $\phi_i(N_j)$

$$L(\mathbf{x}) = \sum_{i=1}^{n} \phi_i(\mathbf{x}) L_i, \tag{4.35}$$

where N_j are the nodes. The other advantage of this approximation is that it avoids the necessity for computation of derivatives of the level set functions at nodal points by expressing it in the terms of shape function derivatives.

$$L(\mathbf{x})_{,j} = \sum_{i=1}^{n} \phi_{i,j}(\mathbf{x}) L_i, \tag{4.36}$$

where $_{,j}$ is derivative along j direction.

4.4.1 Level sets for a crack

A major difficulty arises if the level set method is used in crack problems. The signed distance function is required to be constrained as the crack propagates, in order to keep the existing crack surface frozen. Since level set are usually updated by the integration of Hamilton-Jacobi equation, special techniques are needed so that the level sets describing existing crack remain unmodified [30]. Another reason for a new approach is the fact that level set functions are not updated with the speed of an interface in the direction normal to itself but with the speed of the crack fronts.

In [30] an approach based on the vector level set formulation is proposed, which avoids the level set update difficulty. In this method the level set is defined only on the narrow band around the crack and the evolution of the level set function does not alter the time history of the crack.

The definition of level sets needs to be adjusted in order to be used in open curves such as a crack. Generally two level sets are needed: one for the crack surface L^p and other for a crack tip L^s. A one dimensional crack propagation in a level set framework is modeled by representing the crack as the zero level set of function $L^p(\mathbf{x}, t)$. A crack tip is represented as the intersection of the zero level set of $L^p(\mathbf{x}, t)$ with zero level set of $L^{s,k}(\mathbf{x}, t)$, where ^{k} is the number of tips of a given crack. The crack tip level set is usually assumed to be orthogonal to the crack surface level set

$$L^p_{,i} L^s_{,i} = 0. \tag{4.37}$$

The values of the level set functions are stored only at the nodes. The functions can be interpolated over the mesh by shape functions [31]

$$L^{p,k}(\mathbf{x}, t) = \sum_{j=1}^{n} \phi_j(\mathbf{x})(L^{p,k}(\mathbf{x}, t))_j, \tag{4.38a}$$

$$L^s(\mathbf{x}, t) = \sum \phi_j(\mathbf{x}) L^s(\mathbf{x}, t). \tag{4.38b}$$

An important consideration is that although the actual crack is embedded inside a domain, the zero level set of L^s cuts through the entire domain. It is also assumed that once a part of a crack has formed, that part will no longer change shape or move.

Crack growth is modeled by appropriately updating the $L^{p,k}$ and L^s functions, then reconstructing the updated L function. The evolution of $L^{p,k}$ and L^s is determined by the crack propagation direction θ. In each, step the displacement of the crack tip is given by the prescribed velocity vector $\mathbf{v} = (\mathbf{v}_{x1}, \mathbf{v}_{x2})$, which is always normal to the interface. The following steps describe the simple procedure of evolution of the level set function $L^{p,k}_n$ and L^s_n at the step n [31]. In the first step the rotated level set of $L^{p,k}_n : L^{p,k,r}$ is determined. In step 2 L^s_{n+1} is determined. The updated location of the crack tip is computed in step 3. L^p_{n+1} is updated, if more than one crack tip exists, in step 4. The location of the new crack tip is determined by the intersection of zero level sets $L^{p,k}_{n+1}$ and L^s_{n+1}.

4.5 Fast Marching Method

The fast marching methods (FMM) ([32], [33] and [34]) are desingned to track a propagating interface and to find the first arrival of the interface as it passes a point. They are limited to problems where the speed function does not change sign.That speed can change from point to point, but there are no preferred directions.

FMM can also be transformed into a non-moving problem. In figure 4.18 the procedure is represented. $t(\mathbf{x})$ is the time when the front crosses the point $\mathbf{x}$. Function $t(\mathbf{x})$ gives a cone shaped surface that has the property to intersect xy-plane exactly where the curve was initially placed.
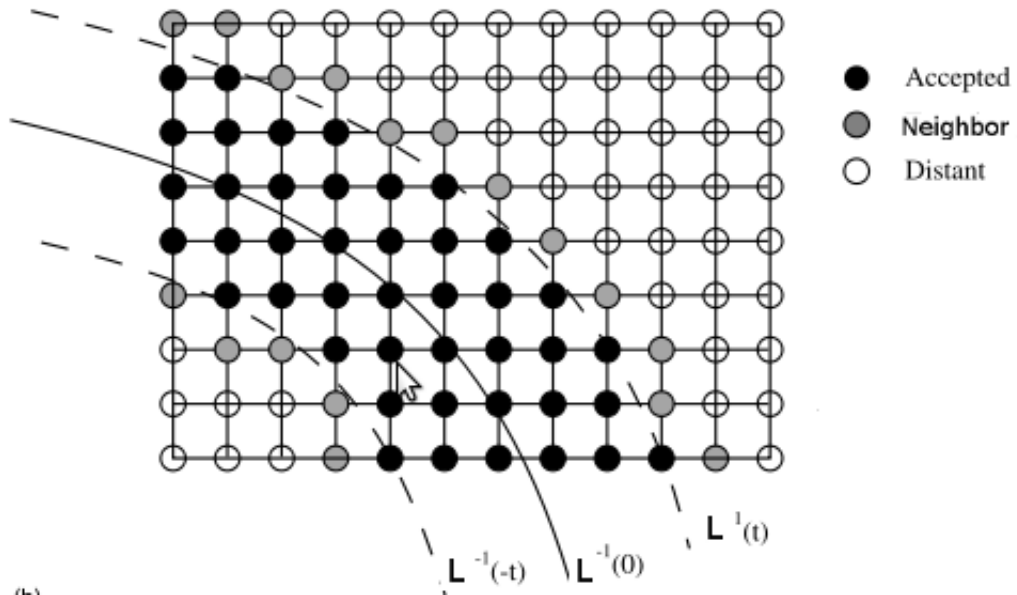
Figure 4.18: Classidication of nodes into accepted, neighbour and distant nodes. [35]

The starting point is placed in a set of accepted nodes. Mesh nodes which are one link away are considered as neighboring nodes. Then the cost of reaching each of these neighbor nodes is computed and the node with smallest cost is removed from the set of neighboring nodes and added the set of accepted nodes. The procedure continues by repeating the cost computing and additioning until all nodes are accepted. FMMs do not require any iterative procedure, which shortens the computing time.

5

Getfem

Getfem is a free open source C++ library for the finite element method as described in the quotation below:

> "The Getfem project focuses on the development of a generic and efficient C++ library for finite element methods elementary computations. The goal is to provide a library allowing the computation of any elementary matrix (even for mixed finite element methods) on the largest class of methods and elements, and for arbitrary dimension (i.e. not only 2D and 3D problems)."[36]

Project is still a work in progress: some functionalities are missing from the Matlab interface and also some methods for discontinuity handling are not yet fully finished. It is also, at the moment, restricted to two dimensional cases. Although much of its functionalities have been developed to the stage in which they can be used. In fact it has been used in several studies (e.g. [37], [38], and [39]).

Getfem's structure is presented in figure 5.1. Quadrature is cubature in Getfem's jargon. Getfem is based on a so called bricks framework, where every component in weak form of the problem is presented by a brick (e.g. if one dimensional problem consist of linear elastic specimen with a tied boundary and a force affecting other boundary, one simply adds one brick to describe the linear-elastic material response and two bricks to describe the boundary conditions and then solves the problem).

5.1   Structure of the code

Next a simple example of Getfem code is presented. The first step is to introduce a mesh, Getfem's own mesher can only produce simple meshes, more complex meshes can be imported from an external mesher. Simple Cartesian mesh is constructed with following command:

```
m = gfMesh('cartesian',[0:.1:1],[0:.1:1]);
```

which produces a square mesh with side lengths 1 and 10 nodes to each direction. Next step is to link the FEM to the mesh:

```
 mf = gfMeshFem(m,1);
```

S.T.L. and other standard libraries

GMM++
Linear algebra library and interface
to other specific libraries

MESH
Reference elements, geometric
transformations, nodes and mesh
description.

FEM
Finite element description at the
element level, degrees of freedom
description.

CUBATURE
Cubature description at the element
level.

MESHFEM
Finite element space description.
(finite element method on a whole
mesh)

INTEGELEM
Elementary integrals description

MESHIM
Integration method description on a
whole mesh.

LEVELSET
Description of level set functions on a,
mesh and finite element "cut" by some
level sets.

ASSEMBLE
Elementary matrix description and
assembly procedures.

BRICKS
Predefined bricks representing pde
models, boundary conditions and
specific constraints (incompressibility ...).

INTERFACES
Matlab and Python interfaces
Post−traitment facilities

Figure 5.1: Diagram of Getfem. [40]
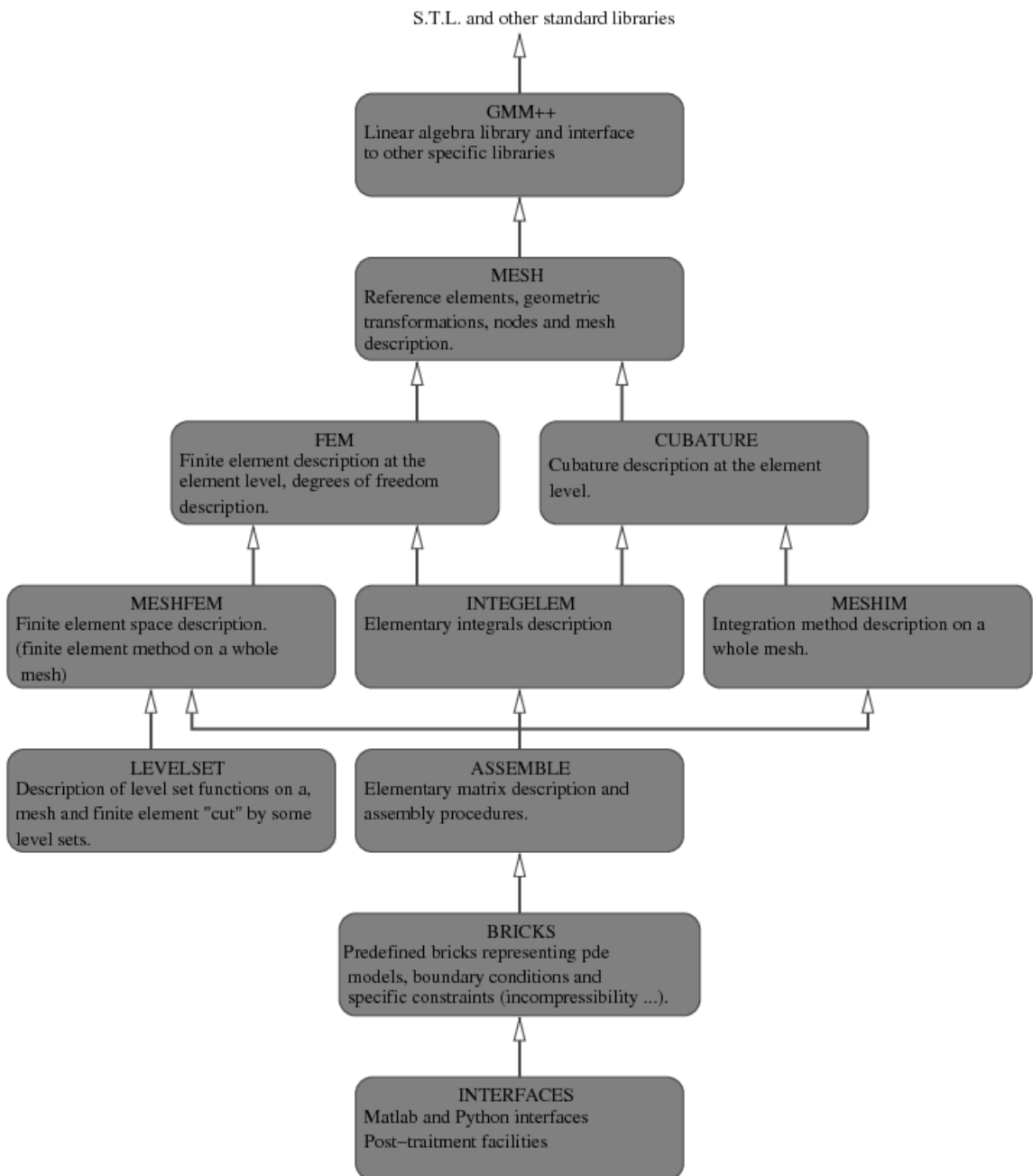
which builds a one dimensional FEM object to the mesh. Dimension of the FEM
object depends on the dimension of the unknown (1D for scalar fields, 2D for vectorial
fields, etc.). Several FEM objects can be introduced to a mesh, one for each unknown
or if the mesh has areas that differ from one another. Next the FEM type must be
specified:

```
set(mf,'fem',gfFem('FEM_QK(2,2)'));
```

this assigns the Q^2 FEM (2D element with quadratic shape functions) to every convex. Type of FEM must be in an agreement with mesh (Q FEM if the mesh contains square elements and P FEM if elements are triangular). In figure 5.2 two different element
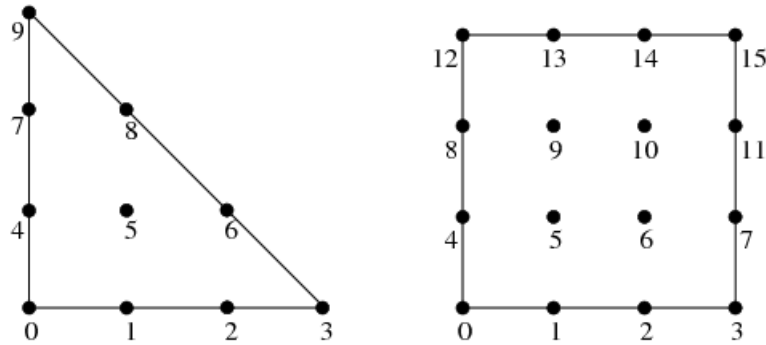
Figure 5.2: Two elements used by Getfem: left P_3^2 element and right Q_3^2 element. [36]

types that Getfem uses are presented.

Level sets are used to describe cracks and other discontinuities. In getfem, a levelset is one or two scalar functions, defined on a lagrange polynomial mesh_fem. The (optional) second function is a way to limit the level-set to handle cracks for example. Mesh level set object is created with following commands

```
ls=gfLevelSet(mesh, ls_degree,'with_secondary');
set(ls, 'values',function1,function2);
mls = gfMeshLevelSet(mesh);
set(mls,'add',ls);
set(mls,'adapt');
```

where the first command creates the level set object, and second command assigns functions that describes level set (function1 describes first level set etc.), third command prepares the mesh to have level sets by creating mesh level set object, fourth command assigns the level set to mesh level set object, and finally the last command adapts the mesh so that the level set cuts it. The modifications (that take discontinuities into account) to shape functions are made with the following commands:

```
ck0 = gf_global_function('crack',0);
coff = gf_global_function('cutoff',0,r,r1,r0);
ckoff0 = gf_global_function('product', ck0, coff);
```

where the first and second commands use modifications that are provided by the Getfem: "crack" has 11 different modifications which one can use depending on the case in hand. "cutoff" has four different options for cut off functions which can be used depending on the case: no cut off, exponential cut off and two different polynomial cut offs. Variables r, r1, and r0 are chosen for each problem ([37], [41]). r is the radius of the cut off function and r0 and r1 (r1 and r2 in [41]) are the limits of cut off function and they are chosen as follows $0 < r0 < r1$. The last command binds

the crack and the cut off modification together. To actually insert the modification
to the FEM one has to use following commands:

```
mfls    = gfMeshFem('levelset',mls,mf);
mf_sing = gfMeshFem('global function',mesh,ls, {ckoff0},1);
mf_u    = gfMeshFem('sum',mf_sing,mfls);
set(mf_u,'qdim',2);
```

where mesh level sets are added to the FEM, and modification to shape functions are
added to the FEM, the last command is the dimension of the FEM. In order to solve
the problem a numerical integration method is needed:

```
mim=gf_mesh_im(m, gf_integ('IM_QUAD(5)'));
```

IM_QUAD(5) quadrature has 7 integration points (figure 5.3). For meshes with level
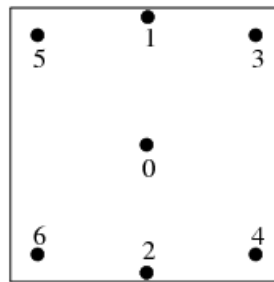
Figure 5.3: Integration points in "IM_QUAD(5)" quadrature. [36]

sets a bit different command is needed:

```
mim = gfMeshIm('levelset', mls, 'all', ...
        gfInteg('IM_STRUCTURED_COMPOSITE(IM_QUAD(7),3)'), ...
        gfInteg('IM_STRUCTURED_COMPOSITE(IM_GAUSS_PARALLELEPIPED(2,2),9)'), ...
        gfInteg('IM_STRUCTURED_COMPOSITE(IM_QUAD(7),6)'));
```

where composite integration methods are used. Second number in the integration
method is the number of subdivisions that the element is divided to. The command
consists of three different integration methods: one for crack tip, one for the other
part of the crack, and one for the rest of the material.

After these steps the actual model can be created:

```
md = gfModel('real');
set(md,'add_fem_variable', 'u', mf_u);
set(md,'add_initialized_data','lambda', "Lame coefficient");
set(md,'add_initialized_data','mu', "Lame coefficient");
set(md, 'add multiplier', 'lower_boudary', mf_u, 'u');
set(md, 'add Dirichlet condition with multipliers', mim, 'u', ...
'lower_boudary', "boundary for which the condition is set");
set(md, 'add initialized data', 'F', "magnitude of the loading");
set(md, 'add source term brick', mim, 'u', 'F', ...
"boundary for which the condition is set");
```

and then the model can be solved and plotted:

```
get(md,'solve','very_noisy');
U = get(md,'variable','u');
gf_plot(mf_u, U, 'norm', 'on');
```

5.2   advantages of Getfem

Getfem is relatively simple to use and it can be adapted to several different problems. It is capable handling all kinds of partial differential problems (elliptic, parabolic, and hyperbolic) and new material models are relatively simple to build into the library, i.e. the user can write new bricks to be used in calculations. Also different solvers are available or one can use one's own or a third party solver.

The mesher in Getfem can only cope very simple geometries, fortunately third party meshers are supported. The biggest drawback in Getfem is the lack of documentation: only a part of its functionalities are covered in the user manuals at present day. Also the Matlab interface is still not finished and some of the XFEM functionalities are not included yet.

6

XFEM code

The studied specimen is fixed at the lower boundary (Dirichlet condition) and the loading is set to the upper boundary. The specimen has an edge crack at {x,y} = {-0.5,0}. The initial crack is along the x-axis. Length of the initial crack is a and the width (and height) of the specimen, W. W is set to be 1 m in this work. In case one the crack length, a, is 0.3 W and in cases two and three the initial crack length, a, is 0.1 W. Specimen is discretized in 59 elements in each direction (total of 3481 elements) in all but one case. In case one a second problem with a mesh having 225 elements in each direction is utilized (totaling 50625 elements). A linear elastic material model is used and the material properties are: Young's modulus 200 X 10^9 Pa and Poisson ratio 0.3. The specimen is presented in figure 6.1. Boundary condition in the upper boundary varies in case two: one variation as in figure 6.1, in second the force, F, is in 45° angle relative to upper boundary, and in third the force, F, is parallel to the upper boundary.
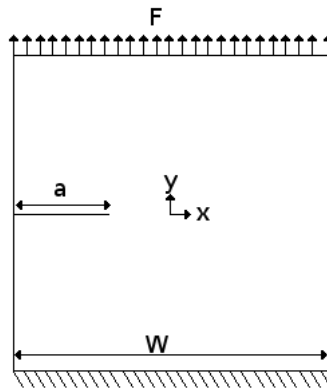
Figure 6.1: Position of the crack and boundary conditions.

The XFEM-solver calculates the two normal stress components in each direction and the shear stress from the darker elements in figures 6.2 and 6.3. The area is chosen such that the disturbances caused by mesh irregularities in close proximity of the crack tip are minimized. Stresses given by the solver are averages over the (darker) elements, this is also done to smoothen the possible irregularities. The effective distance (distance between crack tip and the area where stresses are computed,

r) is $3.125 * \frac{1}{K_{tot,x}}$, where $K_{tot,x}$ is the number of elements in vertical direction. 3.125 is amount of elements between the crack tip and the center location of the stress computing area. The place of the center point is calculated as a the weighted average of the element (inside the area) distances. The stresses used to calculate the crack propagation angle are computed in this area. The area is chosen such that the stress values are low enough (i.e. not at the infinite stress peak at crack tip) but still the effect of the crack tip is clearly visible.

Crack growth is implemented as follows: a straight line (black line, primary level set, in figure 6.2), the initial crack, is added. The crack is restricted with a half circle (black circle, secondary level set, in figures 6.2 and 6.3). Small circles in figure 6.3b are level set for used in define the precipitates in case 3. The angle of crack propagation for the next step is calculated with equation 2.43. Next the radius of second level set is increased by the crack growth increment and the line, the primary level set, is tilted from the end of the previous step. The following steps uses an identical this procedure. The line after the secondary level set is not included in the crack.

(a) 59 elements to each direction.

(b) 225 elements to each direction.
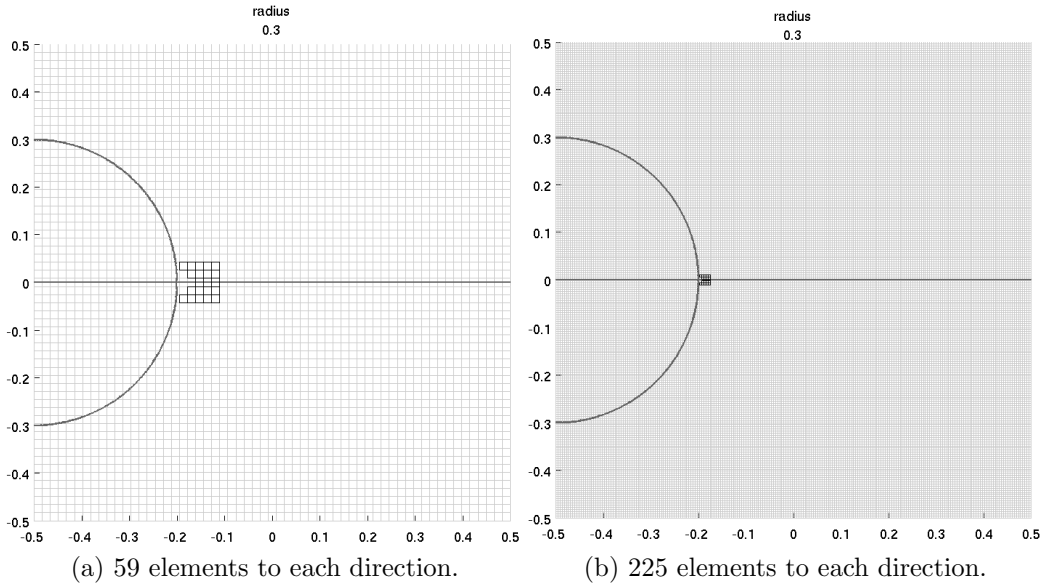
Figure 6.2: Level sets and the area from which stresses are computed in case 1.

The mesh is left somewhat coarse in purpose to hinder the computing time and memory requirements, as well as test the numerical abilities of the XFEM implementation. This results in some inaccuracies in the results, also the boundary conditions causes some error since they are tied into the nodes of the boundary. Subsequently, nodes are quite far apart of each other and thus the conditions are not enough continuous to give smooth displacement field on the specimen corners (figure 6.4). The center point of precipitates in figure 6.3b are at {-0.028,-0.059} and second at {-0.018,0.059}. Radius of the precipitates is $\frac{3.4}{100}$ of the whole specimen.

In figure 6.4 mode I loading with two different discretization is shown. Displacement field changes at {x,y} = {-0.2,0} this is due to the crack. The crack causes the upper boundary of the specimen to be "more free" in x = -0.5...-0.2 than after the

(a) Case2.   (b) Case3; Precipitates are presented by the
                              small circles.
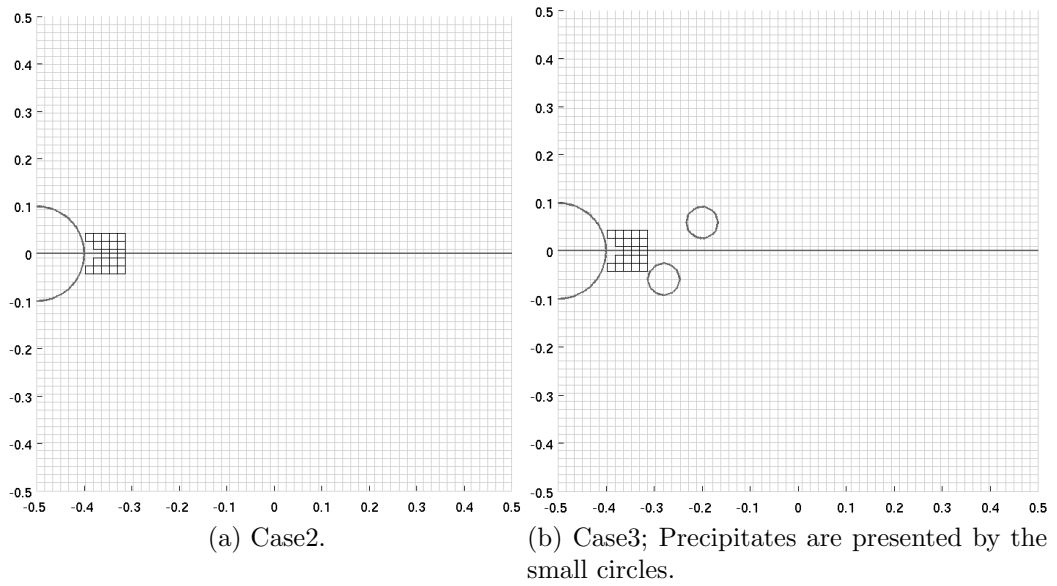
Figure 6.3: Level sets, initial crack, and the area from which stresses are computed in cases 2 and 3.

crack tip where it is fixed.

(a) 59 elements.   (b) 225 elements.
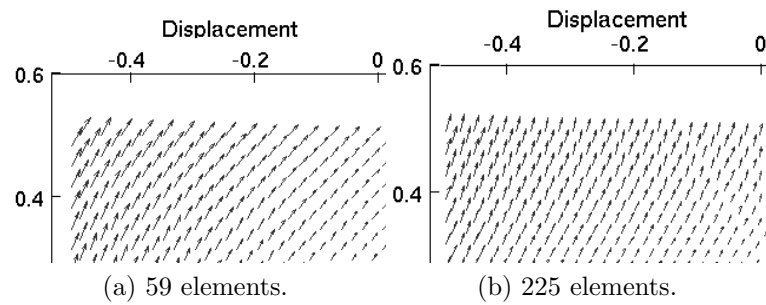
Figure 6.4: Displacement fields with two different discretization in the upper left corner of the specimen.

In each case 30 steps are taken. Initial crack length is $\frac{1}{10}$ of the whole specimen and crack increment on each step is $\frac{89}{10000}$ of the whole specimen so the final crack length is $\frac{367}{1000}$ of the whole specimen.

In case 1 two runs are made to compare different discretizations. In cases 2 and 3 non rectilinear crack propagation paths are analyzed. The area from which the stresses are computed moves along with the crack tip (figure 6.5).

(a) Step 1. (b) Step 15. (c) Step 30.
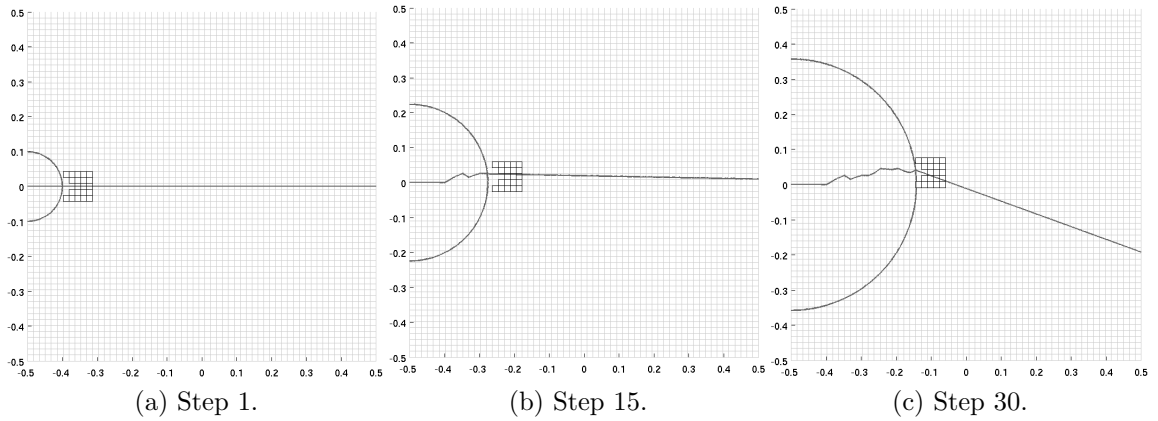
Figure 6.5: Movement of the area from which stresses are computed.

7

Results

Results of the three cases are presented in the following sections. In the first case the vertical stress component is plotted to verify that the code is working properly (i.e. the shape of the stress field is correct and the magnitude of the stress at the crack tip is in agreement with the theoretical estimates).

In the second case the crack path at steps 15 and 30, displacement and von Mises stress fields at the final step, and finally deformed mesh at step 30 are plotted. A table in which K_I/K_{II}-ratios and crack growth angles are collected is also presented.

Crack paths in steps 15 and 30, and deformed meshes at step 30 are plotted for the two further variants (with precipitates 3 times and 7 times stiffer than the base material) in case 3. Also in this case the K_I/K_{II}-ratios and crack growth angles are compiled into a table.

7.1 Case 1

This case deals with a stationary crack with initial length $\frac{3}{10}$ of the side of the whole specimen. Vertical stress components are plotted in figures 7.1 and 7.2. In figure 7.2 the colors and contrast of the picture are modified to enhance the stress field area. Crack mouth opening is 5×10^{-5} in both 59 X 59 and 225 X 225 elements cases, and computed K_I is 12.77 X 10^6 and 10.995 X 10^6 respective.

(a) 59 elements in each direction.　　　　(b) 225 elements in each direction.
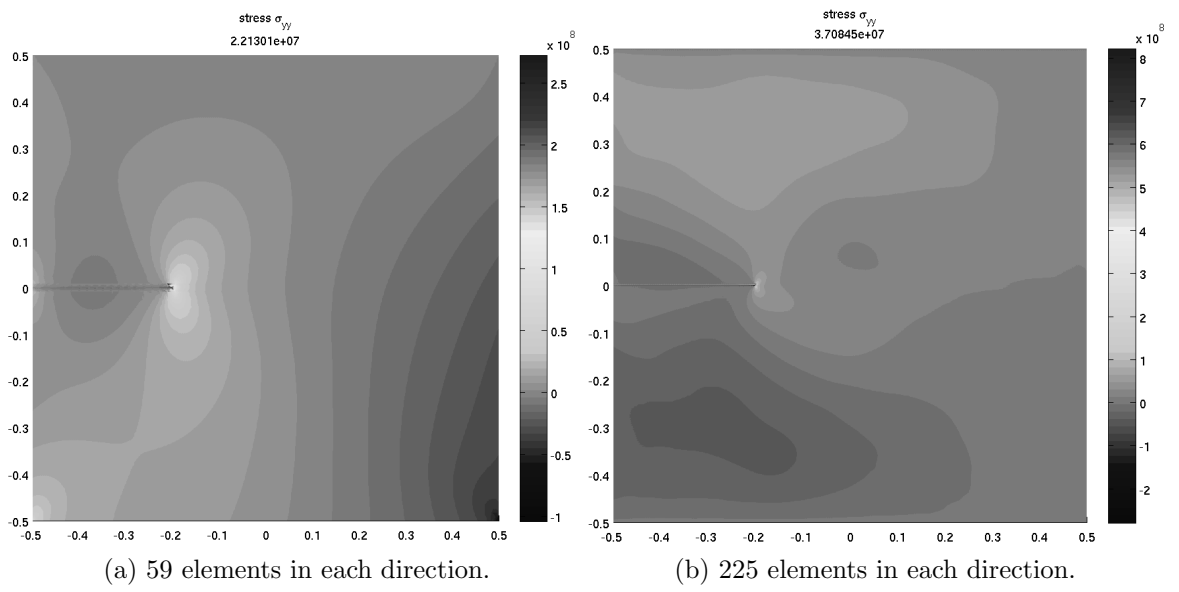
Figure 7.1: Vertical stress components.

(a) 59 elements in　(b) 225 elements in
each direction.　　each direction.

Figure 7.2: Shape of the vertical stress field around the crack tip.

7.2 Case 2

Three different variants in terms of crack growth calculation are presented in this section. First with a vertical force , second with a horizontal force, and third with a force tilted 45° relative to upper boundary. Initial crack length is $\frac{1}{10}$ of the whole specimen width in this case.

7.2.1 Vertical Force

(a) Step 15.   (b) Step 30.
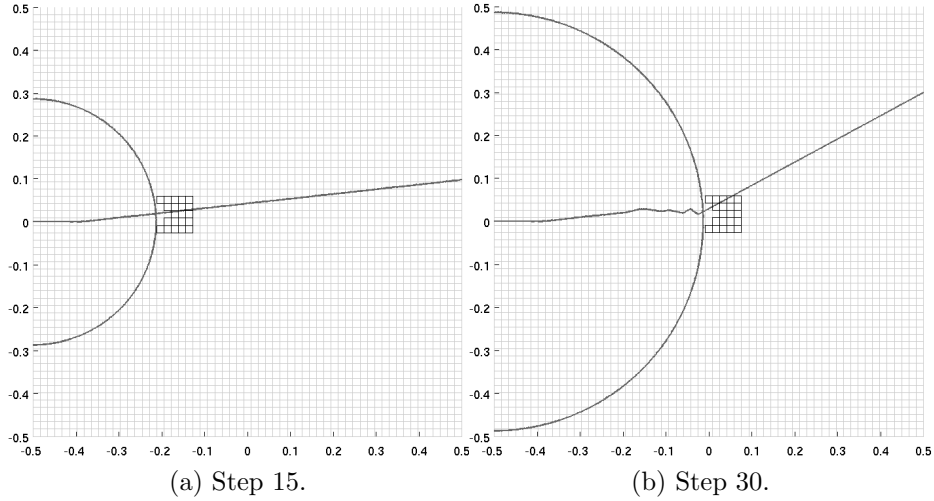
Figure 7.3: Crack path at steps 15 and 30.

Crack path in specimen with vertical force (upwards) is shown in figure 7.3. Stress and displacement vectors are plotted in figure 7.4 and deformed mesh is plotted in figure 7.5. Table 7.1 shows the crack growth $\frac{K_I}{K_{II}}$ ratio and the angles at each step.

Table 7.1: $\frac{K_I}{K_{II}}$ ratios and crack growth angles (degrees) at different steps.

Step	1	2	3	4	5	6	7	8	9	10
$\frac{K_I}{K_{II}}$ ratio	-38.9	-23.4	-21.8	-15.5	-16.5	-19.9	-14.3	-19.8	-17.6	-28.1
Angle	2.9	4.9	5.2	7.3	6.9	5.7	7.9	5.8	6.5	4.1
Step	11	12	13	14	15	16	17	18	19	20
$\frac{K_I}{K_{II}}$ ratio	-20.4	-17.5	-15.0	-18.1	-28.8	-14.0	-6.3	-9.6	45.7	29.4
Angle	5.6	6.5	7.6	6.3	4.0	8.1	17.1	11.7	-2.5	-3.9
Step	21	22	23	24	25	26	27	28	29	30
$\frac{K_I}{K_{II}}$ ratio	7.2	70.7	-10.0	74.3	2.5	-3.8	-3.4	1.4	-3.5	-7.6
Angle	-15.2	-1.6	11.2	-1.5	-35.5	26.6	28.8	-47.9	28.4	14.5

(a) displacement vectors. Crack mouth opening is 1.8×10^{-5}

(b) Von Mises stress.
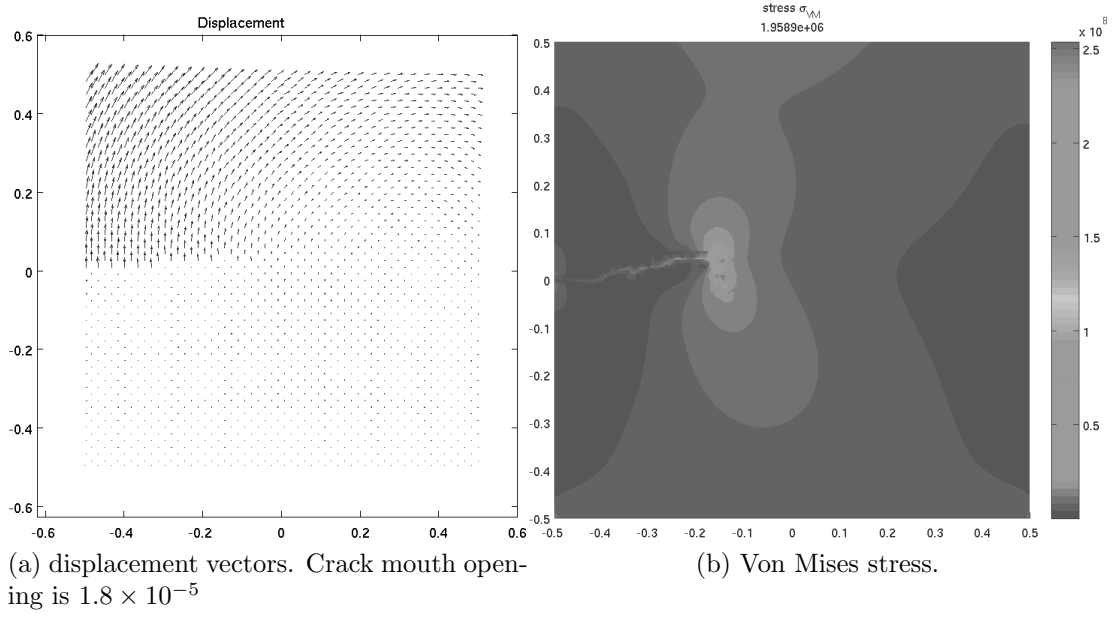
Figure 7.4: Stress and displacement vectors at step 30.
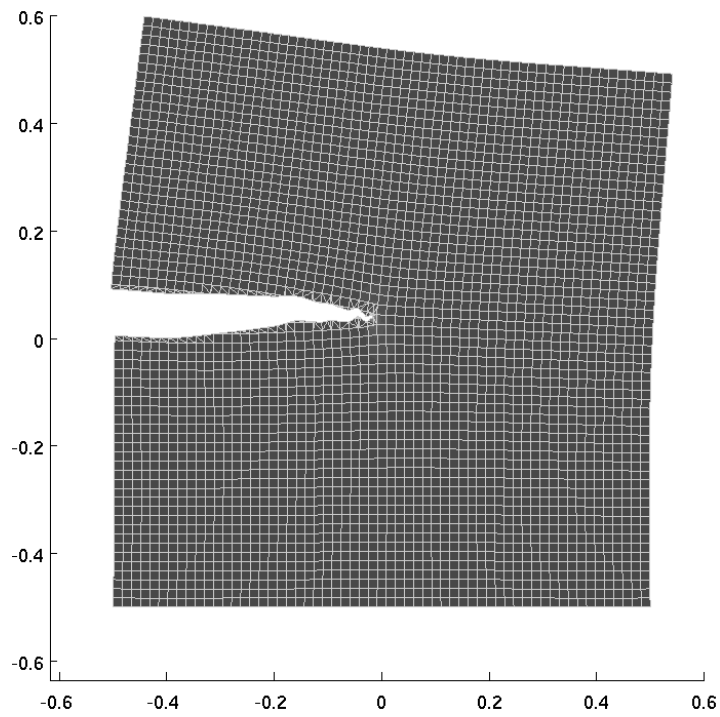
Figure 7.5: Mesh and deformation at step 30.

7.2.2 Horizontal Force

Crack path in specimen with horizontal force (to left) is shown in figure 7.6. In figure 7.7 stress and displacement vectors are plotted. Deformed mesh is plotted in figure 7.8. Table 7.2 shows the crack growth $\frac{K_I}{K_{II}}$ ratio and angles at each step.

(a) Step 15.

(b) Step 30.

Figure 7.6: Crack path at steps 15 and 30.

(a) displacement vectors. Crack mouth opening is 3.5×10^{-5}

(b) Von Mises stress.

Figure 7.7: Stress and displacement vectors at step 30.
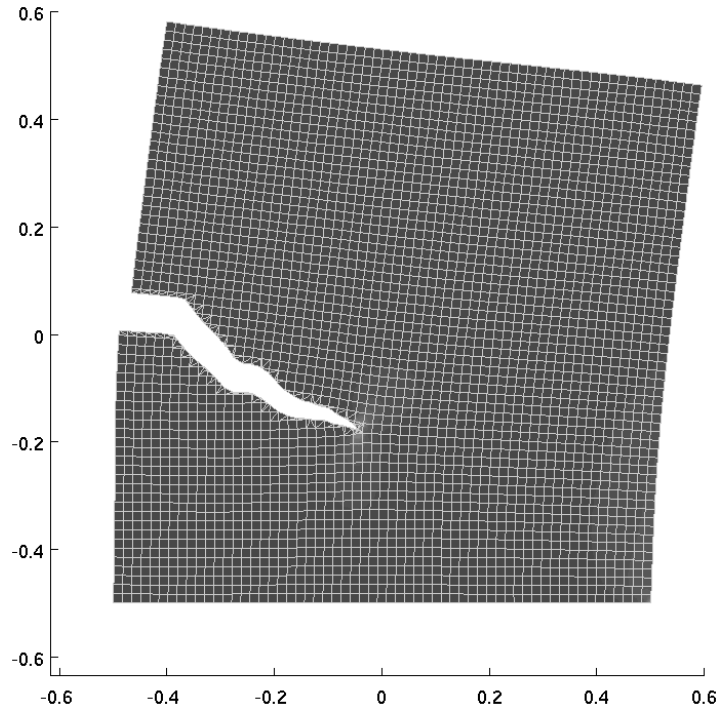
Figure 7.8: Mesh and deformation at step 30.

Table 7.2: $\frac{K_I}{K_{II}}$ ratios and crack growth angles (degrees) at different step.

Step	1	2	3	4	5	6	7	8	9	10
$\frac{K_I}{K_{II}}$ ratio	1.1	2.6	1.1	2.8	2.4	1.3	3.2	0.9	9.4	304.9
Angle	-51.19	-34.7	-51.6	-33.1	-35.9	-48.8	-30.2	-55.2	-11.9	-0.4
Step	11	12	13	14	15	16	17	18	19	20
$\frac{K_I}{K_{II}}$ ratio	31.8	8.5	2.7	2.0	2.2	2.3	11.5	5.0	204.8	5.9
Angle	-3.6	-13.1	-34.0	-40.1	-38.6	-37.2	-9.8	-21.2	-0.6	-18.2
Step	21	22	23	24	25	26	27	28	29	30
$\frac{K_I}{K_{II}}$ ratio	75.3	40.2	3.0	9.5	4.6	4.5	2.8	3.8	55.6	9.0
Angle	-1.5	-2.9	-31.2	-11.8	-22.6	-23.0	-33.1	-26.4	-2.1	-12.4

7.2.3 Tilted Force

Crack paths in specimen with tilted force (components to left and upwards) are shown in figure 7.9. In figure 7.10 stress and displacement vectors are plotted. Deformed mesh is plotted in figure 7.11. Table 7.3 shows the crack growth $\frac{K_I}{K_{II}}$ ratio and the angles at each step.

(a) Step 15. (b) Step 30.

Figure 7.9: Crack path at steps 15 and 30.

(a) displacement vectors. Crack mouth opening is 6×10^{-5}

(b) Von Mises stress.
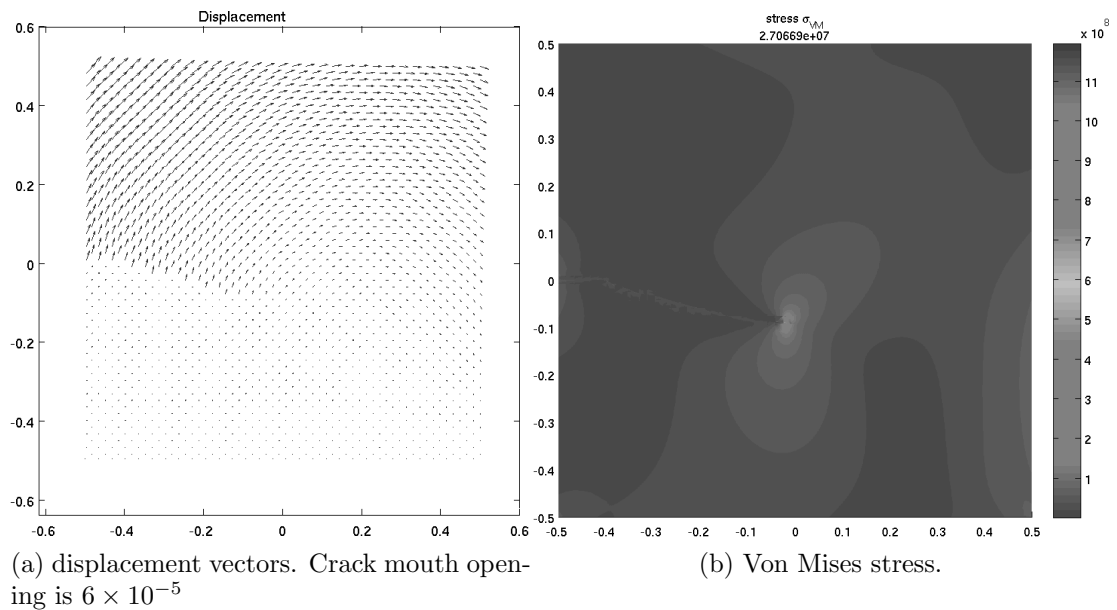
Figure 7.10: Stress and displacement vectors at step 30.
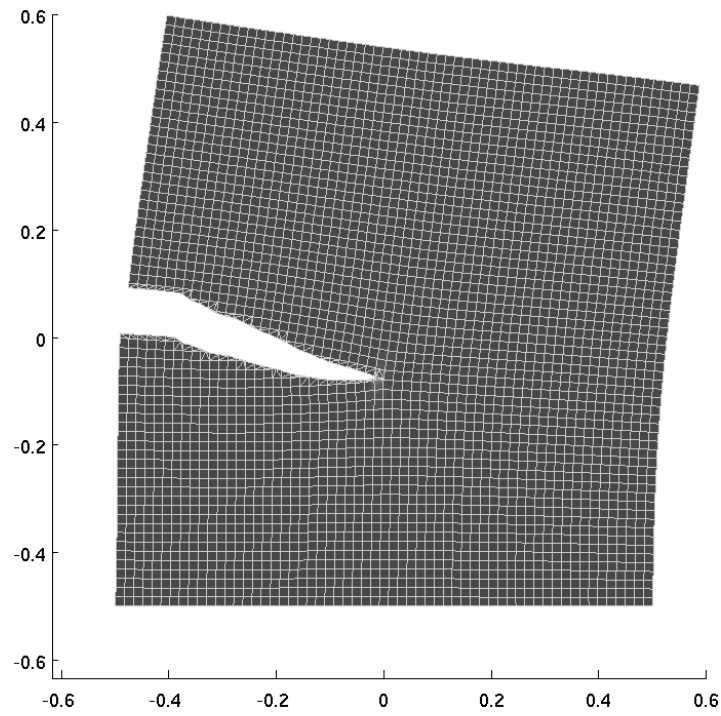
Figure 7.11: Mesh and deformation at step 30.

Table 7.3: $\frac{K_I}{K_{II}}$ ratios and crack growth angles (degrees) at different step.

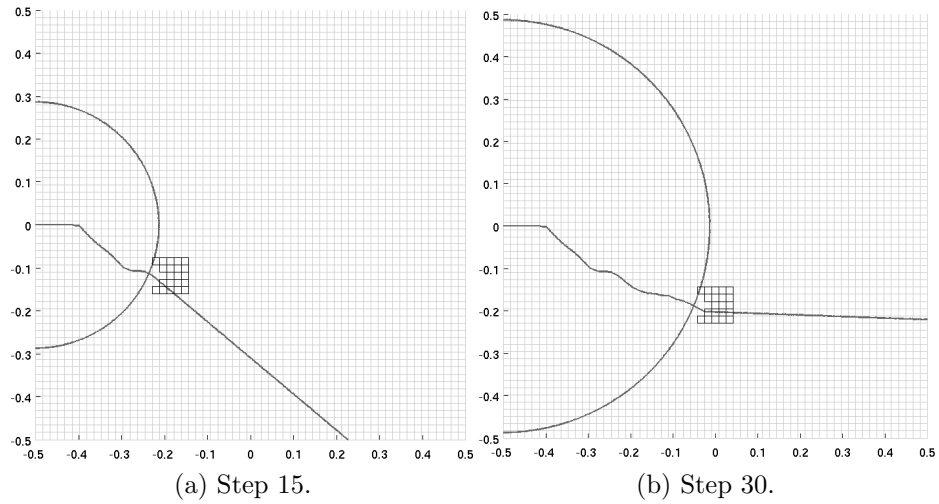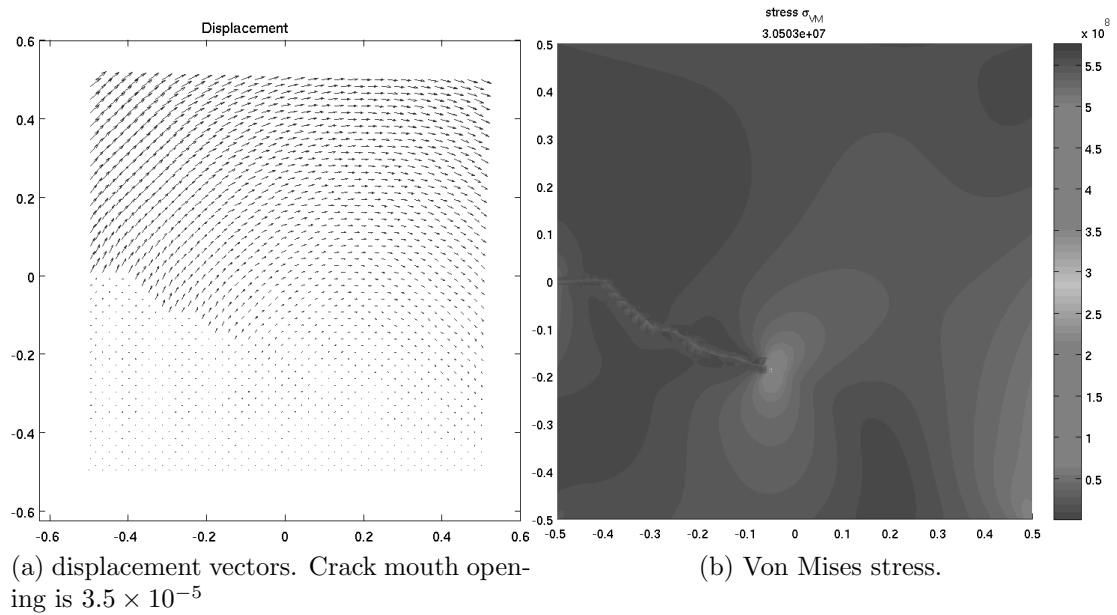| Step	1	2	3	4	5	6	7	8	9	10
$\frac{K_I}{K_{II}}$ ratio	2.7	4.4	31.5	4.3	4	7.2	530.0	13.4	6.0	7.1
Angle	-33.4	-23.7	-3.6	-24.0	-25.4	-15.2	-0.2	-8.4	-18.0	-15.5
Step	11	12	13	14	15	16	17	18	19	20
$\frac{K_I}{K_{II}}$ ratio	4.1	15.0	5.8	8.3	8.6	4.0	7.3	8.7	9.1	9.2
Angle	-24.7	-7.6	-18.5	-13.4	-13.0	-25.4	-15.1	-12.8	-12.2	-12.2
Step	21	22	23	24	25	26	27	28	29	30
$\frac{K_I}{K_{II}}$ ratio	10.2	9.9	31.0	20.0	29.7	25.4	21.2	35.6	33.8	11.6
Angle	-11.0	-11.4	-3.7	-5.7	-3.9	-4.5	-5.4	-3.2	-3.4	-9.7

7.3   Case 3

This case is similar to the vertical force analysis. Only difference is that it has two precipitates at $-0.028; -0.059$ and $-0.018; 0.059$. Crack paths in specimen with precipitates are shown in figure 7.12 and 7.13. In figure 7.14 displacement vectors are plotted. Deformed mesh is plotted in figure 7.15. Tables 7.4 and 7.5 shows the crack growth $\frac{K_I}{K_{II}}$ ratio and the angles at each step.

(a) Precipitates 3 times stiffer.

(b) Precipitates 7 times stiffer.
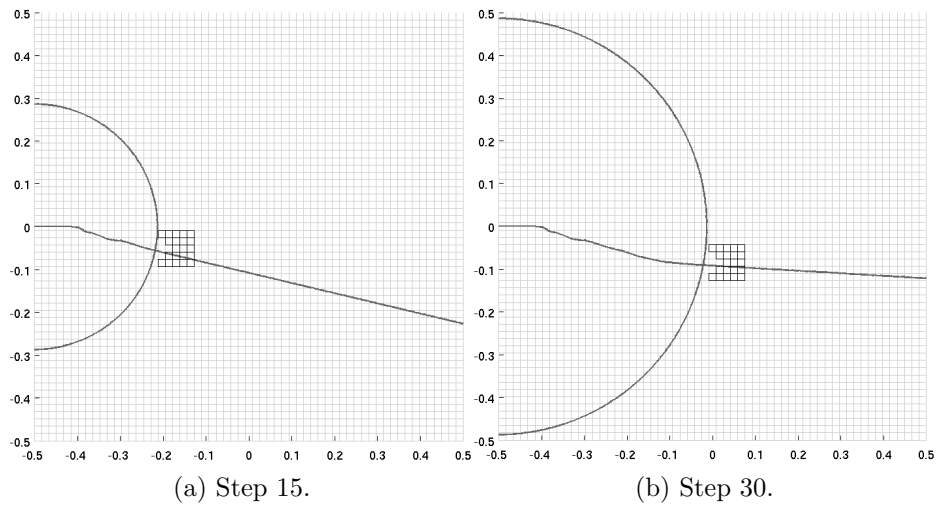
Figure 7.12: Crack path at step 15.

Table 7.4: $\frac{K_I}{K_{II}}$ ratios and crack growth angles (degrees) at different step (3 times stiffer precipitates).

Step	1	2	3	4	5	6	7	8	9	10
$\frac{K_I}{K_{II}}$ ratio	20.3	-54.0	36.2	149.3	67.4	19.4	14.4	9.1	9.1	20.0
Angle	-5.6	2.1	-3.2	-0.8	-1.7	-5.9	-7.9	-12.3	-12.2	-5.7

Step	11	12	13	14	15	16	17	18	19	20
$\frac{K_I}{K_{II}}$ ratio	20.5	10.6	-8.0	9.2	14.4	-13.1	5.9	-5.6	14.8	-17.2
Angle	-5.6	-10.6	13.8	-12.1	-7.9	8.6	-18.4	19.1	-7.7	6.6

Step	21	22	23	24	25	26	27	28	29	30
$\frac{K_I}{K_{II}}$ ratio	-31.6	-8.0	-4.1	-5.1	6.6	5.9	-1.3	3.6	4.2	38.4
Angle	3.6	13.9	24.9	20.9	-16.6	-18.2	49.1	-27.3	-24.2	-3.0

(a) Precipitates 3 times stiffer. (b) Precipitates 7 times stiffer.
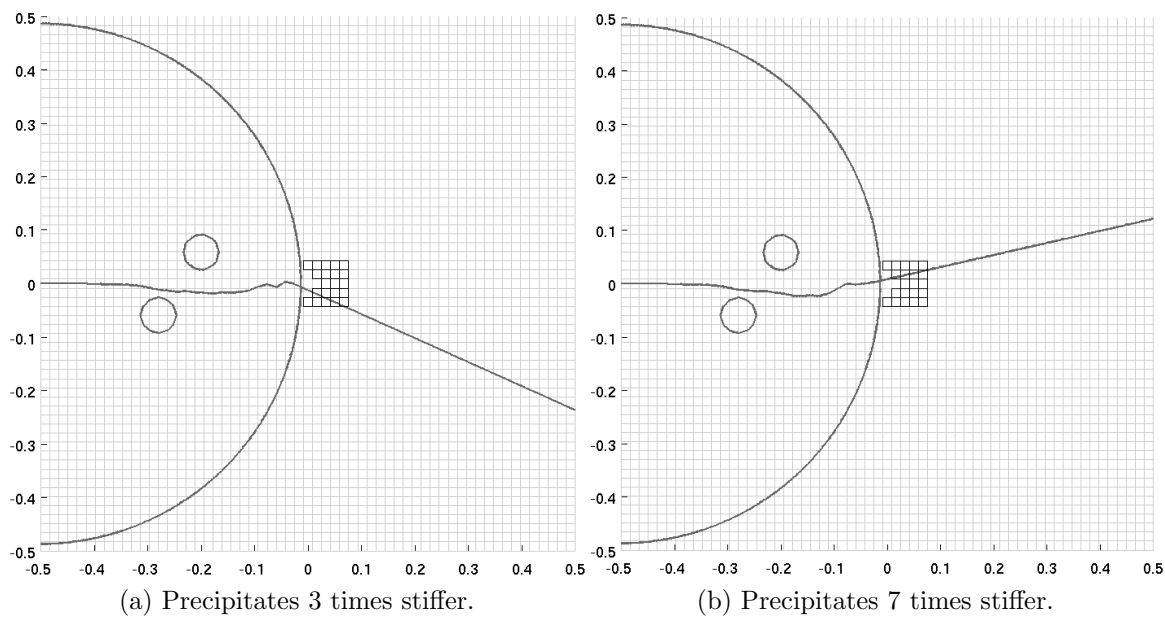
Figure 7.13: Crack path at step 30.

(a) Precipitates 3 times stiffer. (b) Precipitates 7 times stiffer.
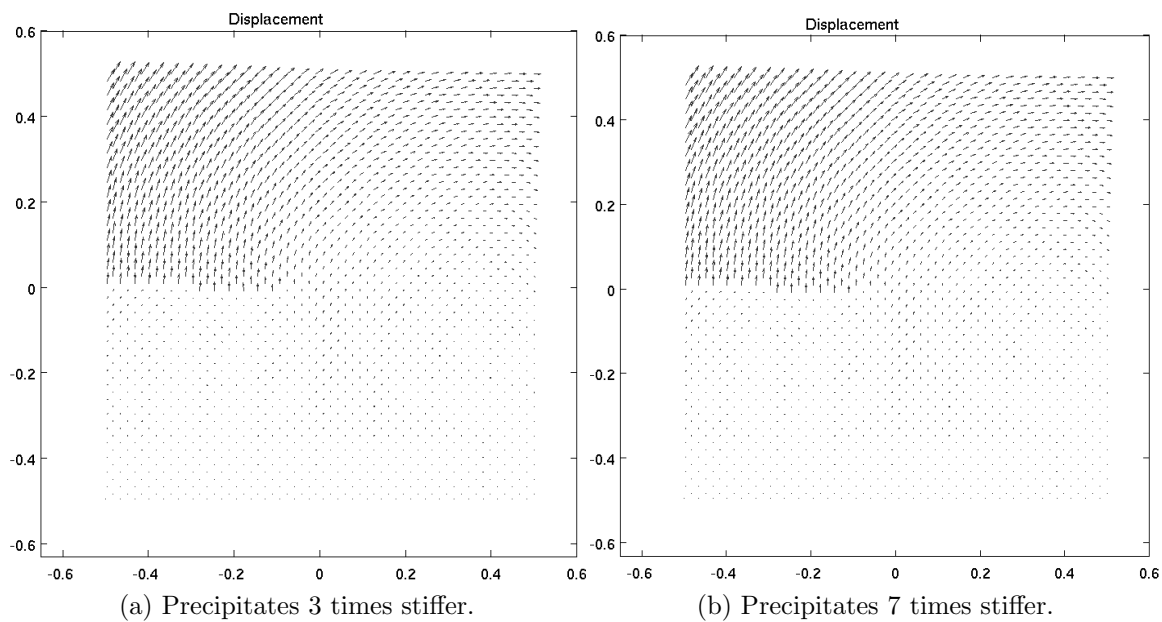
Figure 7.14: Displacement vectors at step 30. Crack mouth opening is 4×10^{-5}

(a) Precipitates 3 times stiffer.
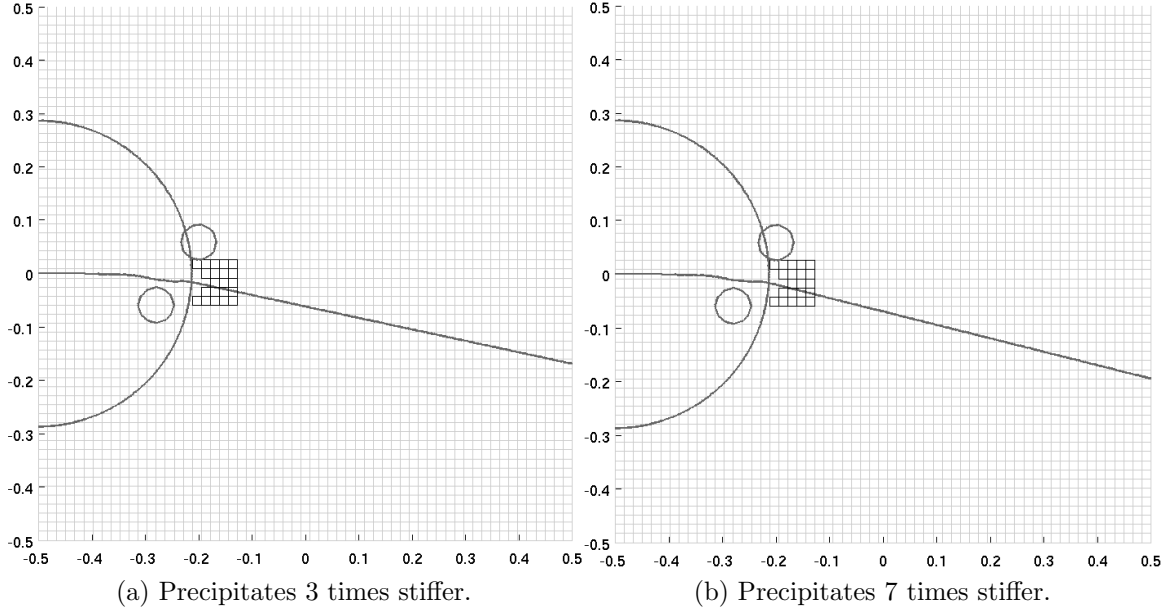
(b) Precipitates 7 times stiffer.
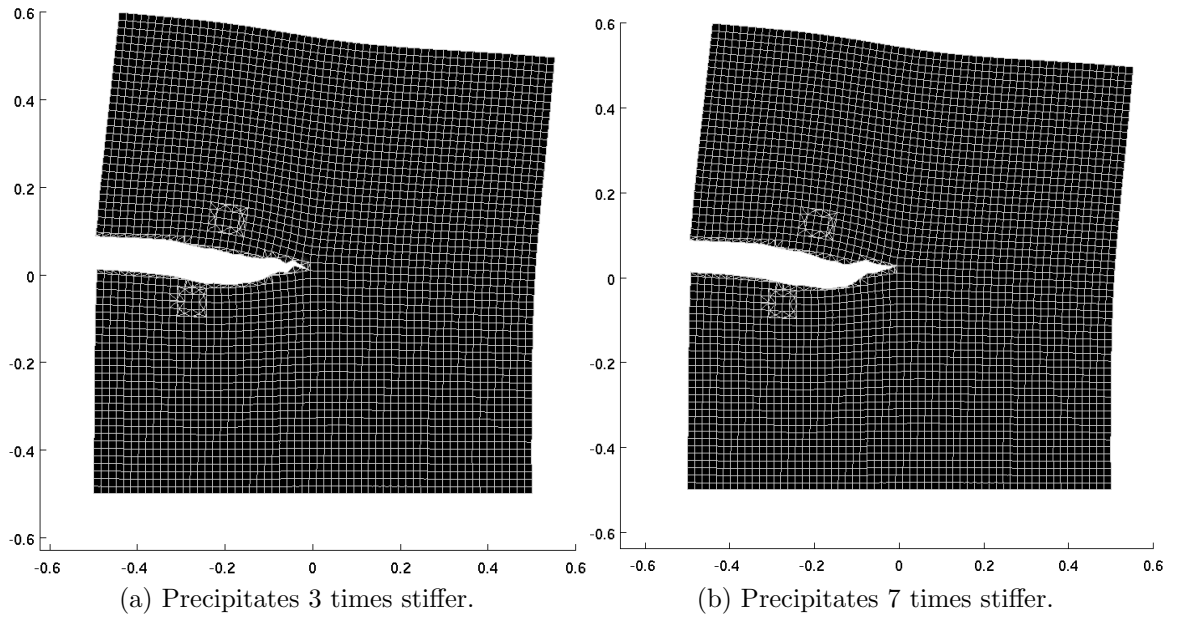
Figure 7.15: Displacement vectors at step 30.

Table 7.5: $\frac{K_I}{K_{II}}$ ratios and crack growth angles (degrees) at different step (7 times stiffer precipitates).

Step	1	2	3	4	5	6	7	8	9	10
$\frac{K_I}{K_{II}}$ ratio	22.5	-49.0	34.8	126.5	65.5	19.2	13.7	9.3	9.8	31.4
Angle	-5.1	2.3	-3.3	-0.9	-1.8	-5.9	-8.2	-12.0	-11.5	-3.6
Step	11	12	13	14	15	16	17	18	19	20
$\frac{K_I}{K_{II}}$ ratio	35.1	10.6	-11.3	7.9	10.9	-44.7	3.8	-16.1	-14.7	10.7
Angle	-3.23	-10.6	9.9	-14.0	-10.4	2.6	-26.5	7.1	7.7	-10.5
Step	21	22	23	24	25	26	27	28	29	30
$\frac{K_I}{K_{II}}$ ratio	-27.7	-4.0	-3.4	-2.4	924.2	8.9	-7.0	-19.9	-8.7	-7.0
Angle	4.1	25.1	28.9	35.9	-0.1	-12.5	15.7	5.7	12.8	15.6

70

8

Discussion

Results of the three cases are discussed in the following sections. The "cut off"-function (exponential/polynomial) used in the `gf_global_function`-function did not have significant effect in the results. In this work a polynomial cutoff-function was used.

7.1 Case 1

The shape of the vertical normal stress component field (figure 7.2) is similar to the predicted in figure 2.15 ([7]). In table 7.1 stress intensity factor given by the code and Irwin's analytical solution (equation 2.16) are compared. K_{ref} $(= \sigma_0 \sqrt{\pi a})$ is used in K_{Irwing} calculation. a and W are crack length and specimen width respectively. Accuracy of the stresses, form where the error is calculated, is 8 decimals (only 6 is presented).

Table 7.1: Normalized values of SIF for two different discretization

Elements (horizontal X vertical)	59 X 59	225 X 225
Distance	0.053	0.0139
Crack tip stress	$22.1301 * 10^6$	$37.0845 * 10^6$
Loading pressure	$5.0 * 10^6$	$5.0 * 10^6$
W	1	1
a	0.3	0.3
K_{ref}	$6.8647 * 10^6$	$6.8647 * 10^6$
K_{Irwing}	$11.4010 * 10^6$	$11.4010 * 10^6$
K_{Calc}	$12.7665 * 10^6$	$10.9551 * 10^6$
Error %	11.89	- 3.99

As seen in table 7.1, the error between computed solution and analytical solution diminish significantly as the amount of elements is increased. Also, the fact that loading is not exactly pure mode I, as seen in figure 6.4, has an affect to the computed value. The "non purity" is a result of the loading condition: the loading force is tied

to the nodes and the distance between nodes affects the accuracy of the outcome. This change in the boundary condition as the mesh turns denser is seen in figure 6.4.

The accuracy could probably be increased by adapting the area from which the crack tip stress field is calculated. In this work it was kept unchanged between since the error produced by the meshes in terms of accuracy was kept unchanged between every case. Accuracy could also be further tuned by adjusting variables r, r0, and r1 in the global function command used in the code since they affect the displacement field around the discontinuity.

7.2 Case 2

Results in all three cases are in good agreement with expected behavior on a fracture mechanical basis: vertical force produces (approximately) a horizontal crack, a horizontal force produces a descending crack, and a tilted force produces also a descending crack but the slope is not a steep as with the horizontal force.

The angles with horizontal and tilted forces are not as steep as they should be in pure mode II and mixed mode (when the magnitude of both modes is equal) about $70°$ and about $53°$ respectful. This error is due to the fact that the stress state in close proximity of the crack tip is not exactly in accordance with the pure mode II and mixed mode cases. The behavior between the boundary and the crack tip affects the resulting displacement field so that it is not exactly similar compared to analytical ones. Also the type of the boundary condition causes some error: Force controlled boundary condition produces slightly differing displacement field to the boundary than displacement controlled. This has direct effect to the displacement field at crack tip. Force controlled boundary condition tilts as the crack opens. And subsequently the specimen bending is greater in the "free" part (the part above the crack) of the specimen than in displacement controlled case.

Some error is due to the way how the boundary condition is tied to the specimen as discussed earlier (chapter 6), this error would diminish with element size. Also the fact that values of crack tip stresses are computed as a mean value of an area, produces some differences in calculated and predicted crack paths.

The fluctuation of the crack growth angle is caused by the fluctuation in displacement fields around the crack tip: Crack tip moves in respect to the specimens boundary which produces alterations to the stress field and hence also the displacement field changes from step to step. As discussed above force controlled boundary condition bends the specimen more than displacement controlled especially when the force is not perpendicular to the specimen's boundary. Especially if the displacement controlled boundary condition is parallel to the specimen boundary (and it is not allowed to tilt) the specimen's "free" surface would not bend at all. Also some of the fluctuation in $\frac{K_I}{K_{II}}$ ratios is due to the changing of place of the crack tip within an element as a result of the XFEM interpolation (crack growth increment differs from the element length).

7.2.1 Vertical Force

Crack angles and K_I/K_{II}-ratios in 7.2.1 are in good agreement with the analytical ones (chapter 2: Crack growth criterion). The crack grows almost perpendicularly to the applied force, the overall (from the end of initial crack to the end of crack growth) crack growth angle is 3.4 degrees.

Boundary conditions and the coarseness of the mesh explain the trend in crack growth angle, which is few degrees. Although boundary condition has only a vertical component the specimens upper left corner moves to up and right since the horizontal direction is not restricted. This bends the specimen, as discussed above, and creates a minor mode II component to crack propagation and hence the crack is not exactly straight. Also the angle of growth from step to step is due to this bending (the quantity of mode II increases as crack propagates). As a certain point is passed in crack propagation the propagation turns to be more horizontal. At this point the specimen is so fractured and the left boundary does not have that much of an effect to the stress field any more.

The fluctuation as seen e.g. in steps 23, 24, and 25 where the crack growth angle is $11.2°$, $-1.5°$, and $-35.5°$ is due to the previously discussed crack tip place regarding element edges.

7.2.2 Horizontal Force

This sub-case is as pure mode II crack propagation as can be achieved with force controlled boundary condition and without binding the vertical displacement component. The initial crack propagation angle from the straight part of the initial crack propagation curve (x = -0.4...-0.3 figure 7.6: steps 1...10) is about $-41.5°$ which corresponds a $\frac{K_I}{K_{II}}$-ratio of 2 (figure 2.20). The angle at step 1 is $51.2°$ which in turn corresponds a $\frac{K_I}{K_{II}}$-ratio of 1. As the crack propagates and the specimen bends the crack turns to propagate more horizontally and the overall crack angle is $-27.6°$ and it corresponds to $\frac{K_I}{K_{II}}$-ratio of 4. This tilting as crack propagates is due to the same phenomena as above: as crack propagates the $\frac{K_I}{K_{II}}$-ratio alternates.

The Von Mises stress field in figure 7.7b is similar to the one shown in figure 7.2 only the one in 7.7b is tilted to an angle. The angle in which the stress field is tilted is $12.4°$ the angle of the last crack propagation angle. The direction of crack propagation is in good agreement with the mixed mode crack propagation presented in [8].

7.2.3 Tilted Force

In this analysis the loading force is tilted to $45°$ angle and thus a greater mode II component than with horizontal force.

Initial crack growth angle in this case is $-33.4°$ ($\frac{K_I}{K_{II}}$-ratio of 3) which is significantly smaller than in the previous case. Comparing figures 7.6 and 7.9 the effect of the force vector tilting can been seen. The overall crack propagation trend is steeper in the first than in the latter figure.

The trend crack propagation of the first ten steps is $-17.5°$ and overall angle is $-13.2°$, which corresponds to $\frac{K_I}{K_{II}}$-ratios of greater than 4 (figure 2.20).

7.3 Case 3

As seen in figures 7.15 the precipitates affect the crack propagation path, and the more stiffer the precipitate is the more it affects the cracks path (figures 7.12 and 7.13). The effect of the stiffer regions is clear. When comparing to the vertical force analysis results (7.2.1 with the tables in case three (7.3 and 7.3), it is seen that the crack starts to grow towards the first precipitate. After the crack tip has passed the center point of the first precipitate (step 10) it slowly starts to tilt upwards, but it remains closer to the first precipitate and hence it does not turn horizontal until the step 18 when the second precipitate is the closest one. Between steps 22 and 26 crack path tilts upwards as a result of the second precipitate's effect to the stress field. After step 26 the trend in crack growth is similar to the one in vertical force analyses in case two. The crack paths are similar in both cases, but the effect of the precipitate is stronger with stiffer precipitates, as it is expected.

The set-up on the crack trajectory in the precipitate analysis and the vertical loading case is similar, an as such the resulting crack paths differ only around the them.

9

Future Work

At present the code is suited only to analyze crack propagation in very simple geometries and material models in two dimension. The most important step to enable real analysis with the code is to implement further material models to the Getfem-library. Fortunately new material models can be introduced into the library by modifying the existing model files, and also the addition process is quit simple due to the Getfem's open structure. The difficulties arise primarily in the actual numerical XFEM implementation of realistic material models.

The fact that code supports only two dimensional cases prevents usage of the code in a complex cases. Though most common specimens used in research purposes are usually relatively simple (most common being compact tension- and Single-Edge Notched Bending-specimens), and their behavior can be modeled quite accurately with two dimensional models. When analyzing real complex objects a three dimensional model is usually needed especially if details of the cracking behavior at the crack tip are important. Also, if a comparison in cracking behavior between a real part and test specimen is desired, only a three dimensional model can give accurate enough results. At present stage of Getfem's development only two dimensional level sets are supported in the Matlab interface.

Code written in C++-language would be more efficient and lighter than the same code in Matlab-script, and thus less computer time is needed in a single analysis, is a good reason to rewrite the XFEM-code in C++-language. Also matters discussed above are powerful arguments for the rewriting proses.

Meshing capabilities of the Getfem-library are not very efficient and limited only to simple geometries, as mentioned in chapter 5. Fortunately, the Getfem-library supports some third party meshers. Incorporating a capable mesher to a XFEM-analyzing procedure is essential in expanding the code's capabilities.

The actual accuracy of the code can be increased by specifying the variables used in global function command. The exact values of the variables depend on the specimen geometry and boundary and initial conditions as well as the meshes quality. Also, determining the actual effective distance between crack tip and the area from which the crack tip stress is calculated better is proposed. Meshes quality and density have a big affect on the distance.

As discussed, a lot of work still remains in the development of a truly capable and versatile XFEM-code, but many of the elementaries of the work are already done.

10

Summary

The purpose of this work was to develop a code that is capable of modeling crack propagation. The code is based on the XFEM theory since conventional FEM is not typically efficient enough in fracture mechanical problems. A linear elastic material model was chosen to keep the work simple enough and the main focus was directed in developing a working analysis tool. Complex functionalities, such as nonlinear material models, will be introduced later. The code was programmed using the Matlab environment. Getfem finite element library was tested and found to provide many of the necessary functionalities. Especially Getfem's Matlab interface was utilized.

Getfem-library is a open source research code developed in France at INSA (Institut National des Sciences Appliques) in Toulouse and Lyon. It is a generic C++ finite element library with Matlab and Python interfaces. Getfem is still under development and especially the interfaces do not yet provide all of its functionalities. At present it provides tools for programming to analyze two dimensional fracture mechanical problems. The library was found to be versatile and adaptable.

The code developed during this work was found to be efficient and accurate for analyzing crack propagation in simple cases. The accuracy of the code can be increased in the future by altering the cutoff-function type used. In this work much time was not spent in valuing the best possible function, since the goal of this work was to develop a working code and the absolutely exact results were not a priority. At this point the code is restricted to linear elastic problems with a quite coarse mesh. As was seen in this work when a more detailed analysis (denser mesh) or a analysis of a more complex problem (specimen containing different materials or several cracks) is needed the computing cost increases dramatically.

Three different cases were analyzed. The first case was used to verify that the code is generally viable and yielded accurate enough results. The accuracy of the code was found to be adequate for this purpose although it could have been increased by increasing the quantity of elements, but this was not pursued due to a desire to manage the problem in a workstation environment. In the second case crack propagation was analyzed. An initial crack was introduced into the specimen and it was grown about to the middle (in horizontal direction) of the specimen.

The code was run with three different set up in the second case. First a force perpendicular to the crack was introduced. The crack propagated to perpendicular direction relative to the applied force, which is in good agreement with the expected

results (crack opening mode I). In second and third analysis the applied force was parallel and in 45° angle relative to the crack. The crack propagation angle is more steeper the more greater the angle of the applied force relative to the initial crack plane.

In the last case, crack behavior in a specimen containing stiffer sections (precipitates) was analyzed, or rather the how the code copes with such a case. The case was identical, besides the precipitates, to the first analysis in case 2. The crack was supposed to turn towards the stiffer areas and indeed it did it. After the first precipitate the crack path started to turn towards the second precipitate.

Overall the code was found to be effective in relatively simple cases. In the future other more complex and thus more realistic material models are planned to be introduced. This would allow the analysis far more realistic fracture mechanical problems. Also a better mesher will be incorporated and as the Getfem-library develops a possibility to analyze three dimensional, more accurate models is planned. Rewrites in C++-language are considered. Matlab was only used to ease the programming and usage (adaptation to different set-ups) of the code.

XFEM is very efficient in handling crack propagation, since it does not require remeshing in every crack growth increment and crack geometry tracing can be attained generally in three dimensions. Although due to the simplicity of the specimen treated in this work, traditional FEM might have been even faster to compute than XFEM. The integrand, produced by XFEM, needs considerably more computer time than an integrand of the ordinary FEM analysis, and the meshing of the specimen is quite straight forward (since the specimen is simple square with a relatively straight crack path). Though the accuracy of the calculations would have probably suffered, since the shape of some of the elements (the ones near crack) would have been corrupted. This shortcoming is rapidly overcome in XFEM as the complexity of the specimen and/or the crack path is increased. The computer time consumed by the XFEM's more complex integrations remains about the same regardless of the complexity of the specimen, but the time needed to remesh the specimen, in the case of ordinary FEM, increases significantly and the analysis approach itself can become unbearable.

Bibliography

[1] W. Cecot. Adative fem analysis of selected elastic-visco-plastic problems. *Computer Methods in Applied Mechanics and Engineering*, 196:3859–3870, 2007.

[2] P. Wang. Modeling material responses by arbitrary lagrangian eulerian formulation and adaptive mesh refinement method. *Journal of Computational Physics*, 229:1573–1599, 2010.

[3] M. Denda and Y.F. Dong. Analytical formulas for a 2-d crack tip singularity boundary element for rectilinear cracks and crack growth analysis. *Engineering Analysis with Boundary Elements*, 23:35–49, 1999.

[4] T. Belytschko, Y.Y. Lu, L. Gu, and M. Tabbara. Element-free galerkin methods for static and dynamic fracture. *International Journal of Solids and Structures*, 32(17/18):2547–2570, 1994.

[5] Thomas-Peter Fries. The extended finite element method, http://www.xfem.rwth-aachen.de/, 2010.

[6] S. Mohammadi. *Extended Finite Element Method*. Blackwell Publishing Ltd, 2008.

[7] M. Janssen, J. Zuideman, and R. Wanhill. *Fracture Mechanics*. Spon Press, 2004.

[8] T.L. Anderson. *Fracture Mechanics: Fundamentals and Applications*. CRC Press, 2006.

[9] M.L. Williams. On the stress distribution at the base of a stationary crack. *Journal of Applied Mechanics*, 24:109–114, 1957.

[10] H.M. Westergaard. Bearing pressures and cracks. *Journal of Applied Mechanics*, 6:49–53, 1939.

[11] G.R. Irwin. Analysis of stress and strains near the end of a crack transversing a plate. *Journal of Applied Mechanics*, 24:361–364, 1957.

[12] G.I. Barenblatt. The mathematical theory of equilibrium cracks in brittle fracture. *Journal of the Mechanics and Physics of Solids*, VII:55–129, 1962.

[13] D.S. Dugdale. Yielding in steel sheets containing slits. *Journal of the Mechanics and Physics of Solids*, 8:100–104, 1960.

[14] J.R. Rice. Path independent integral and the approximate analysis of strain concentration by notches and cracks. *Journal of Applied Mechanics*, 35:379–386, 1968.

[15] J.W. Hutchinson. Singular behavior at the end of a tensile crack tip in hardening material. *Journal of the Mechanics and Physics of Solids*, 16:13–31, 1968.

[16] J.R. Rice and G.F. Rosengren. Plain strain deformation near a crack tip in power-law hardening material. *Journal of the Mechanics and Physics of Solids*, 16:1–12, 1968.

[17] B.N. Whittaker and R.N. Singh. *Rock Fracture Mechanics, Principles, Design and Applications*. Elsevier, The Netherlands, 1992.

[18] F. Erdogan and G.C. Sih. On the crack extension in plates under plane loading and transverse shear. *Journal of Basic Engineering*, 85:519–527, 1963.

[19] C. Johnson. *Numerical Solutions of Partial Differential Equations by the Finite Element Method*. Studentliteratur, 1987.

[20] O.C. Zienkiewicz and R.L. Taylor. *The Finite Element Method Volume 1: The Basis*. Butterworth-Heinemann, 2000.

[21] O.C. Zienkiewicz and R.L. Taylor. *The Finite Element Method Volume 2: Solid Mechanics*. Butterworth-Heinemann, 2000.

[22] T. Belytschko, Y.Y. Lu, and L. Gu. Element-free galerkin methods. *International Journal for Numerical Methods in Engineering*, 37:229–256, 1994.

[23] J.M. Melenk and I. Babuska. The partition of unity finite element method: Basic theory and applications. Number Research Report No. 96-01, CH-8092 Zürich, Switzerland, January 1996. Seminar für Angewandte Mathematik, Eidgenossische Technische Hochschule.

[24] T. Belytschko and T. Black. Elastic crack growth in finite elements with minimal remeshing. *International Journal of Fracture Mechanics*, 45:601–620, 1999.

[25] S. Bordas and A. Legay. X-fem mini-course. EPFL, 2005.

[26] T. Elguedj, A. Gravouil, and A. Combescure. Appropriate extended function for x-fem simulation of plastic fracture mechanics. *Computer Methods in Applied Mechanics and Engineering*, 195:501–515, 2006.

[27] N. Möes, J. Dulbow, and T. Belytschko. A finite element method for crack growth without remeshing. *International Journal for Numerical Methods in Engineering*, 46:131–150, 1999.

[28] J.E. Dulbow. *An Extended Finite Element Method with Discontinuity Enrichment for Applied Mechanics*. PhD thesis, Northwestern University, 1999.

[29] J.A. Osher, S. snd Sethian. Front propagating with curvature-dependent speed: Algorithms based on hamilton-jacobi formulation. *Journal of Computational Physics*, 79(1):12–49, 1988.

[30] G. Ventur, E. Budyn, and T. Belytschko. Vector level sets for description of propagating cracks in finite elements. *International Journal for Numerical methods in Engineering*, 58:1571–1592, 2003.

[31] M. Storlaska and D.L. Chopp. Modeling thermal farigue cracking in integrated circuits by level sets in extended finite element method. *International Journal of Engineering Science*, 51:2381–2410, 2003.

[32] D.L. Chopp. Some improvements on the fast marching method. *SIAM Journal of Scientific Computations*, 23(1):230–244, 2001.

[33] J.A. Sethian. A marching level set method for monotonically advancing fronts. *Proceedings of National Academy of Science*, 93(4):1591–1595, 1996.

[34] J.A. Sethian. Fast marching methods. *SIAM review*, 41(2):199–235, 1999.

[35] J.R. Rice. Extended finite element method and fast marching method for three-dimensional fatigue crack propagation. *Engineering Fracture Mechanics*, 70:29–48, 2003.

[36] Y. Renard and J. Pommier. Getfem++ documentation, part 2: Short user documentation. July 2009.

[37] E. Chahine, P. Laborde, J. Pommier, Y. Renard, and M. Salaün. Study of some optimal xfem type methods. 2005.

[38] E. Chahine, P. Laborde, and Y. Renard. Crack tip enrichment in the xfem using a cutoff function. *International Journal for Numerical Methods in Engineering*, 75:629–646, 2008.

[39] P. Hild, V. Lleras, and Y. Renard. A posterior error analysis for poisson's equation approximate by xfem. *ESAIM: PROCEEDINGS*, 27:107–121, 2009.

[40] Y. Renard and J. Pommier. Getfem++ documentation, part 1: Description of the project. March 2009.

[41] C. Zhiqiang, K. Seokchan, and W. Gyungsoo. A finite element method using singular functions for the poisson equation: crack singularities. *Numerical Linear Algebra with Applications*, 9:445–455, 2002.